Selective Area Grown InAs QDs on GaAs buffer dot structures

Characterization and photo luminescence observation

MSc thesis

Written by *Charline Kaisa Reffeldt Kirchert*

Supervised by

Peter Krogstrup and Peter Lodahl

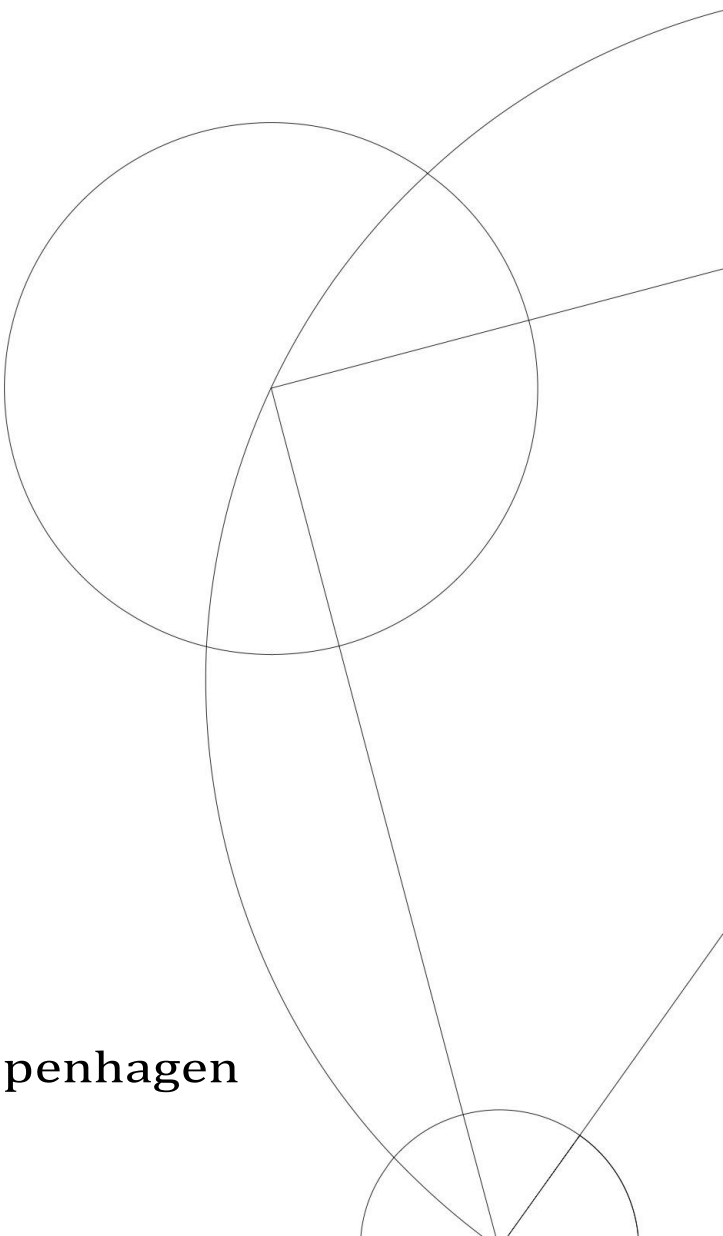

University of Copenhagen

Name of Institute: Faculty of Science

Name of Department: Niels Bohr Institute

Author(s): Charline Kaisa Reffeldt Kirchert

Email: nsl738@alumni.ku.dk
chasliie@gmail.com

Title and subtitle: Selective Area Grown InAs QDs
on GaAs buffer dot structures
- Characterization and photo luminescence observation

Supervisor(s): Peter Krogstrup and Peter Lodahl

Handed in: 2021-11-14

Defended: 2021-11-26

Name _____

Signature _____

Date _____

Abstract

The approaches for creating qubits are many but one of the great problems is to upscale the quantum information hardware platform. The photonic qubit is one of the candidates with limitations in size, shape, and position distribution of the grown III-V quantum dots (QDs).

For this thesis selective area (SAG) grown InAs QDs are grown on GaAs buffer dot structures using electron beam lithography (EBL), HF wet etching and molecular beam epitaxy (MBE) growth techniques. The mask openings and GaAs buffer structures have been studied using atomic force microscopy (AFM) and scanning electron microscopy (SEM), the GaAs/InAs interface and InAs QDs have been investigated using tunneling electron microscopy (TEM) and the photo luminescence (PL) of the InAs QDs have been observed using an above band excitation (ABB) laser.

The formation of shapes of the GaAs buffer are classified into 4 different growth stages; 1. 4-fold symmetry with facet family {110}{111}, 2. 4-fold symmetry with facet family {110}, 3. 1-fold symmetry with facet family {110}{111} and 4. 4-fold symmetry with facet family {111}. The nominal growth rate Γ_{Inc}, i.e how much material that have been Incorporated into the SAG openings compared to a thin film growth without a mask, have been found for the GaAs buffer dots to be of maximum 0.019, which indicate sourcing growth mode where more material is going to the mask then what is incorporated in the mask openings. The InAs QDs were found to be highly relaxed on top of the GaAs buffer dots with a dislocation diameter of 8.6 nm - 10 nm and the diameter measured to roughly 70 nm and height to roughly 30 nm. This results in wavelengths approaching the wavelengths of bulk InAs (3000 nm). Wavelengths above 1100 nm were not possible to detect in the spectrometer available for this project however luminescence was seen in the camera for some of the QDs even though the efficiency above wavelengths of 1000 nm for the camera were under 5 %.

Future studies should focus on optimizing the fabrication of the mask openings to get the openings as uniform as possible for better control of the shape and size of the GaAs buffer dots. The growth parameters should be adjusted to favor small GaAs buffer dots with small top-facets for the InAs QDs to grow on. The growth parameters for InAs should be adjusted to grow Stranski-Krastanov (SK) like QDs to get the wavelength of around 920 nm used for photonic qubits.

Acknowledgements

First, I would like to thank Peter Krogstrup and Peter Lodahl for being my supervisors through this master project which has been a great start of my academic career.

This thesis project becomes a success owing to daily team-work with Laurits Højel and great discussions and essential help from Daria Beznasiuk, Martin Espiñeira, Charalampos (Harry) Lampadaris, Gunjan Piyush Nagda, Damon Carred, Steffen Zelzer, Martin Bjergfelt, Ying Wang, Vasiliki Angelopoulou, Arianna Brooks, Martin Hayhurst Appel and Mikkel Thorbjørn Mikkelsen.

I would also like to thank Thor Hvid-Olsen, Rasmus Dalsgaard Schlosser, and Stine Grønfeldt Stenspil for being good Nano-fellow friends and helping through though times and long days at the institute.

Last but not least an indescribable thanks to my family and partner in life Jonas Braun Lynnerup for the unlimited support and for always believing in me.

Symbols and abbreviations

InAs	Indium Arsenide
GaAs	Galium Arsenide
SiOx	Silicon Oxide
HF	Hydrofluoric acid
QD	Quantum Dot
SAG	Selective Area Growth
NW	Nano Wire
SEM	Scanning Electron Microscopy
AFM	Atomic Force Microscopy
EBL	Electron Beam Lithography
MBE	Molecular Beam Epitaxy
PMMA	Polymer i.e resist for spin coating
SK	Stranski-Krastanov growth mode
WL	Wetting-layer
Ml	Monolayer
QW	Quantum Well
SP	Stereographic projection

Quantum well:

r	Radius of QD (in x, y and z direction)
E	Energy
E_g	Band-gap energy
E_c	Energy of conduction band
E_v	Energy of valence band

ΔE_c	Energy difference between QW in E_c and lowest energy state in conduction band
ΔE_v	Energy difference between QW in E_v and highest energy state in valence band
ΔE	Total energy difference between electron-hole pair (exciton)
λ	Wavelength
$\frac{1}{\mu}$	Reduced mass of electron/hole

Lattice misfits:

a	lattice constant
b	burgers vector
f	misfit strain parameter
p	distance between dislocations
	strain

Kinetics:

TS	Transition state
ERS	Equilibrium reference state
g	Gibbs-free energy
p	Adatom phase
q	Crystal phase
i	Adatom material (e.g. Ga)
μ^{ERS}	Chemical potential of ERS
$\delta\mu_{p-ERS}$	Chemical potential of p
$\delta\mu_{q-ERS}$	Chemical potential of q
$\delta g^{TS}_{pq,i}$	Activation energy from p to q phase

SAG:

I	Incorporation
a	Adatom
c	Crystal
s	Solid phase
v	Vapour phase
i	Material (e.g Ga)
f	Flux
Γ	Rate
w	Width of NW
l	Length of NW
m	Mask
$\Delta\Gamma_{a_m a_c,i}$	Exchange rate of adatoms over trench border; sourcing mode when <0, balanced mode when =0, sinking mode when >0

Wulff:

ECS	Equilibrium crystal shape
$\mathbf{h}_{hkl}$	Radial vector
γ	Surface energy of a facet

Contents

1 Introduction

1.1 Motivation

It is no secret that quantum technology is very close to becoming a big part of the commercial industry. More than ever has the research fields have been dominated by finding solutions to solve the problems with quantum computing and information. Many different techniques for manufacturing different types of quantum dots (QDs) to develop qubits have been explored intensively throughout the last decades. Three types of qubits that have been studied broadly is electron and nuclear spin qubits based on nuclear magnetic resonance (NMR) [1, 2], topological Majorana bound state qubits occurring at the ends of topological nanowires (NWs) [3, 4], and photonic qubits such as semiconductor QDs embedded in wave-guides [5, 6].

In this thesis, selective-area grown (SAG) InAs QDs on GaAs buffer dots have been investigated. InAs and GaAs are both compound semiconductors of the III-V material family. These III-V semiconductors are of the zinc-blend (ZB) crustal structure with the space group F-43m. These components are used in a broad range of semiconducting research and are the main family for applications of optically active QDs. InAs QDs are often used for photonic qubits in the near-infrared spectra [7].

Techniques for approaching the nano-scale are plentiful, different combinations of bottom-up and top-down methods are used and some of the techniques for fabricating III-V semiconductor QDs are mentioned herein. One approach is the self-assembled III-V QD grown by either metal-organic chemical vapor deposition (MOCVD) [8] or molecular beam epitaxy (MBE) [9]. In the latter, the semiconductor QD is grown layer by layer. The QDs are randomly distributed in size and position as they nucleate into islands as an effect of the strain in the interface of the substrate and the QDs. This growth mode is also called Stranski-Krastanov (SK) [10] and will be the reference and starting point for this thesis (SK growth is described in more detail in Section 1.2.2). Another approach is the droplet epitaxy where the size is more controlled and the material used can vary more because the formation of dots does not depend on strain as with the self-assembled SK QDs. This technique is though reported to have a lower quantum efficiency and be less optically active [11].

To be able to upscale the photonic qubits control of parameters such as the position and size have to be solved. This can be done to some extend by combining bottom-up as growth techniques with top-down approaches such as etching techniques and electron beam lithography (EBL) to define the nucleation sites for the growth [12]. A technique

using focused ion beam (FIB) can be used to create openings (reported to be of 63 nm in diameter [13]) in a GaAs layer for the nucleation sites of InAs. In the paper of M. Matha et *al.* [13] ≈ 50 InAs QDs were found in a single growth site which could be adjusted to having single QDs in 52 % of the openings when changing the growth parameters of InAs to grow QDs of approximately the size 40 nm in diameter and 5 nm in height. The technique is limited to the opening of the FIB spot where the InAs QD can be more selectively placed but still distributed and intervention in the pure epitaxy GaAs layer will form impurities which affect the quality of the InAs QD. To solve the problem with the low quality and inactivity of the InAs QD a seed layer can be introduced which is simply growing one more layer of the GaAs and InAs on top without the FIB. The seed layer underneath will induce the growth site of the InAs due to strain [14, 15]. Unfortunately, the quantum efficiency, which is the ratio between radiative and non-radiative decays, is found to be 47 ± 14% [16] which is much lower then the quantum efficiency found for simple SK grown QDs of 90 ± 4% [17]. The quantum efficiency describes how many photons can be collected which need to be large in order for the QDs to be of good quality in therms of life-time and narrow line-width to be useful for quantum information.

This study is a joint project between the research group of the quantum photonic group led by professor Peter Lodahl and the material science group led by professor Peter Krogstrup Jeppesen to study the possibilities of MBE SAG grown InAs QDs solving the questions of defining the position of the nucleation site of the InAs SK grown QDs and the size of the QDs. By doing so, this thesis discusses the growth evolution of the GaAs buffer dots and the photo luminescence of the grown InAs QDs. Using SAG for InAs QDs shows a high potential for engineering the position, size, and shape of the QDs and thereby could be used in the race towards up-scaling qubits, this is more or less a matter of defining the right growth parameters.

1.2 Theory

1.2.1 Quantum dots

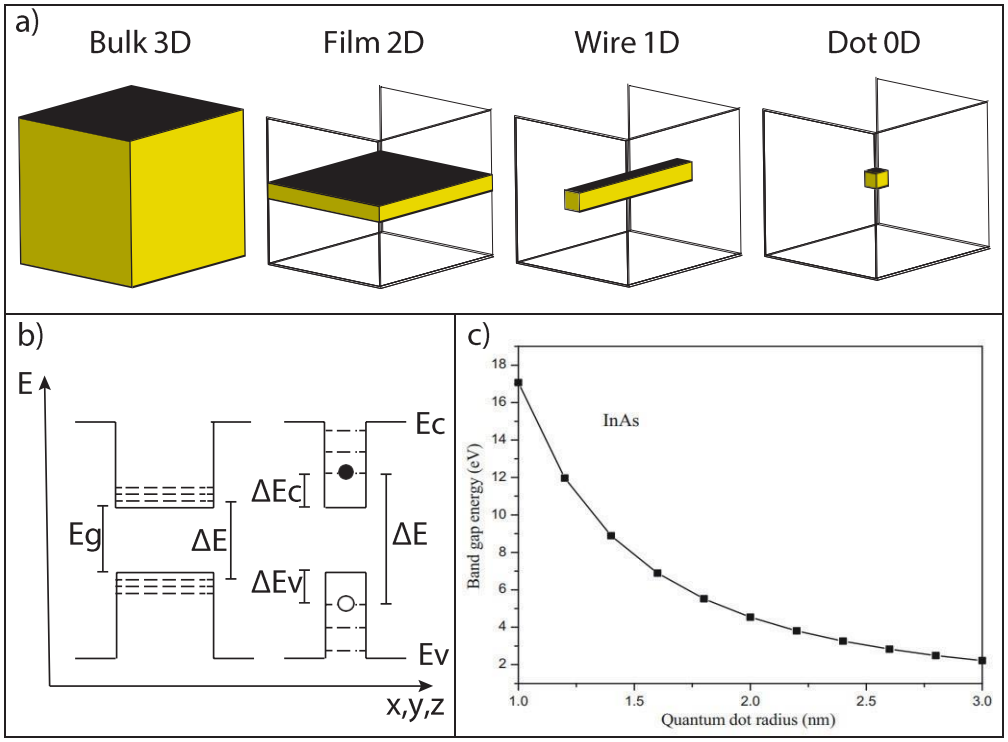

Figure 1: a) Is an illustration of a decrease in dimensions of a material, going from a bulk 3D to a dot with 0 dimensions. b) Shows an energy scheme of two different sizes of a QD, left scheme is a bigger QD than right scheme. Y-axis is the energy where x axis show the size of two different QDs. E_c is the energy of the conduction band, E_v is the energy of the valence band, E_g is the energy of the bulk band-gap, ΔE_c is the difference in energy from E_c at the bottom of the quantum well to the lowest energy state in the conduction band, ΔE_v is the difference in energy from E_v at the top of the quantum well to the highest energy state of the valence band, $\Delta E = E_g + \Delta E_v + \Delta E_c$. The electron is indicated as a solid black circle and the hole is a hollow black circle, together forming an exciton. c) is a plot of the direct band-gap energy as a function of the QD radius calculated in the work by F. Mezrag et *al.* [18], the calculation is done using empirical pseudo-potential method (EPM) on a free spherical InAs QD.

Accessing the quantum scale and the quantum phenomenons is a matter of confining the dimensions of the material to trap the wave-function in discrete states. Figure 1 a) shows

a schematic of decrease in dimensions of a material. In bulk material the wave-function is free to move in all 3 dimensions, the energy states in the valence and conduction bands are continuous and not discrete. When confining one dimension a 2D film is created and the wave-function is now free to move in 2 dimensions only, for 1D for example in a nanowire (NW), the wave-function is confined in all directions except for along the wire. For a quantum dot 0D occurs and the wave-function is trapped in all directions and can not move. Each dimension of confinement gives rise to a quantization of available energy states.

Looking at Figure 1 b) the energy scheme is shown for a large (left) and a smaller (right) QD. The matter of the wavelength of the emitted light from a QD is directly linked to the energy gap between the highest energy state in the valence and the lowest energy state in the conduction band in the material (ΔE).

$$\Delta E = E_g + \Delta E_g \tag{1}$$

Where E_g is the band-gap between the valence and the conduction band (0.35 eV for bulk InAs at 300°K and around 0.42 eV at a few degree Kelvin) [19]) and ΔE_g is the sum of, the difference between the energy of the valence band and the energy of the highest state in the valence band (ΔE_v in Figure 1 b)), and the difference in energy of the conduction band and the lowest energy state of the conduction band (ΔE_v in Figure 1 b)). This is also shown in the following equation:

$$\Delta E_g = \Delta E_c + \Delta E_v = \frac{\bar{h}^2}{2\mu}\left(\frac{\pi}{r}\right)^2 \tag{2}$$

Where $\frac{1}{\mu} = \frac{1}{m_e} + \frac{1}{m_h}$ is the reduced mass of the electron/hole and r is the radius of the QD i.e the width of the quantum well in one dimension. Following the illustration in Figure 1 b) where the energy is shown on the y axis and the size in one dimension i.e the radius on the x axis (this also represent all the other dimensions of the QD i.e y and z direction in the QD), the energy in the quantum well can be described. When a electron is excited from the valence band to the conduction band an electron-hole pair called an exciton is created. It is this exciton that creates the quantum state of the QD (see section 3.2 for a more detailed description) When the exciton decays, a single photon will be emitted, the wavelength and energy of this photon is determined by ΔE. The relation between energy and wavelength is $E = \frac{hc}{\lambda}$ where E is the energy of the emitted light, c is speed of light and λ is the wavelength. When increasing the size of the QD the energy states

will come closer to each other in the bands. This results in a lower ΔE_v and a greater wavelength. This relation can also be seen in Figure 1 c) which shows the results from F. Mezrag et *al.* [18] where the energy of the direct band-gap was calculated for an InAs QD using the empirical pseudo-potential method (EPM) as a function of the radius of the QD, note that the QD here is in free space and spherical. F. Mezrag et *al.* [18] calculations have been done for a radius from 1 nm to 3 nm, in this range it is seen that there is an exponential decrease in the energy of the band-gap. At 3 nm the energy is around 2 eV which corresponds to a wavelength of 620 nm. In this work they mention that going beyond 3 nm radius the band-gap energy tends to go to the bulk energy band-gap because the direct band-gap becoming weak. Either way the energy band-gap will go towards the bulk 0.35 eV (λ = 3542 nm) when increasing the size. The size of a SK grown QD is 20 nm to 40 nm in diameter with a height of 4 nm to 7 nm. This initially seems very large and maybe expect to reach bulk structures, but the wavelength of the emitted light is found to be around 920 nm - 940 nm ($\approx$ 1.35 eV). This is due to the strain in the QD, caused by the 7.2% lattice mismatch between InAs and GaAs, which compresses the quantum well and confines the energy states even though the size of the dot is relatively large. This indication of the strain having a major role for larger QD is reported and calculations of the energy band-gap as a function of the strain in SK QDs has been done by Pryor et *al.* [20] where the energy bang-gap for a QD with a diameter of 18 nm was found to be 1.28 eV. The strain in the SAG grown QDs grown for this thesis may play a huge role in their optical properties, but understanding the complexity of how the strain effect the energy band-gap goes beyond the scope of this thesis.

1.2.2 Stranski-Krastanov

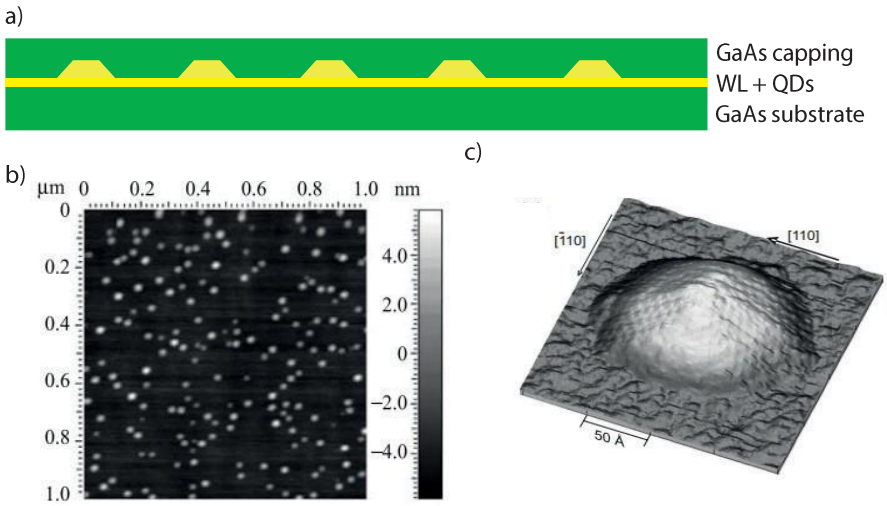

Figure 2: Shows an example of the Stranski-Krastanov (SK) growth. a) Illustration of the SK InAs QDs and InAs wetting-layer (WL) grown between a GaAs substrate and a GaAs capping layer. b) Scanning Tunneling Microscopy (STM) image of an InAs QD on a GaAs substrate, H. Eisele et *al.* [21]. c) Atomic Force Microscopy (AFM) image of SK InAs QDs on GaAs substrate without capping layer, Ju Wu et *al.* [22]

The QDs, which are mainly used for the fabrication of optical quantum devices, are grown in the Stranski–Krastanov (SK) growth mode. SK InAs QDs forms due to the 7.2 % lattice mismatch in the lattice constants between InAs and GaAs which creates strain in InAs. First, the growth of InAs occurs epitaxially on top of GaAs, where the first ≈ 1.5 monolayers (Ml) of InAs are elastically stretched to match the GaAs lattice constant. The thickness of this layer is the critical thickness below which InAs is grown without creation of misfit dislocations. This layer is also called the wetting-layer. After the critical thickness is exceeded droplets of InAs will start to form due to the accumulated strain in the system. Earlier studies show that droplets of around 20 nm to 40 nm in diameter and with a height of 4 nm to 7 nm can be formed before introducing misfit dislocations at the InAs/GaAs interface [22, 23, 24]. Substrates with SK InAs QDs prepared for near-infrared optical devices are provided with a capping layer on top of the QDs to create a quantum well. This is further discussed in Section 3.2. A simple illustration is shown in Figure2 a) of the structure consisting of a GaAs substrate, InAs QDs formed above the InAs wetting layer and a GaAs capping layer which is used both to confine the InAs QD and to passivate the surface. As seen in the SEM picture from the paper Ju Wu et *al.*

[22] in Figure 2 c) the SK QDs are randomly distributed all over the substrate. Figure 2 b) from H. Eisele et *al.*[21] shows how a zoom-in of one of the QDs could look like. The definition of the shape of the InAs QD can vary due to different growth conditions and growth kinetics. Earlier studies have shown various shapes including pyramids with the base structure of octagons, squares and cone-shape [25, 23]. A large distribution of sizes on the same growth substrate, difficulty to control position and shape results in low reproducibility hindering the potential of scaling up devices based on SK QDs.

1.2.3 Dislocation at interface

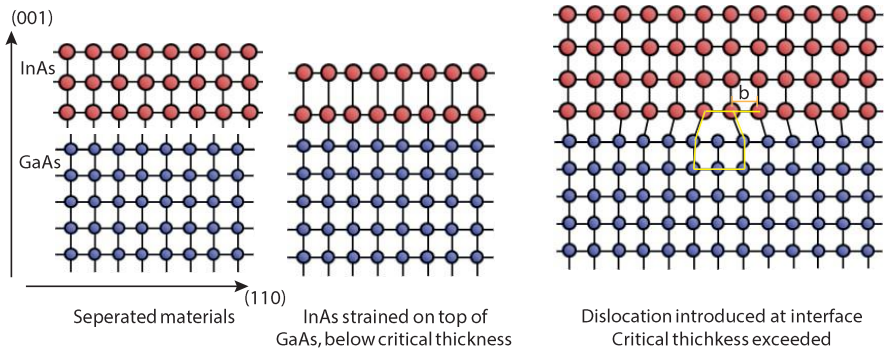

Figure 3: Illustration of the difference in lattice parameters between InAs and GaAs and how InAs is strained on top of GaAs for a few Ml before introducing dislocations at the interface when the growth thickness of InAs exceeds the critical thickness. The in-plane direction is (110) and out of plane (001). The Burgers vector b is indicated as an orange line. The illustration is taken from a web-page [26] and edited.

Figure 3 illustrates the strain in InAs wetting-layer and dislocation formation at the InAs/GaAs interface. In Figure 3 a) it is seen that the lattice parameter of InAs is larger (a_{InAs} = 6.06 Å) than the lattice parameter of GaAs (a_{GaAs} = 5.65 Å) this will cause the InAs in-plane lattice constant to compress when grown on top of GaAs. Owing the Poisson effect, the out-of-plane lattice constant expands in this case as illustrated in Figure 3 b). Due to the deformation of the lattice, the system builds in a localized strain. The misfit strain parameter is given by: $f = (a_{InAs} - a_{GaAs})/a_{GaAs}$. In percentage this gives the 7.2 % lattice mismatch as mentioned above. At some critical thickness it is more energetically favorable to introduce dislocations at the interface and start relaxing the InAs. The distance between dislocations is given by: $p = b/(f - ||)$ where b is the Burgers vector (the distance between where the atom are located and where it should be located if there were no misfits. b is equal to a lattice vector if the dislocation is precise.)

f is the misfit parameter and is the strain. If the InAs is fully relaxed (assuming | | = 0) on top of GaAs the distance between the dislocations (p) would be 8.35 nm. Each misfit dislocation reduces the overall strain in the system. When a periodic array of misfit dislocations with an expected distance p between each dislocation center is created, the mismatched material is fully plastically relaxed. This means for the InAs/GaAs case that InAs recovers its lattice parameter in the InAs above the interface.

1.2.4 Selective area growth

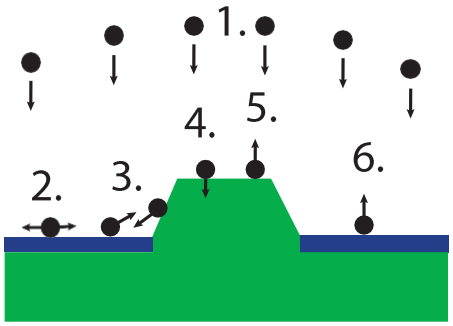

Figure 4: Illustration of the different phases of material growth during SAG growth. **1.** A constant flux of atoms dispersed over the sample. **2.** Adatoms diffusing on the mask. **3.** Exchange of adatoms between the mask and the growth window. **4.** Adatom incorporation into the crystal. **5.** Evaporation of adatoms from the crystal. **6.** Evaporation of adatoms from the mask.

Selective area growth (SAG) is a concept of growing only on the selected area of the substrate. This is done by defining a mask of e.g. SiOx on top of the substrate by using lithography and etching.

In SAG, different processes have to be considered and phases distinguished. First, the growth material is supplied from the effusion cell in the MBE as depicted as incoming flux, covering the whole sample in position 1. in Figure 4. This is called the vapor phase. Then the material adsorbs on the surface of the substrate, either on the mask or in the trenches. These adatoms can diffuse around (positions 2. and 3. in Figure 4). The material is now in the adatom phase. When the growth material is incorporated in the crystal (or mask) it is in the solid phase (position 4. in Figure 4). When the growth material is desorbed from either the mask or the growth site it is in the vapor phase again (positions 5. and 6. in Figure 4). The transition between these phases has a certain Gibbs-free energy (g) associated. For the crystal growth to begin, i.e. for the adatom-crystal phase transition to happen (position 4.) in Figure 4), the energy barrier of the transition has to be overcome, see Figure 5. Following the formalism in Krogstrup et *al.*[27] the energy barrier i.e the activation energy $\delta g^{TS}_{pq,i}$ of which have to be overcome to reach the transition state (TS) is given by the difference between the activation energy of the transition from adatom phase (p) to crystal phase (q) $\delta g^{TS,ERS}_{pq,i}$ minus the chemical potential $\delta\mu_{p-ERS,i}$, see equation 3 below.

$$\delta g_{pq,i}^{TS} = \delta g_{pq,i}^{TS,ERS} - \delta \mu_{p-ERS,i} \tag{3}$$

Where the ERS is the equilibrium reference state and i is the element e.g GaAs.

The rate of how much of the adatom flux went over the TS and into crystal phase is given by the following equation:

$$\Gamma_{pq,i} = \Xi_{pq,i} c_{p,i} \exp\left(\frac{\delta g_{pq,i}^{TS}}{K_B T}\right) \tag{4}$$

Where the $\Xi_{pq,i}$ is the number of attempts for a single atom to pass TS. $c_{p,i}$ the normalised density of atoms i (e.g GaAs) in the adatom phase. $\delta g_{pq,i}^{TS}$ the activation energy of the TS, eq. 3. k_B the boltzmann constant and T the temperature.

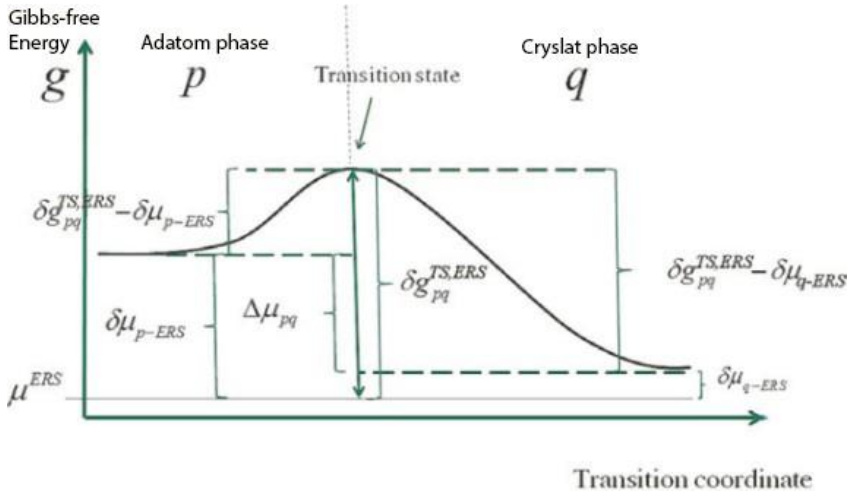

Figure 5: Illustration from Krogstrup et *al.* [27] showing phase transition from adatom phase (p) to crystal solid phase (q) with the Gibbs-free energy (g) as a function of the transition coordinate in one dimension. μ^{ERS} is the potential energy of the equilibrium reference state (ERS) $\delta \mu_{q-ERS}$ is the chemical potential of the crystal solid phase $\delta \mu_{p-ERS}$ is the chemical potential of the adatom phase. $\Delta \mu_{pq}$ is the difference in adatom phase and crystal solid phase potential. $\delta g_{pq}^{TS,ERS}$ is the Gibbs-free of the transition state TS. $\delta g_{pq}^{TS,ERS} - \delta \mu_{p-ERS}$ is the activation energy from adatom to crystal solid phase (eq. 3) and $\delta g_{pq}^{TS,ERS} - \delta \mu_{q-ERS}$ is the activation energy from crystal phase to adatom phase.

1.2.5 SAG window

The aim of SAG is to grow only within predefined openings (i.e. on the substrate) and to avoid deposition on the mask surface. The parameter describing how well this is achieved is called selectivity and is controlled by a set of growth parameters with the most important being the substrate temperature and the group V flux. Only for a certain combination of these parameters, growth will happen selectively in the trenches. The complete set of parameter combinations for selective growth can be plotted in a parameter space diagram and is often called a SAG window. For example, SAG windows have been established for InAs and GaAs in the work of Aseev et *al.* [28].

Figure 6 shows the SAG growth window presented in Aseev et *al.* [28] and the black dots added indicate the growth conditions chosen for this study (see also Appendix 7.9). In the white region above the colored region in the plots are the growth parameter settings for crystallization all over the mask. The colored region is the settings for SAG growth, i.e growth only in the openings on the substrate and the white region below is where no growth happens at all.

1.2.6 Source and sinking effects

If there is no mask on the substrate, the material will diffuse around on the whole sample before either incorporating into the substrate to become growth or desorb and leaving the substrate again. The conservation equation describes the growth of the crystal following the formalism in paper Espiñeira et *al.* [29], and for this case it is:

$$I_{a_c s,i} = f_i - \Gamma_{a_c v,i} \tag{5}$$

Where the incorporation (I) of adatoms (a) in the crystal (c) solid (s) phase growth material (i, e.g. Ga) ($I_{a_c s,i}$), is equal to the flux (f) of incoming material (i) minus the desorption rate (Γ) of adatoms from the crystal into vapor (v).

In paper Espiñeira et *al.* the growth of SAG nanowires is studied, this study is going to be the starting point for understanding the growth of the quantum dots. When considering SAG growth, the dimensions of the openings in the mask also influence the materials incorporation. In the case for a NW, the Equation 5 will look like:

$$I_{a_c s,i} = (f_i - \Gamma_{a_c v,i})wl + (\Gamma_{a_m a_c,i} - \Gamma_{a_c a_m,i})2l \tag{6}$$

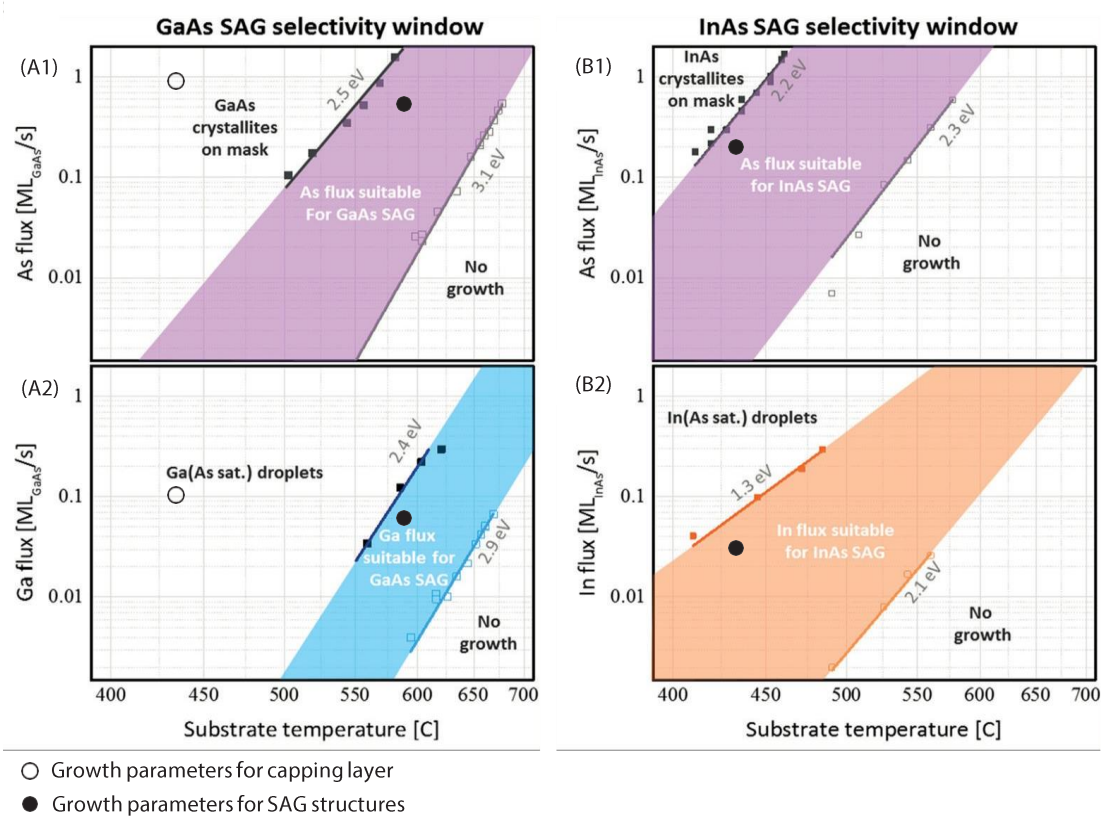

Figure 6: SAG map presented in Aseev et *al.* [28] which shows the growth parameters for GaAs (A) and InAs (B) and marks out the window for SAG. The SAG map of As during GaAs growth (A1) show the substrate temperature in degree Celsius as a function of the As flux in ML/s, (A2) SAG map of GA, (B1) SAG map of As during InAs growth and (B2) the SAG map of In. The black dots in the 4 maps are markers for the growth parameters for the SAG structures, and the hollow dots are markers for the capping layer, grown for this thesis (sample QD1121, QD1132 and QD1142), the growth parameters can be found in appendix 7.9

Where w is the width and l is the length of the NW, so the first term describes how much material is incorporated into the nanowire directly from the MBE flux. The rate of adatoms going from crystal to vapor phase again ($\Gamma_{a_c v,i}$) can be considered negligible in our case for the chosen growth temperatures and fluxes The last term describes the incorporation of material onto the NW from the battle between adatoms leaving the crystal to the mask $\Gamma_{a_c a_m,i}$ and adatoms incorporating from the mask onto the crystal

$\Gamma_{a_m a_c,i}$, (see Figure 4 3.) The equation assumes an infinitely long NW and no substrate decomposition, i.e no transition from crystal solid phase to adatom phase so that no atoms leave the crystal after they have been incorporated. When assuming $\Gamma_{a_c v,i} = 0$ the last therm in eq. 6 which consists of the exchange of adatoms across the border of the trenches, becomes the important factor when controlling the growth. This exchange rate can be described as:

$$\Delta\Gamma_{a_m a_c,i} = \Gamma_{a_m a_c,i} - \Gamma_{a_c a_m,i} \tag{7}$$

If $\Delta\Gamma_{a_m a_c,i} < 0$ the system is described as being in source growth mode. This means that there is more material leaving the growth trench than material coming from the mask surface and contributing to the growth of the NW. If $\Delta\Gamma_{a_m a_c,i} = 0$ the system is in the balances mode i.e. same amount of material is leaving as coming, and if $\Delta\Gamma_{a_m a_c,i} > 0$ the system is sinking. The sinking effect is the opposite of sourcing, here more material is added to the trench from the mask than leaving the trench. By analysing SAG GaAs NWs, Espiñeira et *al.* [29] observed a clear sourcing effect.

Under these assumptions the rate of material incorporation into the NW can be expressed as:

$$\Delta\Gamma_{a_c s} = \sum_i f_i - \Delta_{a_c v,i} + 2\frac{\Delta\Gamma_{a_m a_c,i}}{w} \tag{8}$$

Looking at Figure 7 a) it is seen that the incorporation rate is decreasing with increasing pitch, which means that the more the NW are surrounded with the mask than neighboring NWs, the more adatoms are leaving the NWs than what is being incorporated, which is an effect of the sourcing growth mode. The strength of the sourcing effect is seen when comparing the inner and outer NWs (solid and hollowed data points respectively). It was shown that in an array of four equally spaced NWs, the effect is more pronounced for the outer NWs than for the inner ones which are seen in a general lower incorporation rate for the outer than for the inner NWs (Figure 7 a)). The reason why the NW have different amount of material is that the outer ones are exposed to the surrounding mask, effectively donating the material, while the inner nanowires collect the material from the neighboring nanowires. This results in unequal incorporation: the inner nanowires incorporate more material than the outer nanowires. From a distance of 4 m pitch the incorporation rate seems to saturate. This means that the adatoms diffusion on the mask, affects the incorporation up to a distance of 4 m. This adatom diffusion length is

responsible for different strengths of sinking or sourcing behavior in an array of closely spaced NWs.

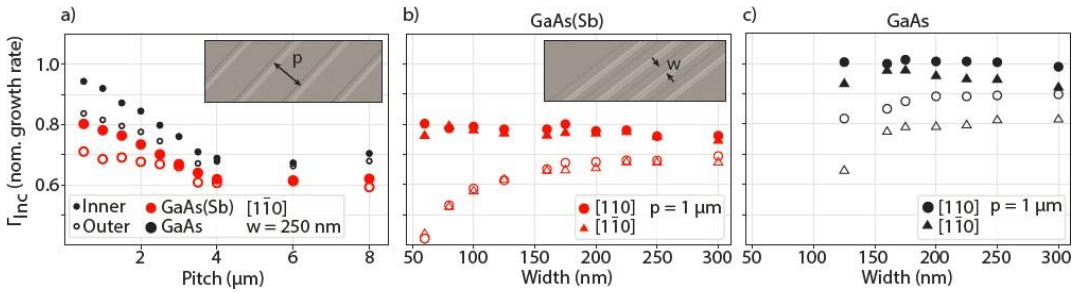

Figure 7: **a)** NW pitch study of GaAs SAG NWs. **b)** and **c)** NW width study of GaAs SAG NWs. In all cases with (red) and without (black) Sb as a surfactant. Taken from [29]

Looking at inner NW (solid) in b) the incorporation rate is not dependent on width, which means that the width of the NW does not affect the incorporation rate of the material in the NW. This means that the effect of the sourcing is the same for all NW with different size and the same pitch, and it is the pitch that changes the effect of the sourcing in the inner NW. The outer NW on the other hand shows a dependence of width, where the incorporation increases exponentially until around 150 nm width. This indicates that the sourcing effect is much stronger for the outer NWs. Comparing Figure 7 b) and c) it is seen that the surfactant (Sb) overall reduces the incorporation of material in the NW. Surfactant is also used for this study.

1.2.7 Facets and Wulff shapes

Stereographic projection (SP) is a helpful way of visualizing a 3D crystal in 2D. In general, the SP is a projection of a sphere onto a circle plane by letting the north-point of the sphere be the center of the circle plane and the equator be the edge. Projecting a point on the sphere, noted by a unit vector to the faces of the crystal, onto the circle plane, forms the SP of crystal faces. The SP of a cubic lattice zink-blend crystal in space group F-43m is shown in Figure 8. Note that the projection is not a direct projection but instead the rings represent increasing degree tilt of the facets by inclination steps of 10 degrees with respect to [001] being at 0 degrees.

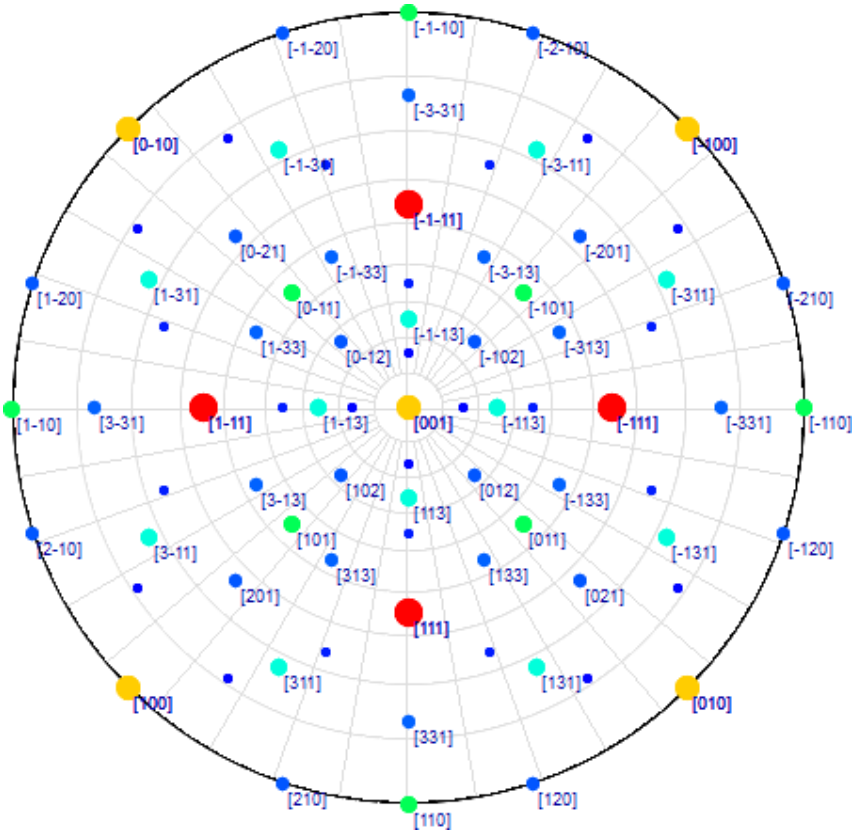

Figure 8: Stereographic projection of a cubic lattice crystal zink-blend crystal in space group F-43m made in WinWulff. The orientation is with respect to the orientation of the sample direction and the growth of the QDs

In Figure 8 the dots also have different sizes. This indicates the surface energy of the faces and the possibility for the faces to form. When the dot is big the possibility of formation is higher and the surface energy is low compared to the smaller dots on the projection. This leads us to the description of the Wulff construction. The Wulff construction is a method where a gamma-function is used to determine the surface energy of the equilibrium crystal shape (ECS). The specific surface energy of a face is given by the distance h_{hkl} (red dotted line in Figure9) from the center O of the crystal orthogonal to the face (hkl) (blue solid line, normal hyperplane) times a constant C. [30]

$$\gamma_{hkl} = h_{hkl} * C \tag{9}$$

(Note that this simple description is only for a free-floating crystal) A gamma-function represent all the energies to all distance from the center and gives the Wulff plot, but it is only the smallest distances i.e h_{hkl}, which have the smallest energies that give the equilibrium shape of the crystal i.e the Wulff construction (light blue region in Figure 9). It is important to note that finding the gamma-function is no easy task in practice. In practice the crystal is grown and studied first and from that the gamma-function is calculated [27]

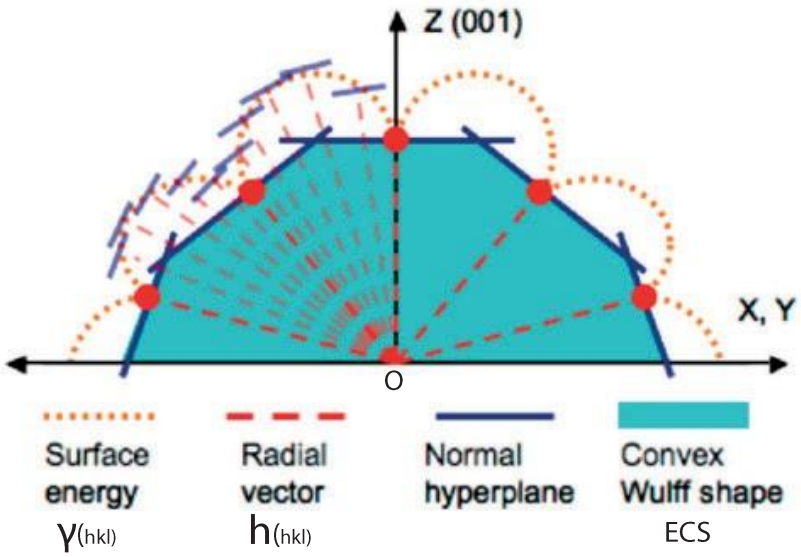

Figure 9: This figure is taken from Wong et *al.* [30] and edited

Summing all these specific surface energies gives the Gibbs-free energy of the whole equilibrium crystal shape (ECS) [31].

2 Fabrication and tools

2.1 Design

The design of the mask seen in Figure 10 was made by Charline Kirchert and Laurits Høgel using CleWin5 and the code language Lua which is a part of the CleWin5 software. The design consists of arrays of 11 identical features varying the sizes from 80 nm to 400 nm in diameter and the pitch from 150 nm to 5000 nm (the pitch is defined from center to center of the features). The increment of the size and pitch is not continuous. The design also consist of different shapes, octagons, hexagons, circles and squares, and combinations of dots and NW structures. For this study mainly octagons are considered for size 200 nm and 400 nm in diameter varying the pitch.

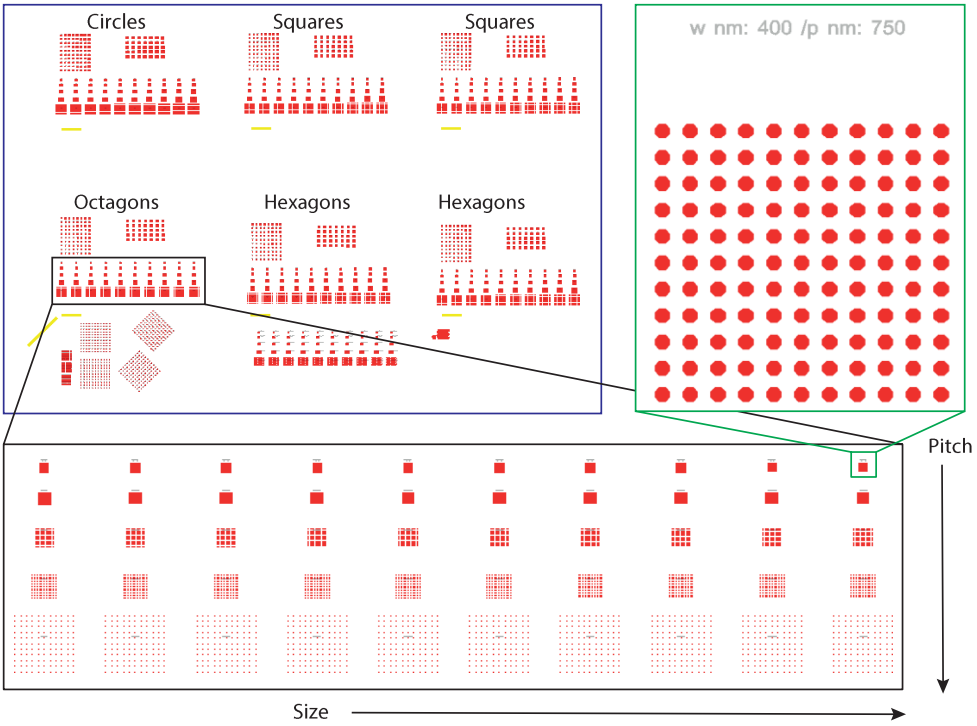

Figure 10: Design drawn in CleWin5 using Lua script showing different shapes and variation of pitch and width which increase in the pointing arrows directions.

2.2 Fabrication process

The QDs have been grown on GaAs (001) substrates (Figure 11 1.) with a mask of 10.5 nm thick SiOx layer, the SiOx layer was deposited by Gunjan Piyush Nagda at Lyngby DTU (Figure 11 2.).

For the final fabrication recipes the substrate was spin-coated with PMMA resist (CSAR) (Figure 11 3.) and exposed in the Electron Beam Lithography system (EBL) Elionix-7000 100 kV, with electron dose 600 μC/cm^2. The sample was developed in MIBK:IPA (Figure 11 4.) and wet etched in HF (Figure 11 5.), followed by strip-off, of the remaining resist (Figure 11 6.). The detailed description of the fabrication process is found in the Appendix 7.2

Fabrication step 3 to 6 (see Figure 11) was done by Charline Kirchert and Laurtis Høgel. After the strip off and cleanness check in the AFM the sample was ready to go to the Molecular Beam Epitaxy (MBE) machine for growth of the crystal structures. The growths were preformed by Daria Beznasiuk.

After the growth, the crystal structures were analyzed using Atomic Force Microscopy (AFM) and Scanning Electron Microscope (SEM) done by Charline Kirchert and Laurits Høgel, and Tunneling Electron Microscopy (TEM) were performed by Sara Martí-Sánchez.

The specific steps for the process and tools used for this project are described in the following chapters.

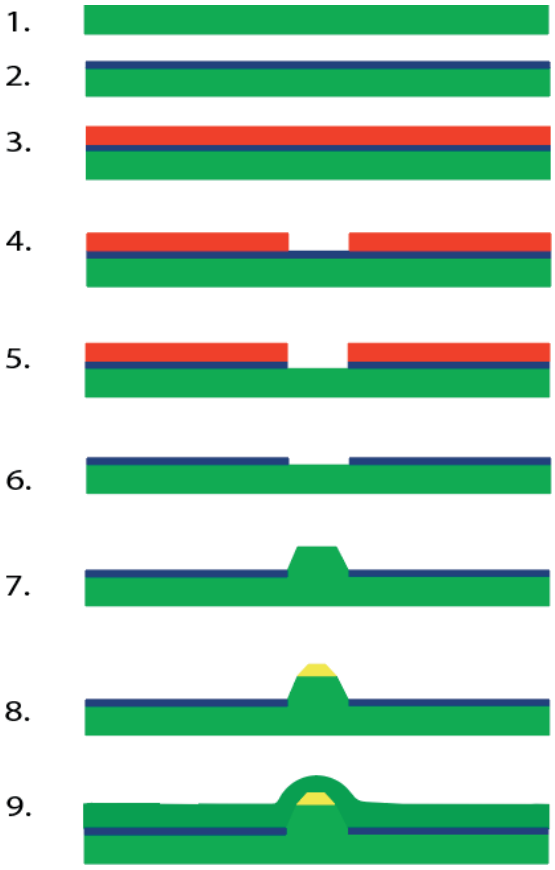

Figure 11: Illustration of the fabrication processes step by step. 1. is the GaAs (001) wafer. 2. Deposition if SiOx (done by Gunjan). 3. Spincoating of resist. 4. Development after EBL patterning. 5. Strip off of remaining resist. 6. HF etching of the mask trenches. 7. Growth of GaAs buffer dots. 8. Growth of InAs QDs. 9. Growth of GaAs capping layer. Step 3 to 6 were done by Charline and Laurits. Step 7. to 9. were done by Daria.

2.3 Electron-beam lithography

Electron Beam Lithography (EBL) [32] is the tool used for creating the mask openings of the wanted design for the substrate. EBL system Elionix7000 100kV [33] is used in this project and was operated by Charline and Laurits with exception of growth QD1104, QD1099, and QD1072 where Daria did the EBL using Elionix F-125 125kV (see Appendix 7.1. The EBL is roughly the same principle and hardware as the SEM, (see section 2.7) but the beam is more focused and the spot size is adjusted to be approximately 2 nm in diameter. Even though the spot size is only 2 nm this does not mean that the design

can get so small. For this EBL it can be possible to achieve features of around 20 nm for experienced users. When the electrons from the beam (primary electrons) hit the resist they lose their energy to the electrons in the resist by collision and inelastic scattering. This interaction produces secondary electrons with the kinetic energy high enough to break the molecular bonds in the electron sensitive resist. The secondary electrons will diffuse around in the resist (Figure 12), and it is this diffusion that determines the actual resolution and size of the pattern. The molecular structure of the resist has been changed where the secondary electrons went, which makes it soluble in these specific places in the developer chemical (MIBK:IPA). This makes it possible to create any type of pattern that one wish for within the limitations of the size control. Settings for the EBL in the final fabrication recipe are seen in Appendix 7.2.

If the pattern is too close to another pattern an effect called the proximity effect will influence the size of the patterns as well. This is the effect of secondary electrons jumping to the previous pattern written from the pattern written at the time. This effect is corrected for using the software BEAMER (version 0.6.4).

Considering the limits in the EBL spot diameter it would be almost impossible to make features of around 10 nm in width. The trenches would for that reason be too big for SAG InAs QDs grown directly in the dot openings. This is one of the reasons why the buffer GaAs dot is used for being the InAs growth site for this project, the top-facet of the GaAs buffer dot is expected to have diameters of 5 nm to 10 nm for InAs QDs to grow on.

In this project whole wafers were patterned with EBL and some exposure time could take up to 24 hours. The long exposure time concluded in the decision of making fewer guide marks which in the end made the navigating and finding the design using other instruments critical. When having a long exposure time the position of the written design could change compared to the original design, due to beam drifting occurring at long time exposures. This is considered to not be critical for this design. The long exposure time can be shortened when using Elionix700 125 kV.

Placing the whole wafer on the sample holder was challenging due to too little space and no ideal clips, this was not ideal and a small angle of rotation of the wafer would be hard to prevent. The small rotation causes a small rotation of the trench compared to the crystal orientation in the substrate. The rotation was calculated to be roughly 1° which is assumed to have no major effect on the shape of the facets formed doing growth.

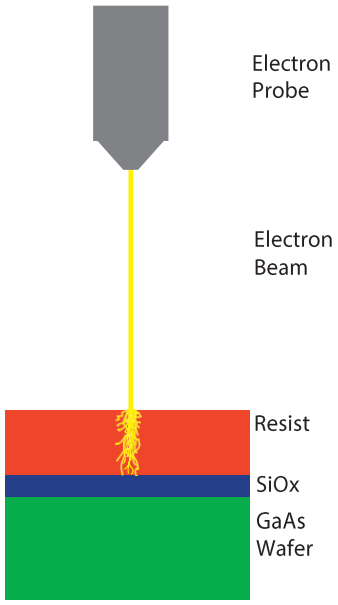

Figure 12: An illustration of the EBL process. The Electron probe/gun (gray) shoots primary electrons (yellow) at the electron sensitive resist (red). The primary electrons produce secondary electrons by inelastic scattering in the resist. The secondary electrons get enough kinetic energy to break molecular bonds in the resist (showed as random yellow lines). The SiOx layer is shown in blue and the GaAs wafer in green.

2.4 Dose Test

Following different recipes and advice before ending up with good results let the project through trying out different resists; EL9, A4 and CSAR. Finding the right dose for EBL exposure is directly connected to the type of resist. EL9 was the first try but was difficult to work with because at even fairly low doses the resist turned out to be reversed, meaning that instead of making holes after development, the resist could not be removed. After some tries trenches were made but problems with removing all the remaining resist from the trenches after the etching showed up. Switching to A4 did not solve the problem with the remaining resist left around the trenches and a third resist CSAR was tried out. CSAR ended up being the one used for the final fabrication. All resist must be gone from the substrate before loading it into the MBE chamber. The MBE can not be contaminated by organic materials.All the dose tests were verified using AFM. The trenches of the guide-marks were scanned to see if all the resist were removed so the bottom looked clean and uniform. It was not possible to verify the trenches of the small dots, see section 2.6. When doing a dose test the beam current stays the same so it is the dwelling time (time of the beam being in a specific spot) that is changed (Area dose = Beam current * Area dwell time). The doses used for the dose test of CSAR were 600 $\mu C/cm^3$, 666 $\mu C/cm^3$, 733 $\mu C/cm^3$ and 800 $\mu C/cm^3$. Looking at the guide-marks doses above 600 $\mu C/cm^3$ seems to be too much because the trenches are not a rectangle anymore but rounded.

For the last dose test using CSAR, Au deposition was done after development, this made it possible to investigate the outcome of the trenches of the dots. By doing SEM of the Au dots it was seen that trenches down to 80 nm were developed for dose 600 $\mu C/cm^3$. The dose chosen to go with for future fabrication was set to 600 $\mu C/cm^3$. A calculation of the difference in the design size and the size of the trenches after the development of EBL pattern is done in section 4.1.

2.5 Etch test

Hydrofluoric acid (HF) is used for the wet etching technique to make the trenches in the SiOx layer [34]. The solution was approximately 0.5 % and mixed by the cleanroom staff. Due to the thin layer of SiOx (10.5 nm) it is important to know the etch rate of the solution to be as precise as possible with the etching. This is crucial because the HF etching is isotropic, i.e etching in all directions (Figure 13). The etching should be to the GaAs surface but as little as possible to the sides to remain the size and shape of the trench from the resist. To calculate the etch rate, a piece (≈ 1 cm x 1 cm) of the wafer was used. To measure the SiOx thickness an Ellipsometer was used with a program model which included fitting to GaAs(001) substrate, GaAsOx and SiOx, the parameter of GaAsOx was fixed to 0. An Ellipsometer is a tool that use a laser to measure the thickness of the material by comparing the polarization of the incoming light to the reflected light from the sample. A difference of approximately 2 nm in measured thickness from the Ellipsometer to the known deposit-layer thickness is seen. The table 1 shows data from one of the etch-tests. Two measurements were taken for each etching time, for the example given here the etching times were 12 s and 25 s.

The average of the measurements were taken and the rate was calculated for each chip. $\Gamma_{etch} = (SiOx_{t=0} - SiOx_t)/t_{etch}$, where Γ_{etch} is the etch rate, t is the time, $SiOx_{t=0}$ is the SiOx thickness at t = 0 $SiOx_t$ is the SiOx thickness after etching and t_{etch} is the etching time. The etch rate average was used in the fabrication. Doing the considerations of how to calculate the etch rate, the effect of decaying etch rate over time was considered. It is seen in the measurements that the etch rate is lower for the chip etched for 25s than the one etched for 12 s. This effect is considered to be caused by the Ellipsometer being less precise, when the layer of SiOx becomes thinner. Taking this into account the rate could be calculated using this formula:

$$\Gamma_{etch_{t=0}} = \Gamma_{etch_t} - \frac{\Delta\Gamma_{etch}}{\Delta t} t \tag{10}$$

Where $\Gamma_{etch_{t=0}}$ is the etching rate at 0 s, Γ_{etch_t} is the etch rate after etching, $\Delta\Gamma_{etch}$ is the difference in etch rates at two different times and Δt is the time difference. Looking at the difference in calculated $\Gamma_{etch_{t=0}}$ = 0.3118 nm/s and the average of the two etch rates = 0.03231 nm/s (see Table 2), only a small difference is seen. This effect is estimated to be small enough to have no significance, and the uncertainty when doing manual etching is much bigger than what is seen here. A manual etching can never be this precise. Note that this example ignores the extreme case of etching time set to a value where the SiOx layer exceeds 0 nm.

	Chip 1	Chip 2
Etch time	0 s	0 s
SiOx	12.32 12.41	12.47 12.48
Average	12.375	12.475
Etch time	12 s	25 s
SiOx	8.35 8.31	4.70 4.79
Average	8.33	4.745
Etch rate	0.3371	0.3092

Table 1: Example of etch test

Etch rate Average	0.3231
$\Gamma_{\text{etch}_{t=0}}$	0.3118

Table 2: Comparing the two techniques for calculating etch rate

Furthermore due to the fact that even though the SiOx layer was 10.5 nm the number was set to 15 nm when doing the calculation for the actual etching time for the fabrication, this was done to be certain that the SiOx was etched all the way through.

At the very end of the project, the etch-test were done on chips with a thicker SiOx layer, this was not done earlier because no other wafers than the growth wafers were accessible. After the decay in rates over time was observed and discussed, a chip with SiOx of 72 nm was handed out. Etch-test for this chip was done with time increased to 1 min, 1.5 min and 2 min. The etch rate for these 3 tests was found to be 0.3484, 0.3496 and 0.3498 respectively. For these calculations the frac$\Delta\Gamma_{\text{etch}}\Delta$t is close to zero, so calculated average is also the etch-rate at time = 0. This supports the importance of the SiOx layer thickness when doing etch-tests especially if there is an uncertainty in the Ellipsometer that increases with decreasing SiOx layer. It should be noted that the rates for the two different tests (SiOx = 10.5 nm and SiOx = 72 nm) are incomparable due to the use of two different HF solutions.

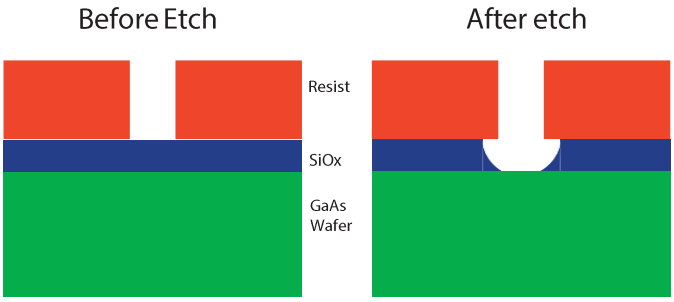

Figure 13: The illustration shows a before and after isotropic HF etch schematic. The before etch illustration shows the step after development of the resist and before etch. After etch the SiOx has been removed in a pattern characteristic for isotropic etching (etching in all directions).

2.6 Atomic force microscopy

Atomic force microscopy (AFM) is an analyzing tool to look at features in the nano-scale. The tool consists of a cantilever with a pyramidal-shaped small tip at the end, the very end of the tip at the size of a few atoms. For this project the used cantilevers is RTESTA-150 with a tip radius of 12 nm to 8 nm and a height of 10 μm to 15 μm, and SCANASYST-AIR-HR with the radius of 12 to 2 nm and a height of 5 μm. The dimensions of the tip define the minimum size scale one can image. When creating an image the cantilever either tap or drag along the surface of the sample (Figure 14 b) 1.). The atomic force interaction between the tip of the cantilever (Figure 14 b) 2.) and the atoms at the surface of the sample occurs when the tip approaches the surface. When the force is strong a current can flow and it detects that it is approaching the surface. When moving the tip line by line, i.e scanning the surface across the sample, by tapping or dragging, the surface structure is detected using a laser (Figure 14 b) 3.). The movement of the cantilever on the surface changes the reflected laser path, which goes into a detector (Figure 14 b) 4.), this information is being converted into an image that can be analyzed.

In this study the AFM has been used to look at patterns formed by EBL after the development, to verify the mask opening, development time and dose time.

It has also been used to verify the etching depths of the trenches in the SiOx and in general used for verifying the purity of the growth surface for quantum dots.

When looking at the openings in the resist after development of EBL patterned structures, one of the issues was the limit of the tip dimensions, when trying to imaging the very

bottom of the holes for smaller hole sizes. The resist was around 400 nm thick and when some of the openings are only around 100 nm in diameter, the image taken shows a tip-formed hole instead of the real form of the developed design. This does not give any proves of rather the resist is fully developed or not for the small features. To verify the development, looking for remaining resist at the trenches, the guide marks with dimensions of 10 μm by 100 μm were scanned. Because the resist is very sticky it is impossible to get sharp edges and the shape can not be trusted fully. When the etching has been done and the resist removed the AFM would image the 100 nm small holes in the $\approx$ 11 nm SiOx layer if both the development and the etching have been done correctly. When the dots have been grown in the MBE chamber the volume, height and shape are measured with the AFM as well. For every scan, it is crucial to have a good resolution i.e at least 512 lines per scan and a low frequency around 0.5 Hz, to make the scans as reliable and correct as possible.

For this project, we used gentle tapping mode with RTESTA-150 for imagining the trenches in the resist after development and the trenches after etch. Imaging with scanning mode on SiOx surface with trenches after etch will break the tip quickly, because the SiOx surface is very rough. When imagining the growth and the actual QDs SCANASYST-AIR-HR probes is used with scanning mode.

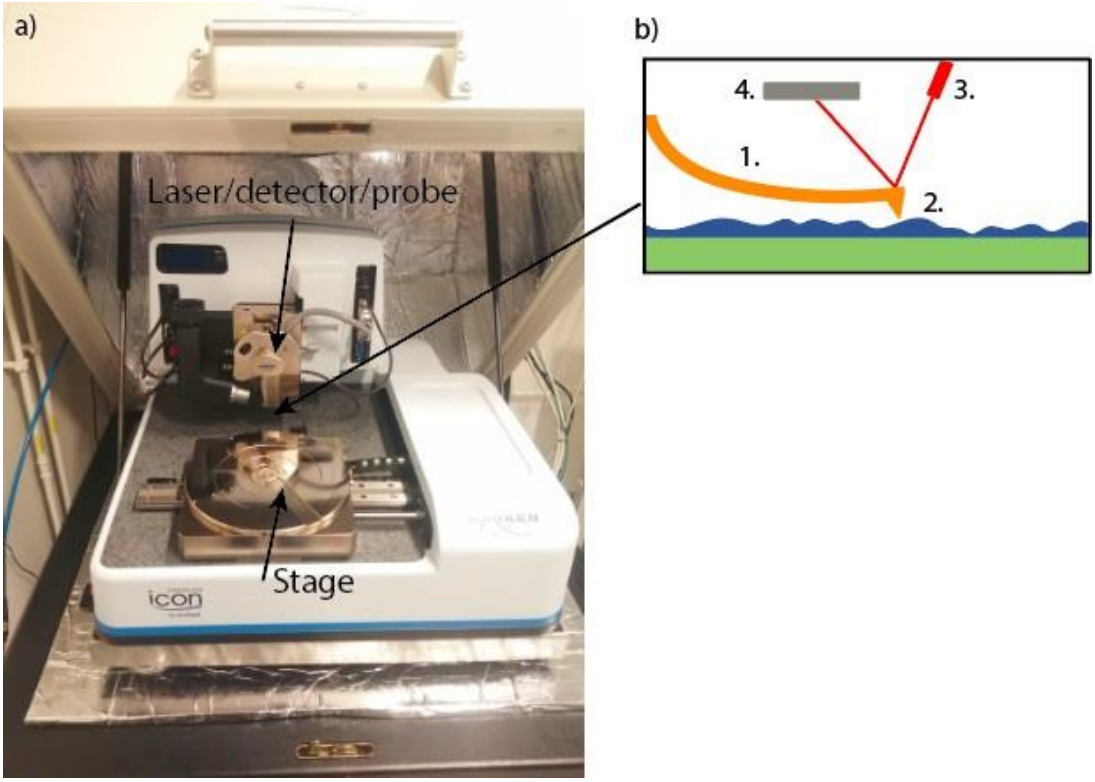

Figure 14: a) A picture of the AFM tool in the basement at HCØ, shows the stage where the sample is loaded and the holder for the laser, detector and cantilever with the probe. b) Shows a schematic of the cantilever (1.) with the probe/tip (2.) approaching the surface (blue) of the sample (blue/green). The laser (3.) reads the movement of the cantilever which reflects into the detector (4.).

2.7 Scanning electron microscopy

Scanning Electron Microscopy (SEM) was used to get a quick verification of dots faceting, growth and the quality of the growth. For this study two SEM tools were used, Jeol7800F [35] located at HCØ, which were the ones used the most, and FEI Verios G4 located at Microsoft in Lyngby. Images were taken by Charline Kirchert, Laurits Høgel and Martin Espiñeira.

SEM is a microscope which is mainly working like a regular optical microscope but uses an electron beam to form a probe and scan the sample. This allows imaging smaller objects due to the shorter wavelength of electrons.

A high electron current is extracted from the electron gun (see Figure 15 b)). The electron beam is sent through the middle of a condenser lens and an objective lens. The lenses consist of a magnetic coil which has the function of shrinking the diameter of the electron beam by changing the current in the coil. The condenser lens controls the broadening of the beam and therefore the amount of electrons passing through the aperture, which is a hole in a metal plate. This will also control the beam current. After passing through the aperture hole the beam gets its final focus and fine-tuning of diameter in the objective lens. It is this diameter of the electron beam that defines the quality of the images. The beam will now hit the sample which is attached to the stage in the vacuum chamber. The stage can move in x, y and z-direction, which select the position and resolution of the image. The stage can rotate in the x-y plane and create a tilt by rotating in z.

The electron beam hits the sample surface and electrons will emit from the sample. The secondary electron detector also known as lower electron detector (LED) or upper electron detector (UED), will collect and detect the secondary electrons emitted from the sample. For images taken by the LED, surfaces which are directly underneath the detector appear most bright and surfaces with an angle to the detector are darker. One can imagine the same light contrast with shadows and bright parts just as when a light source is shining on the side of the sample. Here the LED detector position will effectively act as the light source position. For ultra high resolution the UED detector is used combined with the gentle beam (GB) setting. The image of the structure on the sample is viewed on a computer screen.

The SEM is also equipped with a standard charged coupled device camera (CCD) in the chamber for sample navigation and preventing the pole piece protection cap from crashing onto the sample, and a set of vacuum pumps to keep the chamber around 10^{-3} to 10^{-4} Pa.

When operating the SEM the load-lock is first vented to reach atmospheric pressure. The sample is attached to a sample holder which is loaded in the load-lock. When the load-lock is closed the pre-vacuum pump pumps the chamber until the pressure is low enough to open the load-lock-chamber gate. The sample holder with the sample slides into the chamber using a manually operating handle. Before starting to focus on the sample a safety of-set (O) from the highest point on the stage to the pole piece protection cap. This is done by first setting the working distance (WD) to 10 mm, then navigating to the highest point. When having the target area in the field of view, the focus is adjusted by moving the stage in the Z direction. When the focal plane is found WD+O=Z and the of-set O is saved in the software for this SEM session. This has to be corrected at each SEM session. The next step is to find the sample and some random particles on it to adjust wobbling, astigmatism and focus. Wobbling corrects the tilt angle between the primary electron beam and the optical axis when adjusting, the beam is moving in and out of focus, if the wobbling is not set the image will not just oscillate between focus and out of focus but will also move in the x and y-direction. After the adjustment on the random particle on the sample the actual design is found and smaller corrections in the stigma and focus are done. A good focus setting can be judged in form of the visibility of the mask roughness. If beam current is changed during the SEM session the adjustment has to be corrected again. When moving around the chip the focus will also change due to small height differences. For this project, the settings for the best SEM pictures of the dots are found to be electron beam current set to 5 kV with a WD of 4 mm. The electron detector used is UED with a gentle beam (GB). During the SEM session carbon contamination can appear and can be prevented by filling liquid nitrogen into the tank from the outside of the chamber, the tank is connected with the main chamber, acting as a cryopump. This has to be done gradually and for the best result every day.

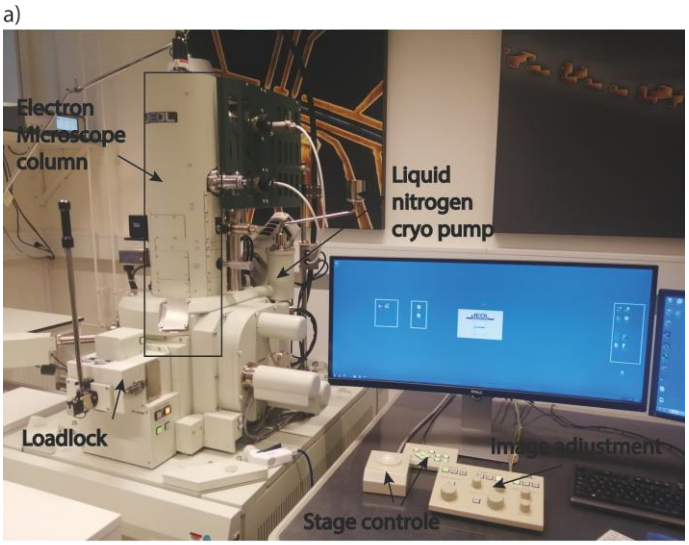

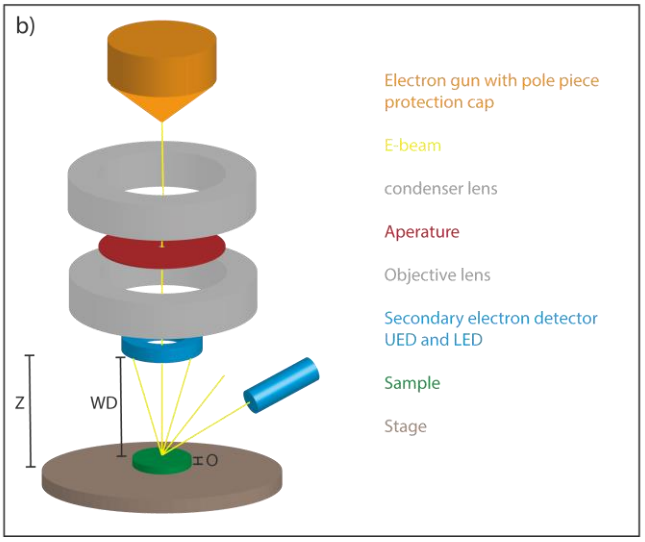

Figure 15: a) shows a picture of the SEM780F which is located in HCØ. The electron column, liquid nitrogen cryopump, load-lock, stage control and image adjustment control is pointed out in the picture. b) shows an illustration of the electron microscope column. The distance O is the highest point on the stage, WD is the working distance, the distance between the highest point on the sample and the probe, and z = WD + O.

2.8 Molecular beam epitaxy

The dot structures are epitaxially grown by molecular beam epitaxy (MBE), which was operated by Daria Beznasiuk. The MBE is located at HCØ. Figure 16 shows a schematic of the MBE chamber. The sample is loaded on a thermal stage that can rotate doing

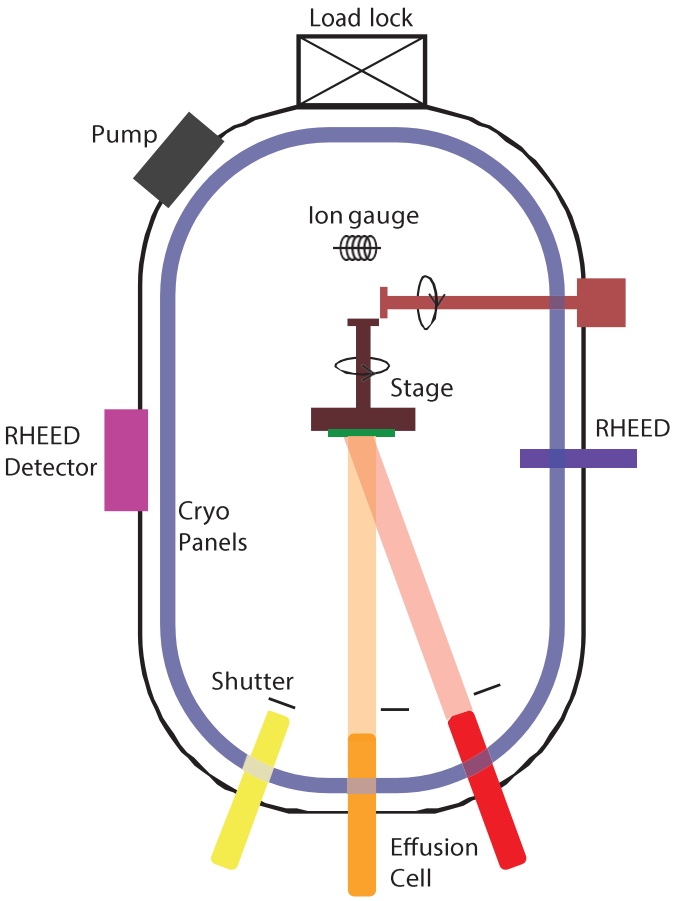

Figure 16: Illustration of the MBE chamber

growth, the rotation makes the growth uniform. The stage temperature is set to a certain value in the software but the right temperature is measured and read off at a pyrometer during growth, this temperature difference can be approximately 100 °C. The temperature on the stage is also what is defined as the temperature of the material during growth. The environment in the chamber is controlled by cryopanels and a vacuum pump. The chamber walls are cooled to liquid nitrogen temperatures (≈ 80 K) and the pressure is in the ultra-high vacuum regime, less than 10^{-7} Pa.

Effusion cells control the beam flux of the growth species and one growth species is in each effusion cell. The flux is defined by grown monolayers per second (Ml/s). When GaAs buffer layer QDs are grown, the shutters at the effusion cell with Ga and As are open. For this growth there will be an over-pressure of As in the chamber, this means that the sample is provided with about 10-20 times more As than Ga (V/III-ratio). This

can be done because the growth temperature is too high (400 ˚C - 600 ˚C) for the As to form crystals without Ga. Controlling the flux of Ga will control the growth rate. Before starting the growth the flux of Ga is measured by an ionization gauge. [36]

The MBE chamber is also provided with reflection high-energy electron diffraction (RHEED) which allows knowing the crystallography of the surface.

For this study, the growth parameters for GaAs buffer dots were chosen to target growth with early growth stage containing top-facet formation for the smallest features on the design. Two different sets of parameters were tried out but more has to be tested to target the right growth stage for the small features. The parameters are given in the Appendix 7.9.

3 Optical measurement and setup

The optical measurements were performed at the Niels Bohr Institute (NBI) by the Quantum Photonics group. Before loading the sample in the cryostat (Montana) the sample was deposited with gold markers for navigation and visibility in the camera (ThorLab, CS165CU). The Gold was deposited by Harry using AJA2 and cleaved to a 3 mm x 4 mm chip by Martin Bjergfelt using a scribe tool (LOOMIS ANLD4240) at HCØ to make the most precise cut.

The Setup was run and controlled by Ying Wang and Vasiliki Angelopoulou where Laurits Høgel and Charline Kirchert were taking over gradually under supervision.

The sample was glued with silver paste onto the center of a titanium plate to make a thermal connection between the sample and the cryostat. This was done on a heat plate to speed up the drying process of the paste. Before pumping down the pressure in the chamber, the design was found in the camera by illuminating the sample using a white light source. Before cooling down, the pressure was brought down to 5e-5 mbar at room temperature and subsequently the cryo chamber was brought down to $\approx 5^{\circ}\mathrm{K}$

Somehow the step size in The navigation software system (Daisy) is changing over time and has to manually be calibrated. This is done by measuring a known length of the guide mark in unit lengths of the step size.

3.1 Setup

In Figure 37, an illustration of the setup for the optical pathway is shown. The Tsunami laser is sent through a fiber and a coupler lens before going to the beam walk made of two mirrors, first a $\lambda/4$ and then $\lambda/2$ mirror. The beam walk is there to control the beam path enabling to send the beam spot profile and position centered right on the sample, thereby the maximal coupling efficiency can be reached. After the two mirrors there is two lenses These two lenses are for controlling the focus of the beam so the correction of the position of the beam gets easier.After the lens two wave-plates are introduced, a half wave-plate (HWP) and a quarter wave-plate (QWP) to control the input beam polarization and align it with the polarization of the QDs.

The laser transmits now through a 90/10 beam splitter (BS). This BS is there to enable having a white light source for the camera to illuminate the structures on the sample. The white light is reflected and follows the same path as the laser. The laser beam gets reflected from a 90/10 BS onto a mirror mounted on top of the cryostat and is rotated

in the z-direction so the beam reaches the sample from the top. The QDs emit light and the emitted light is collected straight above the sample. The emitted light and laser beam go back the same path and get transmitted in the 90/10 BS. A long-pass filter (900 nm) is installed after the BS, to filter the excitation laser and only allows the emitted light to pass through, the emitted light is expected to have a longer wavelength due to the expectation of the size of the dots being bigger than SK dots (see section 4.3 and 5). The emitted light passes through a lens before reaching a 50/50 BS where half of the light gets reflected into the camera and the other half transmitted further to another beam walk. two final pair of mirrors, that will couple the emitted light from the QDs into a coupler lens before reaching the spectrometer. When looking at the spectrometer the Long pass filter is removed.

The QDs were detected by the camera and showed luminescence when using the laser (Tsunami) at maximum power (unfortunately the power can not be specified due to no readout available). The wavelength of the Tsunami was set to 790 nm to do above-band excitation (which is described in section 3.2) due to the missing information of the size and wavelength of the QDs at the time of the experiment.

Even though the beam was well aligned. The spectrometer did not detect anything from the sample. This was caused by the silicon CCD inside the spectrometer which has very low quantum efficiency for wavelengths above 1000 nm and the grating which is also wavelength dependent (see also section 4.4).

The presumption of the QDs wavelength being above 1000 nm, made it impossible to use fiber coupling to the spectrometer, because they were limited to max 980 nm. This results in performing a free space path to couple to the spectrometer.

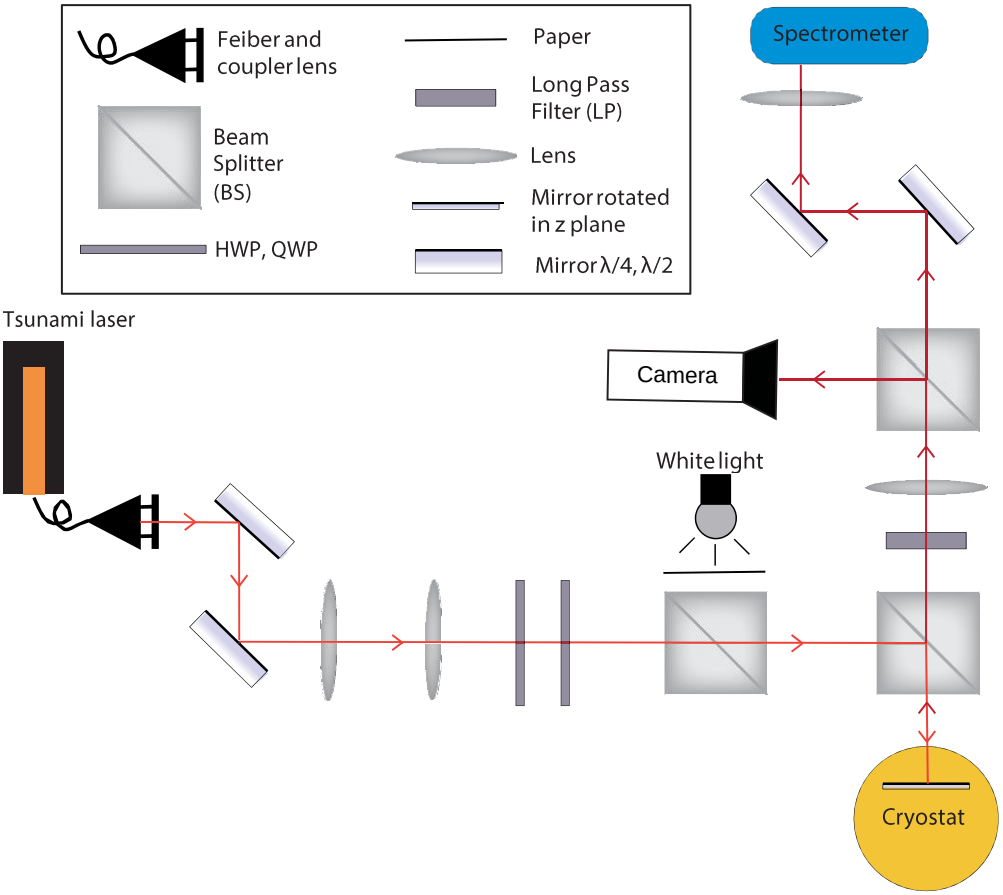

Figure 17: Illustration of the optical table

3.2 Above band gab excitation

When performing a photo luminescence (PL) experiment the laser wavelength has to be chosen to fit the energy of the band-gap (ΔE) to excite the electrons from the valence band to the conduction band. When the energy band-gap is not known, an Above-Band (ABB) excitation has to be done. The excitation laser (Tsunami) was set to a wavelength (790 nm) with much higher energy than what is needed to excite the electrons in the valence band to the conduction band in the InAs. Figure 18 shows an illustration of the energy bands for the valence and conduction bands for both the SK-grown QDs and the SAG-grown QDs. The growth structure creates a quantum well that contains discrete energy states in the InAs if the confinement is small enough i.e creating a QD of 0 dimensions. The laser will cause the electrons in GaAs to get excited from the valence band to the conduction band of GaAs and form an electron/hole pair. (The

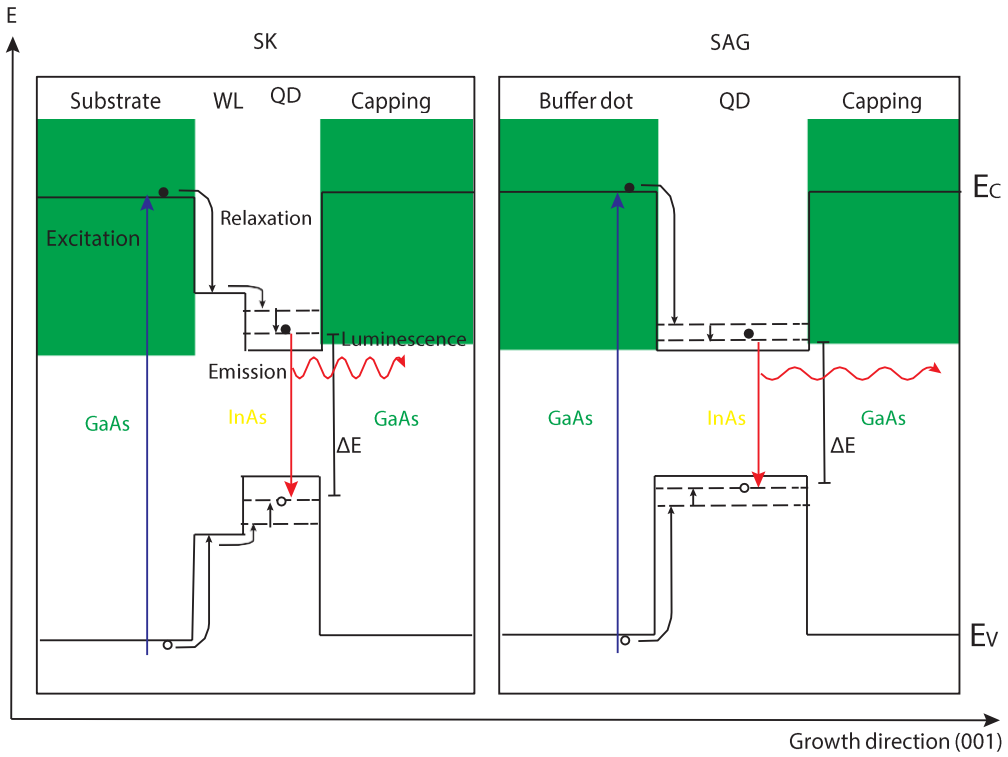

Figure 18: Illustration of the energy band structure along the growth direction (001) for InAs SK QDs and InAs SAG QDs. The excitation laser is indicated with a blue arrow, relaxation with a black arrow and emission from dots with a red arrow where the photon luminescence is the red curved arrow. The electron is illustrated as a solid black circle whereas the corresponding hole is illustrated as a hollowed black circle. Due to the difference in energy bands from GaAs to InAs the structure of the growth forms a confined quantum well with discrete states in the QD. ΔE is the energy difference between the lowest energy level of the conduction band (E_c) and the highest of the valence one (E_v).

phenomenon will be described using the electron as an example but the hole describes the same physics with a reversed sign. The hole can be thought of as a positive electron.) From the conduction band in the GaAs the electron will either do non-radiative decay (relax) into the InAs conduction band or do radiative decay (PL) back to the valence band of the GaAs. This relation defines whether we will see PL from the GaAs substrate or the InAs QDs. The electrons which relax into the conduction band of the InAs will do PL and emit a photon. This photon can be detected by the spectrometer and the wavelength of this defines the band-gap energy.

The band-gap of GaAs is much larger (1.42 eV in bulk at 300°K) than the band-gap for InAs (0.36 eV in bulk at 300°K)[19] which make it possible to do ABB excitation. This is a good procedure when the band-gap of InAs is unknown but once you have the wavelength measured in the spectrometer the laser can be set to the right wavelength to only excite the InAs QD. To have a QD there has to be confinement in all directions (as described in section 1.2.1) but the confinement in the z-direction (growth direction (001)) is the biggest due to the height being so small (2 nm - 7 nm) compared to the diameter (10 nm - 40 nm).

Due to the size of the SAG InAs QDs seem to be bigger than the SK grown QDs in this project, the wavelength of the SAG QDs is expected to be longer than the originally expected wavelength for SK QDs around 920 nm - 940 nm.

4 Analysis and results

4.1 Growth mask

a) SEM 150 nm x 650 nm pitch

b) AFM 150 nm x 600 nm pitch

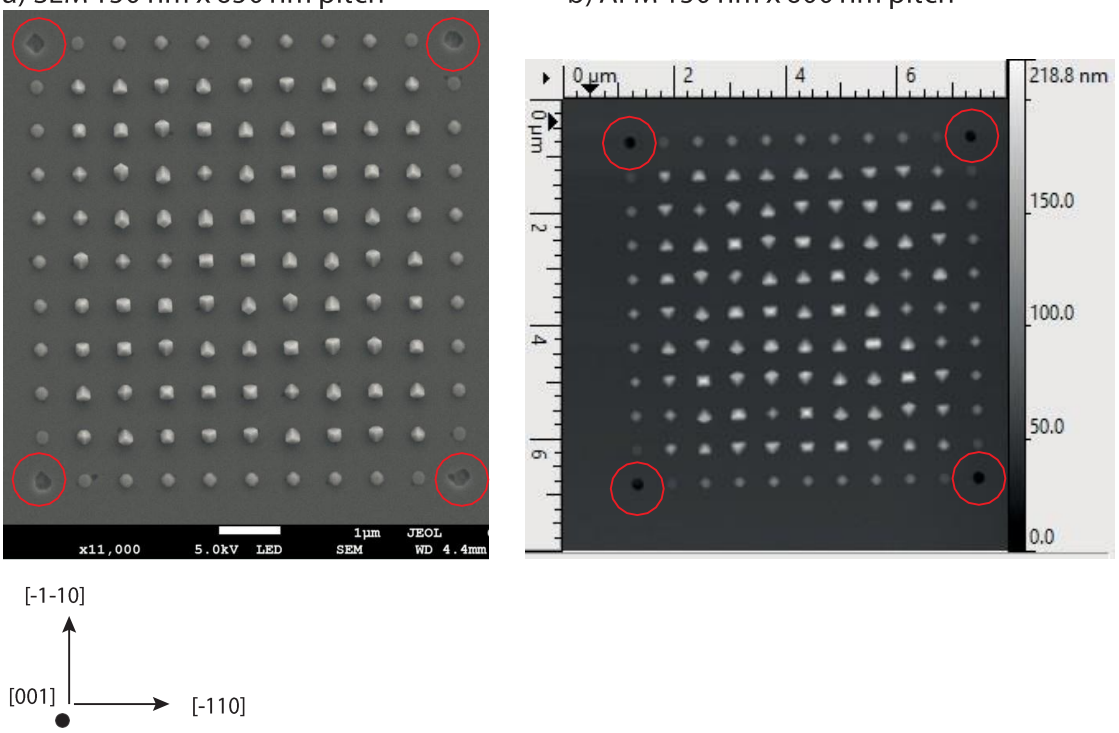

Figure 19: Sample: QD1121 after GaAs buffer dot growth. a) SEM image of 150 nm design diameter 650 nm pitch. b) AFM image of 150 nm design diameter 600 nm pitch.

When looking at SEM images of the array after the growth, it is seen that the regions where the GaAs buffer dot has not grown above the mask surface (corners in Figure 19 a)) does not appear uniform and circular/octagonal but of a more random shape. The appearance of uniform shaped holes in the AFM picture of the same 150 nm design diameter in Figure 19 b) confirms that the random shape of these holes seen in the SEM image are not caused by fabrication steps like EBL or etching but is a result of the growth in the MBE. Due to the MBE chamber not having hydrogen cleaning before growth but using thermal annealing instead, some of the GaAs will disorbe from the substrate under the SiOx opening. This will cause the holes to appear non-uniform when looking at the SEM images because the edge of the SiOx opening is not visible. This is also seen as randomly formed black spots next to the growth structure which really is small pockets without GaAs. This is also confirmed when looking at the TEM images in

section 4.3.

4.1.1 Proximity effect of EBL

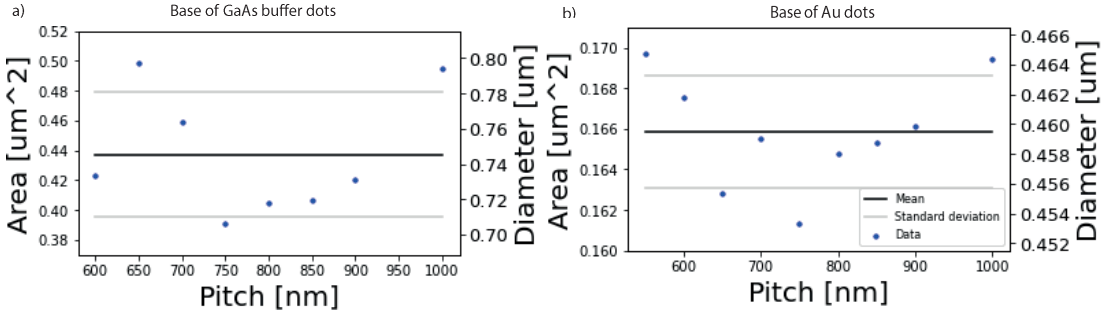

Figure 20: a) and b) show AFM measurements of the area of the GaAs buffer dot and the Au dots base in μm^2 in dependence of the pitch. The measured points are shown as blue dots, the mean value as a black line and the standard deviation in gray lines. The approach for the measurement is seen in Appendix 7.5.

To see, whether the proximity effect influences the size of the openings when doing lithography, measurements of the opening were done in different ways for different pitches. If no change in the size of the opening, depending on the pitch is seen there is no influence of the proximity effect. Three different measurements were done to investigate this effect. Figure 20 a) and b) show measurements from AFM images of the base area of the GaAs buffer dots and the base area of Au dots, respectively for 400 nm design diameter. The measurements were done by subtracting the area without the dots from the full area and division by the amount of dots in the array (121 dots) (see also Appendix 7.5). Both of the plots show a decreasing trend in the area (blue dots) from 550 nm to 800 nm pitch (with exception of 600 nm pitch for the GaAs buffer dots) and an increase again from 800 nm to 1000 nm pitch. This could indicate the proximity effect seen for pitches below 800 nm pitch. It has to be noted that for base GaAs buffer dots the increase from 600 to 650 is almost as big as the trend, which makes the trend less valid. When there is no proximity effect we would expect data to be on a flat line but we see a decrease up to 800 nm and an increase after 800 nm pitch which does not follow the expectations of no proximity effect.

The mean (black line) and standard deviation (gray lines) are indicated in both plots a) and b) to investigate the variation of the measured data. For the diameter of GaAs buffer dots the relative standard deviation (RSD = standarddeviation $*$ 100/mean) is 4.4 %, which means that the mean value of the data has a precision of 4.4 % within the data

set. In other words, the measured area of the base GaAs buffer dots lies within 4.4 % of the mean value. The aim is to make this percentage as small as possible so the spread of the area becomes less and closer to the mean value to get a more uniform size distribution dependent on the pitch. For the base diameter of the Au dots RSD = 0.8 % which means that the mean value is more precise and spread is smaller than for the base GaAs buffer dots. This indicates that the size of the base of the GaAs dots gets more distributed in the fabrication steps (e.g the etching step) or the growth after the lithography. It is hard to say if the trend seen is caused by the proximity effect only or also could be caused by development time and beam current settings. But having two measurements showing the same trend before and after growth indicate that the proximity effect or other parameters play a role in the variation of sizes dependent on the pitch. To get a better insight into this trend more measurements could be done for other sizes and pitches, and individual dots for each size should be measured to get the variation of size within one array.

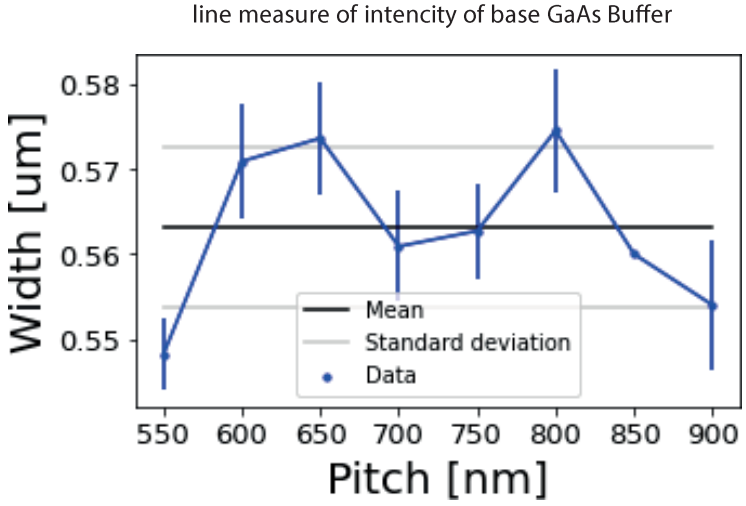

Figure 21: Plot of width in μm of the GaAs buffer dot base dependent on the pitch in nm, measured using intensity in SEM images. The blue dots show the measured widths with an error-bar showing the standard error of the mean. The black line is the mean value and the gray lines are the standard error. The measurement is of low statistical value due consideration of only eleven dots for each pitch. The approach for the measurement can be found in Appendix 7.8

.

Furthermore, a measurement of the base of the GaAs buffer dots was done using the intensity peaks in SEM images (see Appendix 7.8). Figure 21 shows a plot of the measured

width of the base GaAs buffer dependent on the pitch. The width is measured for only one line of dots through the middle of the array for each pitch. The standard error of the mean for each measurement is indicated as error-bars, the mean value as a black line and the standard deviation as gray lines. Here the trend noted in Figure 20 a) and b) is not seen and the RSD is 1.7 %. This result does not indicate any sign of proximity effect or the trend seen in the other two measurements mentioned above, this could be due to less amount of data, where the trend might show up if the measurement were taken for all 121 dots.

4.1.2 Calibration factor for EBL

From the dose test where Au deposition was done, a calibration factor of 1.21 was found (an increase of 21 % from the original design to the actual size). It was calculated under the assumption that the Au dots match the trenches in size and shape after development. It is observed that the hexagon shape of the Au dots is preserved down to 230 nm (see Appendix 7.6). The sharpness of the edges of the shape depends on the proximity effect and scattering of electrons in the resist and the development time. The calibration factor was found by calculating the mean value of 22 data points for 6 different sizes. A single data point is a measurement across the Au dot (hexagons) from corner to corner, done by manually measuring SEM pictures in Fiji (ImageJ) (see Figure 22 b)). The difference in measured diameter and the design size is found and plotted in Figure 22 a) as blue data points. After the measurements were done it was observed that the size of the design was defined from edge to edge and not from corner to corner for the hexagon structures. This results in choosing to measure the size of the design from corner to corner instead of redoing all the measurements of the SEM pictures. The values and results are shown in Table 3 and 4. Figure 22 shows a plot of the trench diameter of the design on the x-axis as a function of the mean value of the measured diameters of the Au dots. The blue points are the measured data points that seem to have a linear dependence which is shown by a linear fit of the data going through zero (black line). The orange points are the diameter of the design times the calculated calibration factor of 1.21. The slope of the fitted line is 1.217 which gives an increase of 22 %, this value and the measured value seem to match well. In conclusion assuming that the calibration factor does not change with different design shapes and that the proximity effect of the EBL is calibrated right using BEAMER, the increase in size of 21 % has to be taken into account when the size of the buffer dots should be controlled.

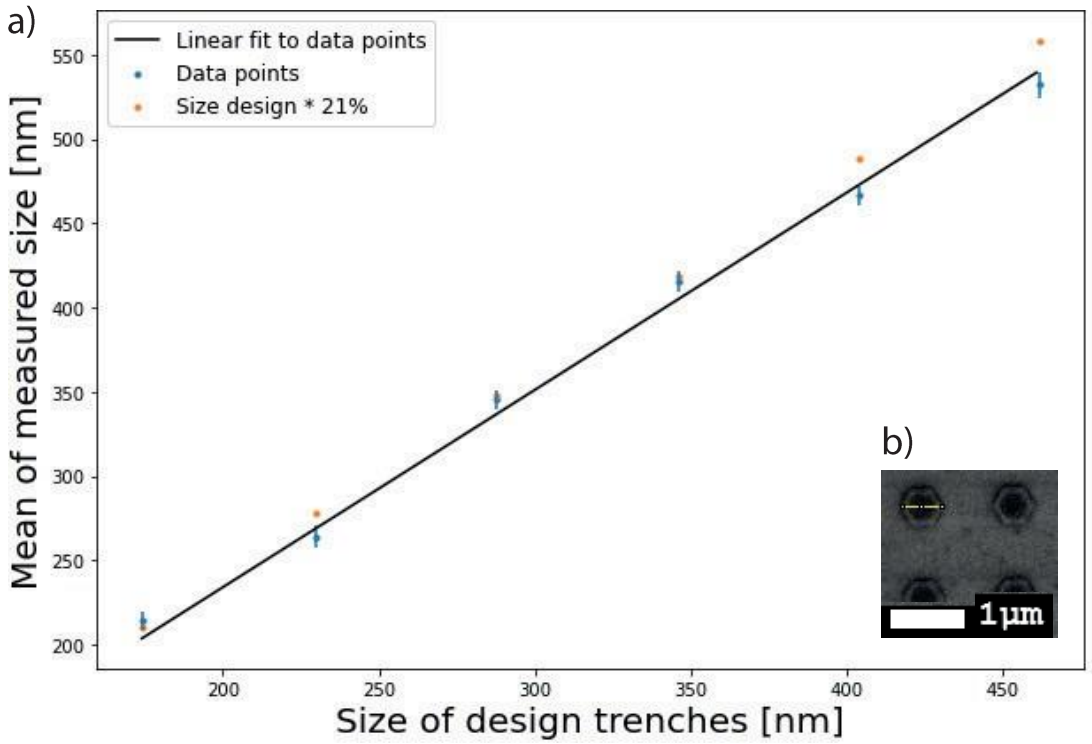

Figure 22: The graph a) shows the correlation between the width/size of the design patterns and mean value of the measured widths/sizes of the Au dots. The Au dots are assumed to be a direct imprint of the openings after development of EBL exposed resist. The blue data points are the measured data points plotted with a standard error of the mean. Orange points are the original design size times the calculated average 21 % calibration factor between design and actual size of trenches. The black line is a linear fit to the data points going through 0. The inset b) shows a cropped SEM picture of the Au dots with a yellow line that indicates the method of measuring the size. It has to be noted that the shape of the Au dots is hexagons and not octagons. Due to this fact where the position of where the measurement was taken correspond to precise but oddly displaced numbers of the design size.

Design Size	174	230	288	346	404	462
Size Difference %	23.0	14.7	19.9	20.0	15.4	15.1

Table 3: Size difference in % from design size to measured size of Au dots

Average difference %	20.9
Slope of fit %	21.7

Table 4: Comparing the calculated difference and the slope of the fit

4.1.3 Etching distribution

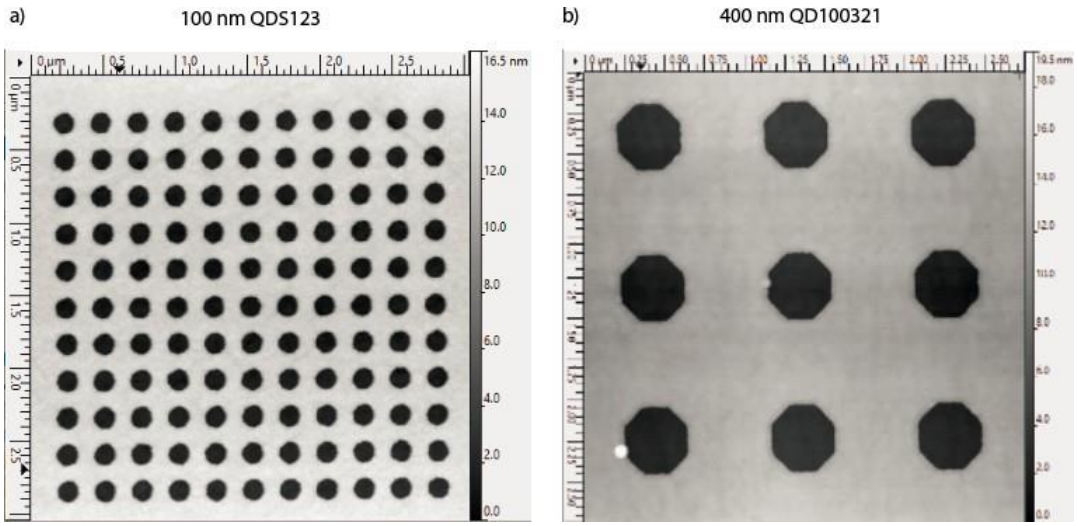

Figure 23: AFM images after HF etch. a) 100 nm design diameter 250 nm pitch from sample QDS123. b) 400 nm design diameter 800 nm pitch from sample QD100321.

Figure 23 a) and b) show AFM images of the openings after HF etching for 100 nm design diameter and 400 nm design diameter, respectively. It is seen that the designed octagon shape for the 400 nm has been accomplished but has not for 100 nm. The shape of the openings seems more stochastic for the 100 nm than for the 400 nm which will play a role in the facet formation during growth. The sharpness of the shape depends on the EBL, development and the etching technique. In Figure 24 and Figure 25 the stochastic behaviour of these two opening sizes are plotted.

Figure 24 shows measured area and diameter estimates extracted from an AFM scan, of

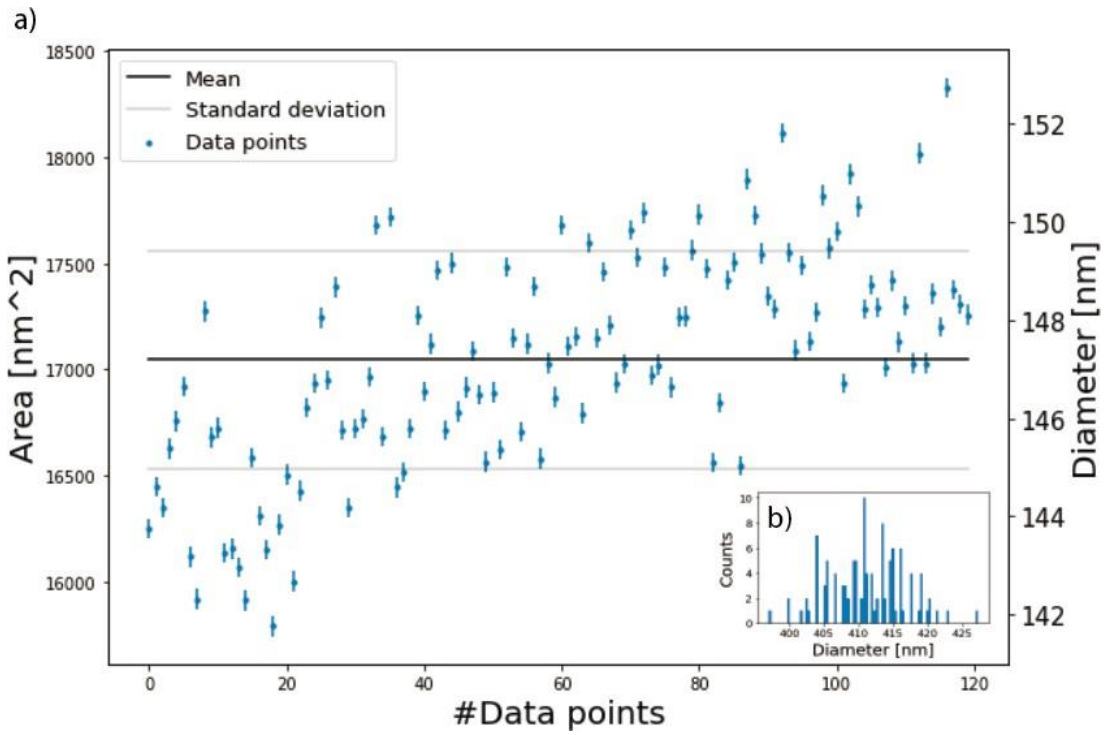

Figure 24: Sample QDS123. Measured area [nm^2] from 100 nm design diameter AFM data, of every opening in the mask (121 holes) within an array after HF etching. a) Shows the data points in blue with error bars (standard error of the mean), the mean diameter (147 nm in black and the spread (standard deviation = 2.2 nm) in gray. b) Shows the same data plotted as a histogram with bin = 100.

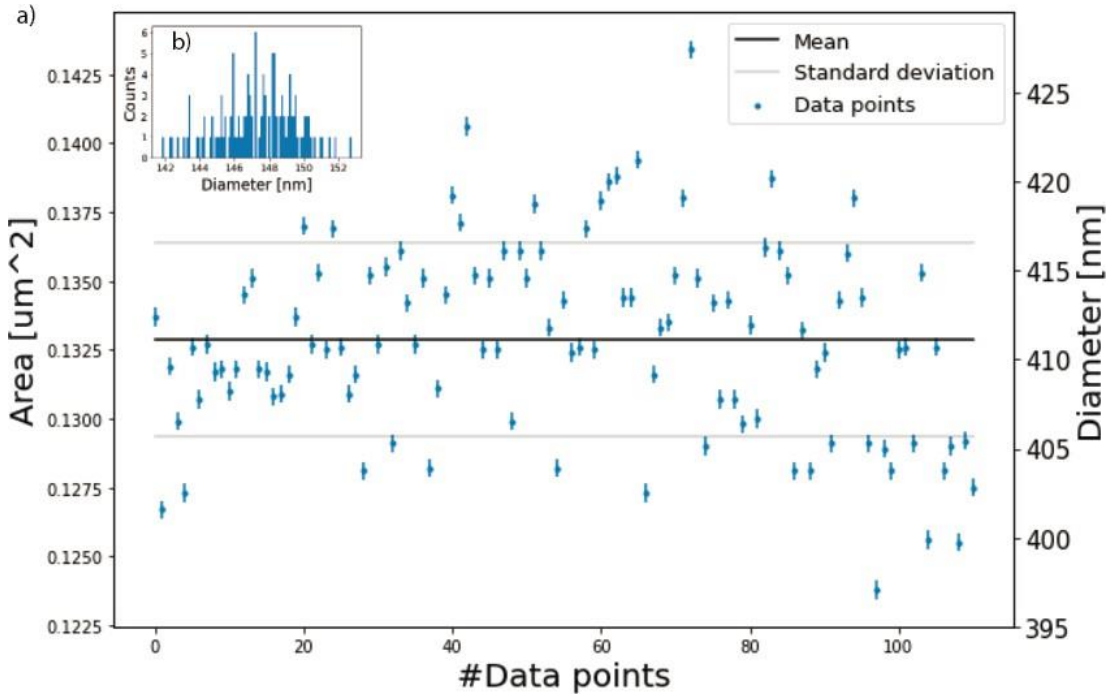

Figure 25: Sample QD100321. Measured area [um^2] from 400 nm design diameter AFM data, of every opening in the mask within an array after HF etching. a) Shows the data points in blue with error bars (standard error of the mean), the mean diameter (411 nm in black and the spread (standard deviation = 5.4 nm) in gray. b) Shows the same data plotted as a histogram with bin = 80.

the openings after etching for all 121 holes in one array for 100 nm design diameter. a) and b) are a plot of all the measured sizes and a histogram of the same data respectively. Both of the plots show a distribution of the hole size varying with ≈ 10 nm from the smallest to the biggest opening. a) shows the mean value as a black line and the standard deviation as gay lines. The relative standard deviation (RSD) is 1.5 % which means that the measured sizes are within 1.5 % of the mean value of ≈ 147 nm in diameter. To make the mask openings as precise as possible we would the RSD to be as small as possible.

Figure 25 shows the same kind of data set as Figure 24 but for 400 nm design diameter. These results show a mean diameter of 411 nm width, a standard deviation of 5.4 nm and a RSD of 1.3 %. The data for 400 nm deviates less from the mean value (1.3 %) than the data with 100 nm (1.5 %) but this difference does not seem to be of a big

enough significance to conclude that the precision depends on the size. Furthermore it should be noted that the two figures can not be compared directly since it is from two different samples so the etching time is not identical. considering the broadening in the distribution histograms the amount of measured points does not seem to be enough for strong statistics.

4.2 GaAs buffer dots structure

4.2.1 Defining the facets and shapes

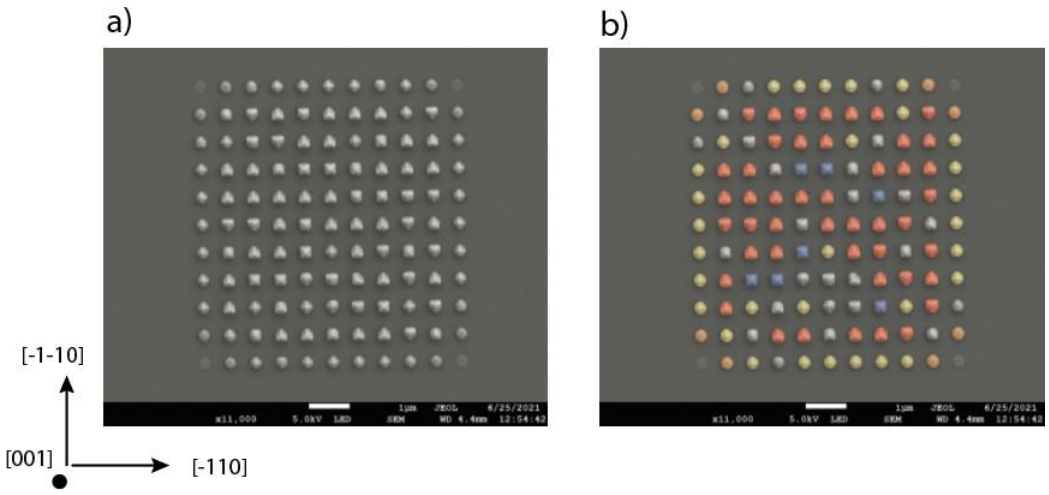

Figure 26: a) and b) is a SEM picture of 200 nm width and 600 nm pitch without and with false colors to shapes respectively.

One of the first things to note when looking at the array of buffered GaAs dots for 200 nm width and 600 nm pitch in Figure 26 a), is that they grow in different shapes within the same array. The shapes have been assigned to four different groups namely octagons with top-facets in orange, octagons with no top-facets in yellow, pentagons in red and squares in blue, which correspond to different growth stages (see Figure 26 b) and Figure 27 for the color code). There are also shapes that seem to be a mix of some of the defined four shapes, these are not categorized for simplicity.

The different shapes have been categorized according to their faceting. The facets are defined by measuring the angle of the facets with respect to the substrate plane (corresponds to the (001) plane) using the software Gwyddion, and comparing the angles with the stereographic projection (see Appendix 7.3). The first shape (growth stage 1, Figure 27) is a 4-fold crystal in the the family of {110} and {111} facets. The second shape (growth stage 2) has a 4-fold symmetry with facets only from the {110} family. The third shape (growth stage 3) has a 4-fold symmetry faceted only in the {111} family. The fourth shape (growth stage 4) has a 1-fold symmetry consisting of two facets in the {110} family and one from the {111} facet family.

The shapes classification into different growth stages is done by measuring the GaAs buffer dot volume under the assumptions of independent growth rate. The local growth rate must have a negligible influence on the shape. The main influence on the shape is here the volume of the material incorporated and the substrate temperature. The volume corresponds directly to the growth stage so that the larger the volume the more advanced the growth stage (see Figure 27).

Dots located at the edges of the array grow slower than the ones in the middle of the array, owing to the strong sourcing effect where the adatoms escape to the surrounding mask instead of incorporation into the dot. These dots are at the beginning of their evolution and of growth stage 1 and 2 where the inner ones are at later growth stages 3 and 4 and growth stage 1 and 2 are not represented, which is a result of the sharing of the escaping adatoms between neighbors. This is also seen for NWs which is explained in section 1.2.4. The volumes given in Figure 27 are the mean value of the measured volumes in the 200 nm dots with 600 nm pitch for each shape.

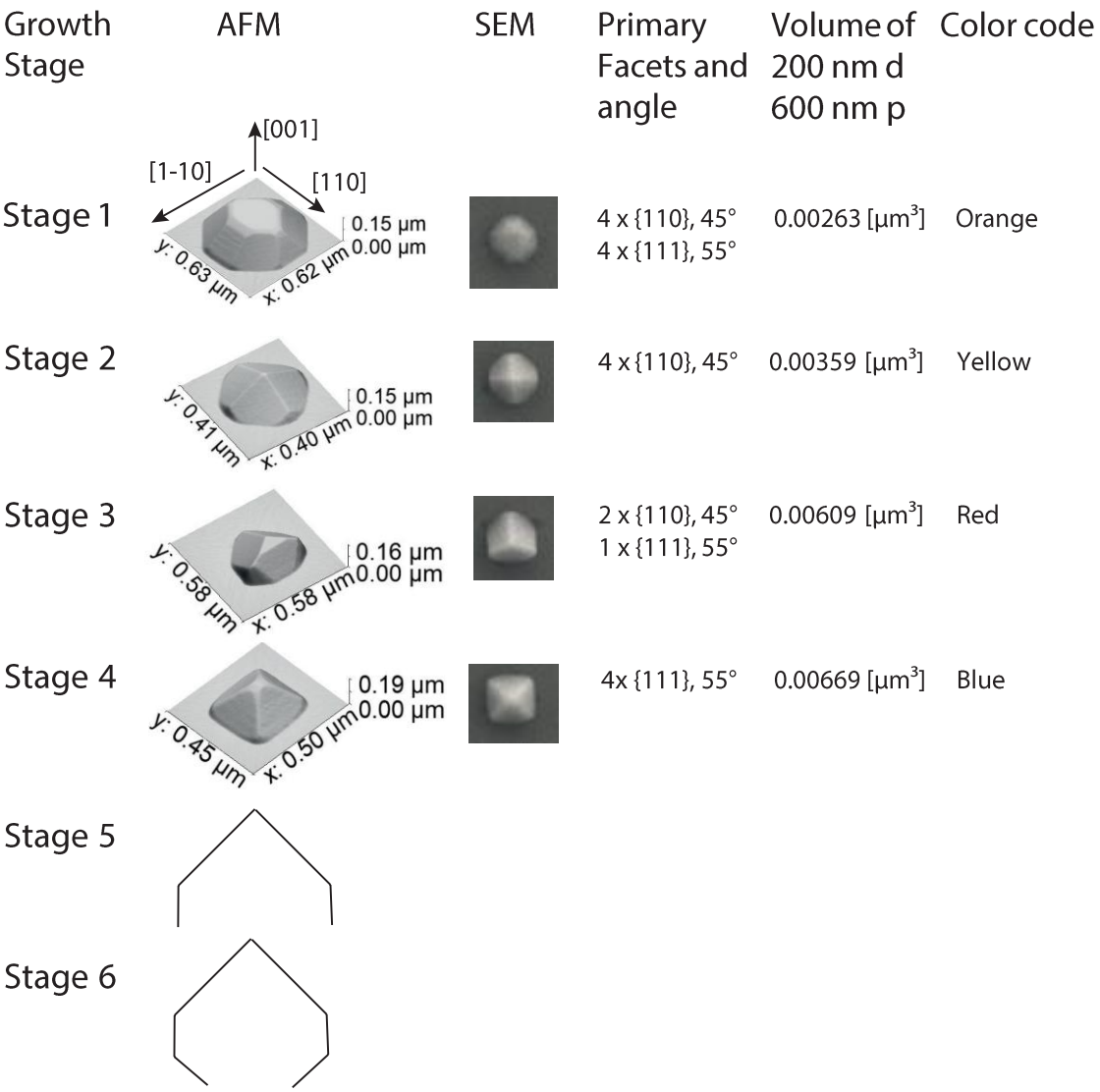

Figure 27: Schematics of the evolution of GaAs buffer dots under the assumptions of independent growth rate. Stages 1-4 are directly observed on the array of QDs from Fig 1 and accessed with AFM and SEM while stages 5-6 are illustrations made on the assumption of the minimization of the surface energy of the crystal. The crystal directions, major facets, the measured volume [μm^3] of the dot for 200 nm 600 nm pitch and the color code from Figure 26 are shown. (The AFM image of stage 1 is taken from a 400 nm dot with 600 nm pitch for better visibility of the shape).

4.2.2 Growth stage evolution

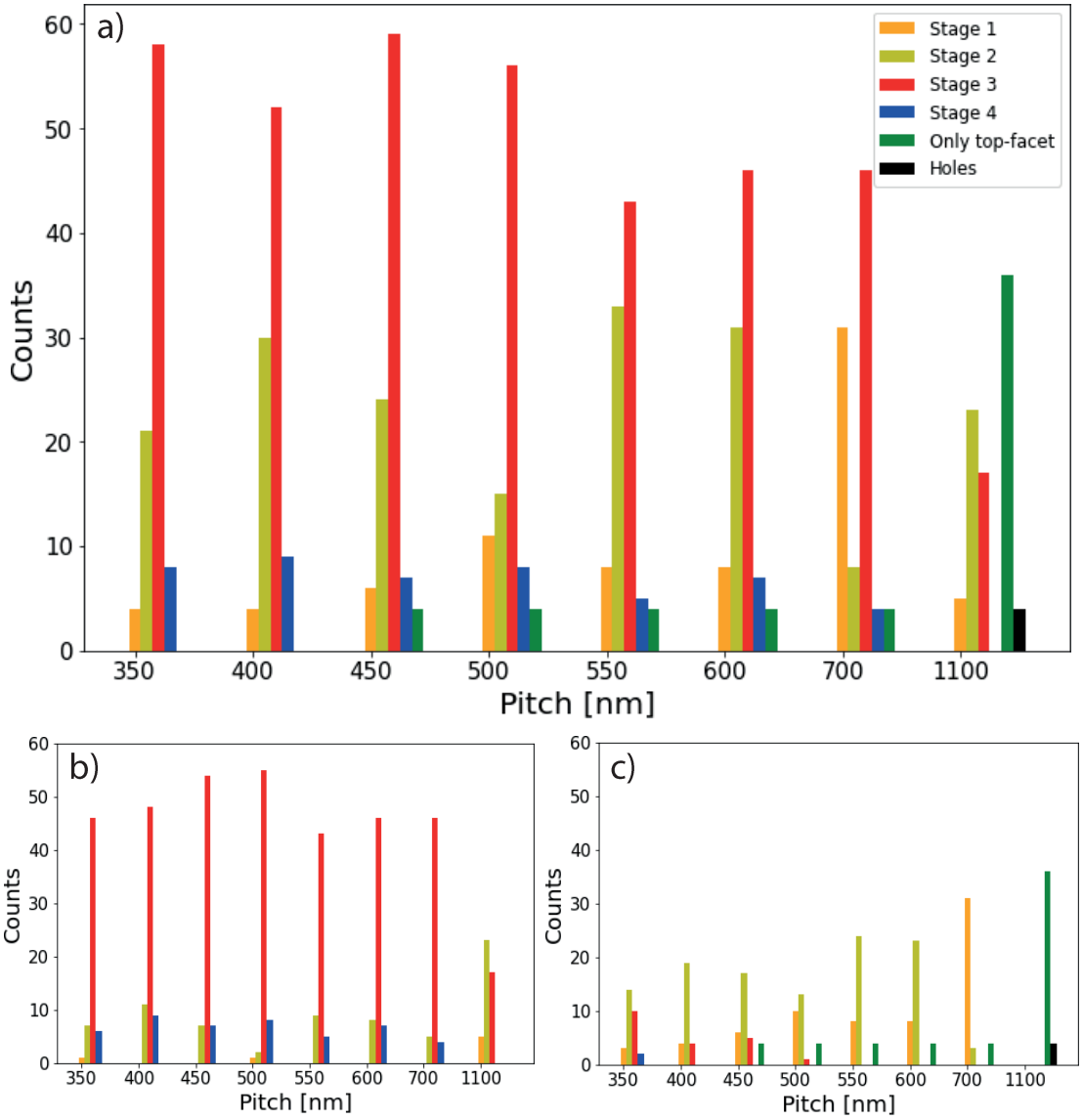

Figure 28: Histograms of growth stages from stage 1 to 4, holes (no growth) and mainly top-facet represented in the array of GaAs buffer dots for 200 nm design diameter dependent on the pitch. a) Shows all the shapes counted in the array for different pitches. b) Is only the middle of the array leaving out the counts of the 4 edges where c) is only representing the counts from the edge. Unclassified shapes are not included in the histograms.

Looking at the SEM images in Figure 26 a) the second thing noted is that the dots at the corners and edges are not grown as much as those in the middle of the array. It is also clear to see that the dots at the edges show a trend of being in earlier growth stages with less volume than the ones in the middle of the array when looking at the colors in Figure 26 b), the edges are dominated by yellow when the middle is dominated by red.

Figure 28 a) shows a histogram of how many different growth stages are represented in an array of GaAs buffer dots of the same width (200 nm design width) and pitches (350 nm - 1100 nm). Figure 28 b) and c) show histograms, from the middle of the array (disregarding the edges) and only the edges (disregarding the center of the array), respectively. It can be noticed from Figure 28 a) that with increasing pitch the dots appear in earlier growth stages. When the pitch reaches 1100 nm growth stage 4 (blue in Figure 28 a)) is not presented in the entire array, and the numbers of dots reaching stage 3 (red in Figure 28 a) and b)) drops significantly compared to the smaller pitches. Furthermore the number of dots which are only evolving the top-facet (green) appear only for the largest pitch. The trend is more clear when only looking at the dots grown at the edge of the array (Figure 28 c)). Looking at Figure 28 c) it is seen that stage 1 (orange) becomes more pronounced when increasing the pitch, this is a trend also seen for the green which presets an early stage 1, the case for the stage with only top-facet. The growth stage 3 (red) disappears for pitches above 550 nm, and growth stage 4 is only seen where the pitch is the smallest at 350 nm. This trend is a result of the sourcing effect where more material is Incorporated in the dots with smaller pitches and more adatoms are leaving the dot arrears to the mask when the pitch is increased. The trend should also be seen clearly in the middle of the array (Figure 28 a)) but here it seems like the growth conditions for the chosen dot size and pitches favored stage 3 (red). By increasing the size of the dots the trend would be shifted so the earlier stages would be seen for smaller pitches. To test this idea, an array of dots of bigger sizes such as 250 nm and 300 nm can be analyzed to see if the trend becomes more obvious. These patterns exist in the current design and can be potentially analyzed in the near future.

4.2.3 Polarity

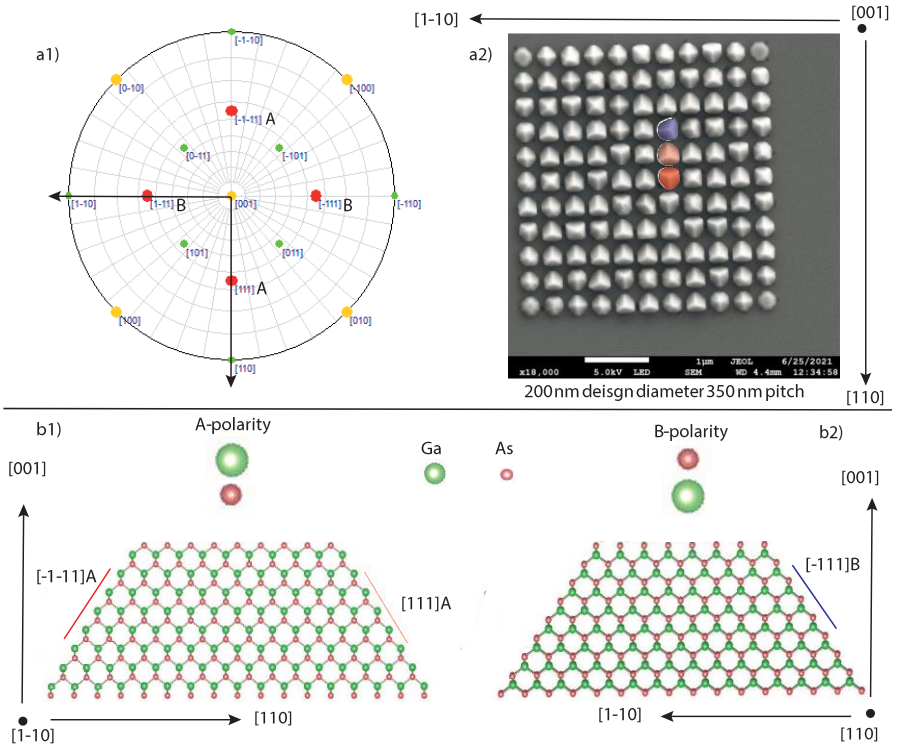

Figure 29: a1) is the stenographic projection orientated with respect to the substrate orientation, with arrows pointing in the [110] and [1-10] direction. a2) SEM image of GaAs buffer dots with 200 nm design diameter and 350 nm pitch, the 3 shapes belonging to 3 different orientations are marked with false colors. Bright red is with the (-1-11) facet and the tip pointing in the [110] direction, dim red is with the (111) facet and the tip pointing in the [-1-10] direction. Blue is with facet (-111) with the tip pointing in [1-10] direction. b1) and b2) is a model made in the software VESTA to show the polarity of the crystal structure. A-polarity is shown when the dumbbell is presented with the III-material (Ga, green) pointing to the surface, B-polarity is presented when the V-material (As, red) is pointing to the surface.

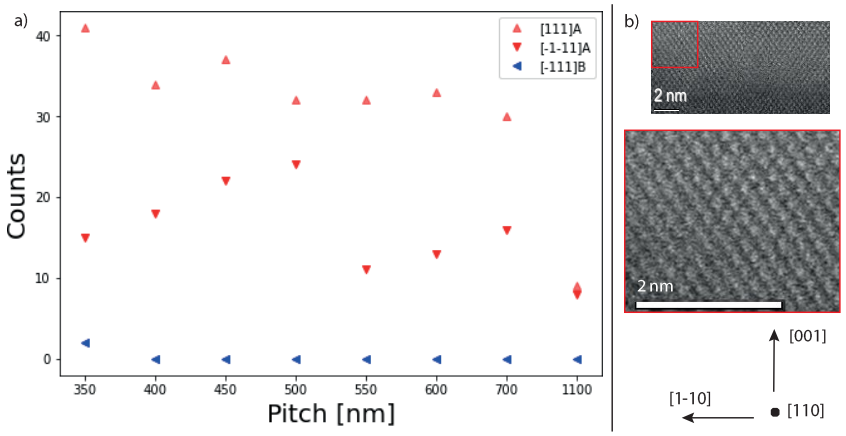

Figure 30: a) is a plot of the counted 3 shapes from the GaAs buffer dots for 200 nm design diameter and pitch ranging from 350 nm to 1100 nm. The dim red arrows pointing up is the shape with the facet [111]A, the bright red arrows pointing down is the shape with [-1-11]A facet and the blue arrows pointing left is has the [-111]B facet. b) is a HR TEM from 150 nm design diameter and 1500 nm pitch.

Figure 29 and 30 how a study of the polarity in 111 facet family for GaAs buffer dots in growth stage 3. Figure 29 a1) is the SP orientated in the same direction as the SEM image in a2) of the buffer dot with design diameter of 200 nm and pitch 350 nm with the zone axis in [001] direction. In Figure 29 a2) the 3 different orientations of growth stage 3 is shown in false colors. The blue has a [-111]B facet with the tip pointing in the [1-10] direction, the dim red has an [111]A facet with the tip pointing in [-1-10] direction and bright red with a [-1-11]A facet with the tip pointing in the [110] direction. The definition of polarity is shown in the VESTA model Figure 29 b1) and b2). b1) Show the buffer dot with zone axis in the [1-10] direction which shows a dumbbell structure consisting of Ga atom (green) on top of the As atom (red). This results in the Ga atom facing outwards from the crystal and indicates A-polarity of the 111 facet family. Rotating the crystal 90 degrees around the [001] direction shows the B-polarity of the 111 facet family, where the dumbbell is flipped and the As atom is facing out [37]. The exact polarity of this growth can only be confirmed with high-resolution tunneling electron microscopy (HR TEM) to see individual atoms. The HR TEM taking for this study has only been done with the zone axis in [110] direction where the dumbbell structure can only be sensed and the polarity can not be distinguished (see Figure 30 b)). Figure 30 a) show the counted

structures within the array of 200 nm design diameter for pitches from 350 nm to 1100 nm. It is seen that the A-polarity (red) is favored above the B-polarity (blue) in this growth. Only two duffer dots with B-polarity are seen in the growth with the smallest pitch of 350 nm and are not seen for larger pitches. There have been distinguished between the two facets [111] and [-1-11] both with A-polarity, even these facets should not differ in surface energies and grow with the same probability it is seen that more [111]A facets are formed then [-1-11]A facets. The reason for this can only be speculated at this level of study and suggestions could be that maybe a small rotation of design on top of the substrate favors one of the facets more than the other or a small tilt occurring in the substrate under the fabrication of these [38].

4.2.4 Height of the GaAs buffer dots

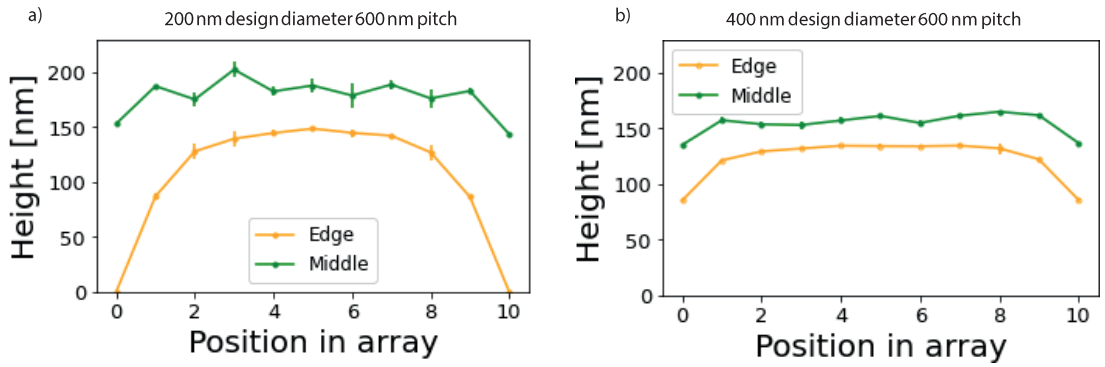

Figure 31: Height as a function of the dot position in an array of GaAs QDs with 600 nm pitch and a) 200 nm diameter and b) 400 nm diameter. The position is from 0 to 10 where the plot for the outer dots at the edge (orange) is an average of all 4 edges and the green line is a plot of the average from 3 lines of dots through the middle of the array. This can also be seen in the Appendix 7.7. The lines are a guide for the eye.

Figure 31 a) and b) show the average height of 200 nm and 400 nm GaAs buffer dots respectively, as a function of the position in the array averaged along all 4 lines for the outer dots and along 3 lines going through the middle of the array for 600 nm pitch (see Appendix 7.7). In Figure 31 a) the first thing seen is that the height of the middle (green) GaAs buffer dots, with an average height of roughly 175 nm, is higher than the GaAs buffer dots at the edge (Orange) of the array with an average height of 140 nm for dots in position 2 - 8. This indicates that the inner dots incorporate more material than the outer ones as expected when considering the results from Espineira et *al.* We

observe that the GaAs buffer dots are sourcing material and the strength of the sourcing effect is bigger for outer dots than for the inner dots because more adatoms are leaving the dots and going to the mask than adatoms incorporating in the dots. It is observed that the corner dots (position 0 and 10 at the edge) do not grow at all whereas the next dot (position 1 and 9) has a height around 80 nm which is the largest increase in height along the position line. The height seems to saturate between position 2 and 8 for the dots at the edge line. The height of position 0 and 10 for the position along the line through the middle of the array is also lower than the height at the position 1 - 9. Figure 31 b) shows the same trend with lower dots at the edges and height dots at the middle of the array. The average height of position 1 to 9 for the dots at the edge is around 125 nm and around 150 nm for the dots at the middle.

Comparing Figure 31 a) and b) it is seen that the height of the dots along the line at the edge (orange) varies more along with the position for 200 nm design diameter than for the dots of 400 nm design diameter. This is again an effect of the sourcing effect where the dots with 200 nm design diameter have a bigger distance between the neighboring dots and therefore more mask around them than the ones with 400 nm design diameter. This effect is stronger the fewer the neighbors which are seen as a bigger jump from dots at corners (position 0 and 10 at the edge, i.e 3 neighbors) to dots at position 1 and 9 respectively which have 5 neighbors, then from position 1 and 10 with 5 neighbors to position 1 and 9 respectively with 8 neighbors for the line going through the middle of the array. It is also seen that the average height for position 2 to 8 in both inner (140 nm) and outer (175 nm) dots of 200 nm design diameter is greater than the average height at the same positions for inner dots (125 nm) and outer (150 nm) for dots of 400 nm design diameter. This means that the smaller the dots the less material needs to be incorporated to reach later growth stages for the dots. This indication can also be seen in the variation of height in the inner dots at 200 nm which comes with the difference in the different shapes occurring at later growth stages.

4.2.5 Nominal incorporation growth rate

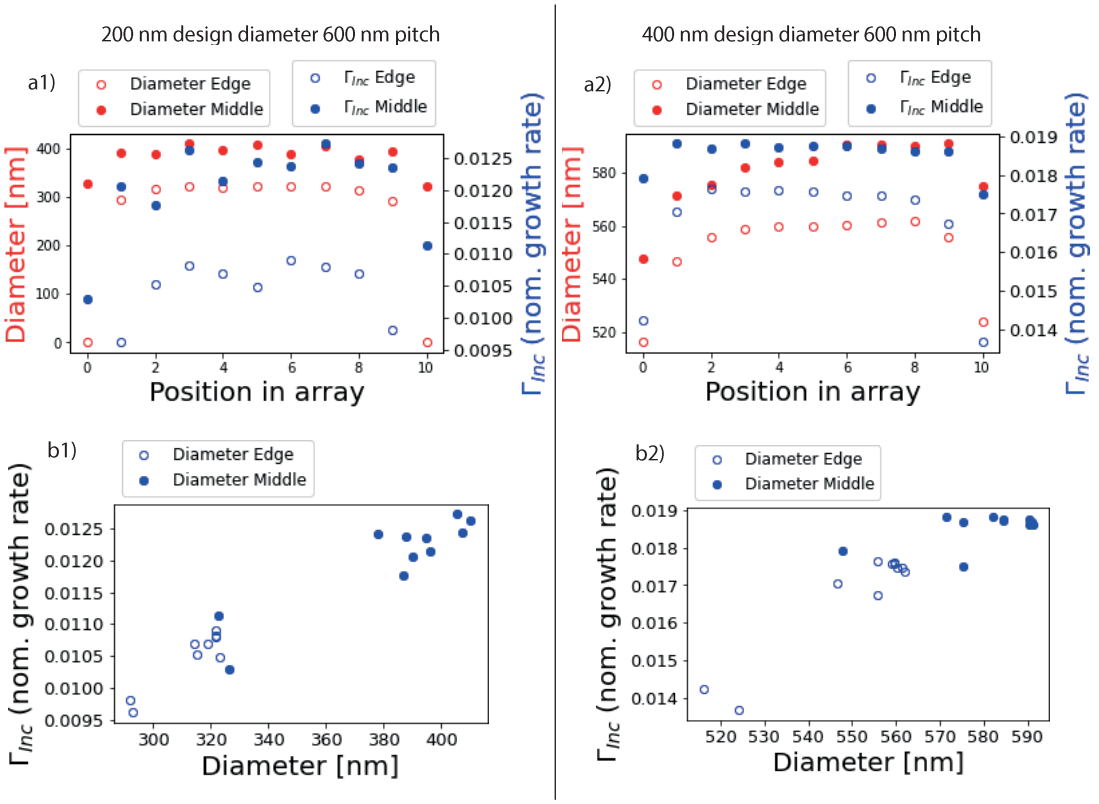

Figure 32: Nominal incorporation rate Γ_{Inc} dependence for 200 nm design diameter and 400 nm design diameter with 600 nm pitch. a1) and a2) show the base diameter of the GaAs buffer dot (red) and the Γ_{Inc} (blue) as a function of the position in the array for dots along the edge line (hollow circles) and dots along the line through the middle of the array (solid circles) for design diameter 200 nm and 400 nm respectively. The base diameter is calculated from the measured base area of the dots assuming the shape is circular. b1) and b2) show the Γ_{Inc} as a function of the base diameter for the dots along the edge (hollow) and dots through the middle of the array (solid) for 200 nm design diameter and 400 nm design diameter respectively.

Figure 32 a1) and a2) show the diameter (red) and nominal growth rate (blue) as a function of position in the array for dots at the edge (hollow circles) of the array and dots in the middle (solid circles) of the array for 200 nm and 400 nm design diameter and 600 nm pitch respectively. The diameter is calculated from the are of the dots under the assumptions of a circular dot. Figure 32 a1) show that the diameter (red) for the

middle dots are larger than the ones at the edge and follow the same trend as the height of the dots where the corners at the edges did not grow and the dots with the same amount of neighbors have roughly the same diameter of 300 nm along the edge. The outer dots with 5 neighbors for the dots along the lines through the middle (solid) are around 325 nm and smaller than the ones with 8 neighbors which has a diameter of roughly 400 nm. The middle dots fluctuates more in diameter than the dots at the edge which again could be due to a greater shape variation in the middle of the array. The nominal incorporation growth rate is plotted in blue as a function of position and shows roughly the same trend as the diameter and height, where the rate increases with more neighbors and more material get incorporated. The nominal incorporation growth rate (Γ_{Inc}) is the growth rate of the dot compared to a 2D film growth ($\Gamma_{\text{Inc}} = 1$) under same growth conditions. The equation is given by:

$$\Gamma_{Inc} = \frac{V}{taA} \tag{11}$$

Where V is the volume of the dot, t is the time growth in seconds, a is the lattice constant and A the base area of the dot. It is seen that the Γ_{Inc} is very low only around 0.0125 for the ones that incorporate the most. This means that these dots only incorporate 1.25 % of what would have been incorporated in the same area for a planar 2D growth. almost all the adatoms go to the mask which means is in an extreme sourcing mode. Figure 32 a2) shows the same kind of data for 400 nm design diameter. The trend here is roughly the same as seen before where the dots with fever neighbors has a smaller diameter. It seems like both the dots along the line through the middle and the edge decrease in diameter for the dots with the highest amount of neighbors, this trend is not expected but should be symmetrical around the middle of the position in the array. For the biggest dots the $\Gamma_{\text{Inc}} = 0.019$ which is an increase from dots with 200 nm design diameter but still very low. The trend of increasing Γ_{Inc} for increasing diameter can also be seen in Figure 32 b1) and b2). b1) show the Γ_{Inc} as a function of the diameter and show a linear decreasing dependence, which means that the bigger the diameter the more amount of material gets incorporated. It is also seen that the ones at the edges hve a lower Γ_{Inc} than the ones at the middle of the array. Increasing the design diameter to 400 nm in Figure 32 b2) show a further increase of Γ_{Inc} with increasing diameter. Here it seems like when the diameter is reaching above 580 nm the Γ_{Inc} saturates, but this trend is not clear.

4.2.6 Top facets of GaAs buffer dots

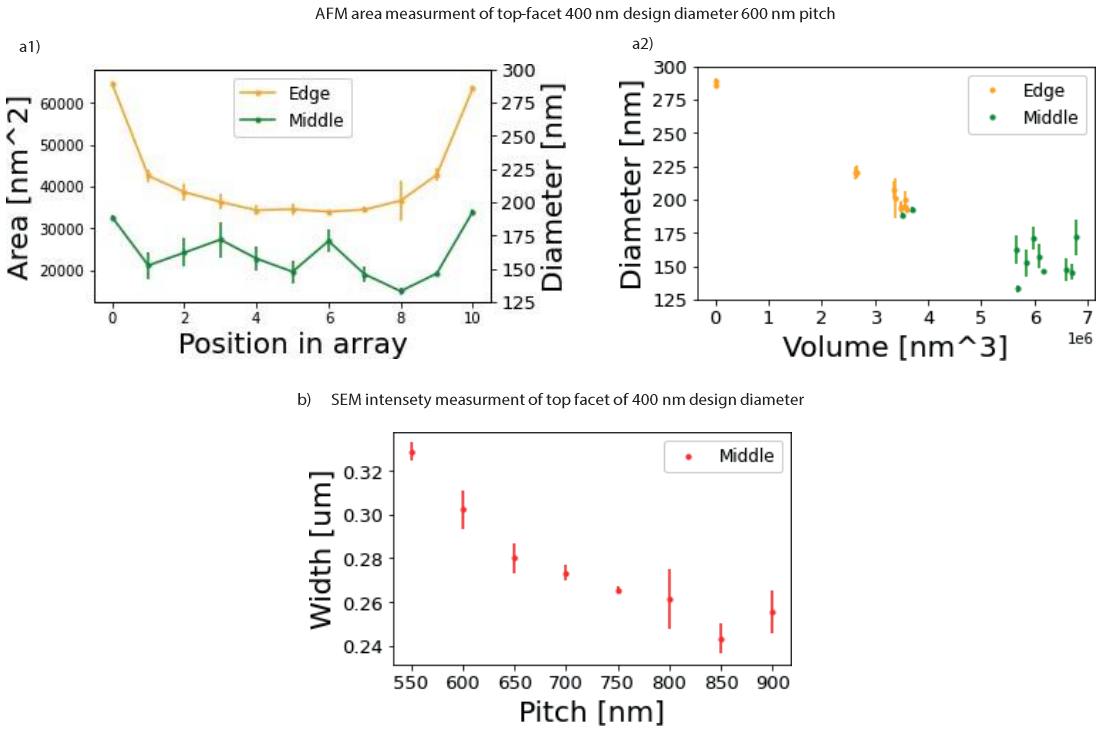

Figure 33: Indication of the evolution of the top-facet for 400 nm design diameter. a1) Shows the area and diameter depending on the position in the array along the edge (orange) and along the middle (green) for 600 nm pitch for AFM images, a2) shows the diameter of the top-facet as a function of volume for the same set of data (see Appendix 7.7 for measurement explanations). b) Shows the width measured from intensity peaks in SEM images dependent on the pitch (see Appendix 7.8 for measurement details). The error of the mean is indicated as error-bars in the data.

Figure 33 a1) shows a plot of the position in the array along a line as a function of the area [nm^2] and the diameter [nm] of the top-facet, for the GaAs buffer dots (400 nm design diameter and 600 nm pitch), the line connecting the points are a line to guide the eye and not a fit. The orange curve is an average measurement of the for edges in the array and the green is an average of 3 lines through the middle (see Appendix 7.7). It is seen that the corners (position 0.) of the edges have a bigger top-facet than the ones in the middle. Due to the corner dots having more mask and only 3 neighbor dots the material incorporate less compared to all the other dots i.e more material is leaving the growth sight due to sourcing. This follows along with the theory from Espineira et

al. [29] The dot in position 1. shows an approximately 25 % decrease in top-facet from position 0. which has 5 neighbor dots and less mask region than dot in position 0. This indicates that the dot is incorporating more material and the effect of the sourcing is not as strong as for the dot in position 0. The strength of the sourcing effect becomes less when going towards the middle position. Positions 4 - 7 seem to source the same and have the same top-facet diameter of approximately 200 nm. Even though the amount of neighbours matters the most in this case, going from 3 to 5 neighbors, it is seen that this is not the only factor that matters because dots in position 1 and 2 do not incorporate the same. This is due to the distance to the mask along the position line being shorter for dot 1 than dot 2. The adatoms which are leaving the dot nr 1 have a higher probability of going to the mask and leaving the system and not incorporating into neighbor dots in this direction than adatoms leaving dot nr 2. It is seen that the dots from the lines going through the middle of the array (green) have a smaller top-facet than the dots along the edges. This is again explained by the strength of the sourcing effect not being that effective because the distance to the mask is getting bigger for the dots at the center. It is also seen that the variation of the top-facet area is getting bigger (from 130 nm to 175 nm) for the inner dots (190 nm to 200 nm) than for the dots at the edges. This can be speculated to be an effect of the different shapes (1-fold and 4-fold) occurring more often within the array than at the edges where mostly one shape (or 4-fold family) is found.

Figure 33 a2) shows the top-facet diameter as a function of the volume for the AFM data set of dots along the edge line (orange) and through the middle line (green). It is seen that the diameter of the top-facet decreases with increasing volume as expected. Following the physics of the sourcing effect and extending the data analysis of how the top-facet evolves dependent on the pitch, one would expect to see an increase in top-facet area with increasing pitch. When increasing the pitch the mask region where the adatoms can go to and leave the system gets bigger and the strength of the sourcing effect increase which will result in less material Incorporated in the dots and thereby an earlier growth stage with a bigger top-facet. Therefore a measurement of the width of the top-facets were done for pitches from 550 nm to 900 nm for GaAs buffer dot design diameter of 400 nm. Figure 33 b) shows a plot of top-facet width [um] dependent on the pitch [nm], the width is extracted from intensity peaks from SEM images using Gwyddion (see Appendix 7.8, these SEM images were taken by Damon Carrad using ELine). This trend shows the opposite of what was expected. The width of the top-facet decreases with increasing pitch. This trend most likely indicates that the openings for the GaAs growth were bigger for smaller pitches than for larger pitches causing the dots for smaller

pitches to be bigger compared to the ones for larger pitches. All dots were expected to have the same size but due to the proximity effect at the EBL process in the fabrication this could cause the effect observed.

4.3 Transmission electron microscopy

Tunneling electron microscopy (TEM) images were taken on the GaAs/InAs quantum dots to have a better understanding of the growth of InAs layer on top of GaAs. The TEM images were taken by Sara Martí-Sánchez on a TITAN TEM microscope located in Zaragoza. TEM makes it possible to see the InAs/GaAs interface and do analyzes of the atoms arraignment in the two materials. To perform the analysis, the sample are first milled down to a very thin lamella of approximately 50 nm wide and 3 um - 5 um long. Such lamella is transparent for the electron beam and thus can be readily analyzed with TEM. The lamella cut was done at the cross-section in the middle of the array of dots (see Figure 34 e)). The lamella cut is expected to have no more than 2° tilt therefore it is assumed that the cut goes through the middle for all dots. TEM was taken for dots with GaAs buffer design size 150 nm diameter with 1500 nm pitch (Figure 34) and 200 nm diameter with 2000 nm pitch (Figure 35). In the zoom-in (Figure 34 b) and Figure 35 b)) the SiOx mask is seen in black, GaAs in gray and InAs as lighter gray The sample is protected with an oxide layer In Figure 34 a) a TEM image of 5 dots of size 150 nm design diameter width 1500 nm pitch is shown. It is assumed that if the image showed all the dots (11 dots) the image would have mirror symmetry. Figure 34 b) shows a zoom-in of the 5 dots. The dot #5 shows no growth of GaAs buffer over the SiOx surface due to the sourcing effect (see section 4.2) and it is seen that some of the GaAs substrate have been disorbed doing the MBE growth (see section 4.1). The measured height and width of the dots are given in the Table 5. The measurement were done at the images showing the dialitation due to better contrast using the software ImageJ.

# dot for 200 nm	Height [nm]	Width [nm]
#3a	23.9	65.8
#3b	16.0	37.3
#2	36.3	81.0
#1	29.1	81.3
# dot for 150 nm	Height [nm]	Width [nm]
#4	30.3	63.2
#3	28.3	87.4
#2	29.6	88.2
#1	32.0	91.3

Table 5: Measured height and width of InAs QDs from TEM images (D_{xy})

Figure 34 c) shows a set of high resolution (HR) TEM images at the interface for dots #1 to #4 and the corresponding Geometric Phase Analysis (GPA) maps. TEM has atomic resolution which makes investigation of the atoms location in the crystal possible. With GPA the displacement fields of the atoms in the material are accessed. The analysis of the dilatation in xy-plane (D_{xy}), i.e the displacement of the atoms in the field of view, shows that there is approximately 7 % displacement of the atoms position in the InAs (yellow) compared to the reference (blue, GaAs). This indicates the 7.2 % mismatch between the lattice parameters of InAs and GaAs. The change in color from blue (GaAs) to yellow (InAs) occurs abruptly at the interface. This means that the InAs is plastically relaxed on top of the GaAs. This can only be done by introducing an array of misfit dislocations at the InAs/GaAs interface, which is seen as color discontinuity at the interface. The dislocations can be seen more clearly in the GPA of the rotation in xy-plane. Here the reference GaAs color is between red and green, which corresponds to 0° rotation in the lattice. At the interface of 4 the dislocations are seen clearly as rotations at -5 and +5 (blue and white spots) periodically placed along the x-direction. The distance between the dislocation is measured to be ≈ 10 nm for 150 nm design diameter and ≈ 8.6 nm for 200 nm design diameter. The measured distances are an average of the distances of dislocations in dot #4, #3 and #2 for 150 nm and dot #3b and #2 for 200 nm. The theoretically calculated distance for a fully relaxed InAs QD is 8.35 nm which could indicate that the InAs grew in this project still have some strain. In Figure 35 c) it is seen for dot #3a, #3b and #2 that the edge of the InAs dot is green/blue in the right part of the dot and yellow/red in the left part, this means that the right part has minus rotation where the left part has plus rotation which indicate that the lattice planes are bent down on the sides of the InAs QDs corresponding to some elastic relaxation. Figure 35 c) dot # 2 show the same green color at the edges which indicate rotation in the same direction.

Figure 34 d) and Figure 35 d) show data from Electron Energy Loss Spectroscopy (EELS) which shows the relative element composition as percentage on a color scale. The top picture shows that there is 100% In in the QD and 0% in the buffer GaAs dot relative to Ga. This indicates no element segregation i.e no mixing of In into the GaAs or Ga into the InAs QD. A sharp interface between InAs and GaAs is also seen.

In Figure 35 b) the InAs QDs seem to grow on the edges of the GaAs dot, this is also seen for 150 nm dot #4, one could speculate the growth of InAs starts on the edges before merging in the middle. The GPA in Figure 35 c) shows the same trend as GPA for 150 nm where InAs seems to be almost fully relaxed looking at the dilatation and

have elastic rotation. It is observed that dot #2 in the 200 nm (Figure 35 c)) and, less clear dot, #2 in 150 nm (Figure 34 c)), seems to also have InAs grow on the side facet of the GaAs buffer dot. In general, the dots seem to grow primarily on the top-facet of GaAs buffer dots, which was one of the goals for this project.

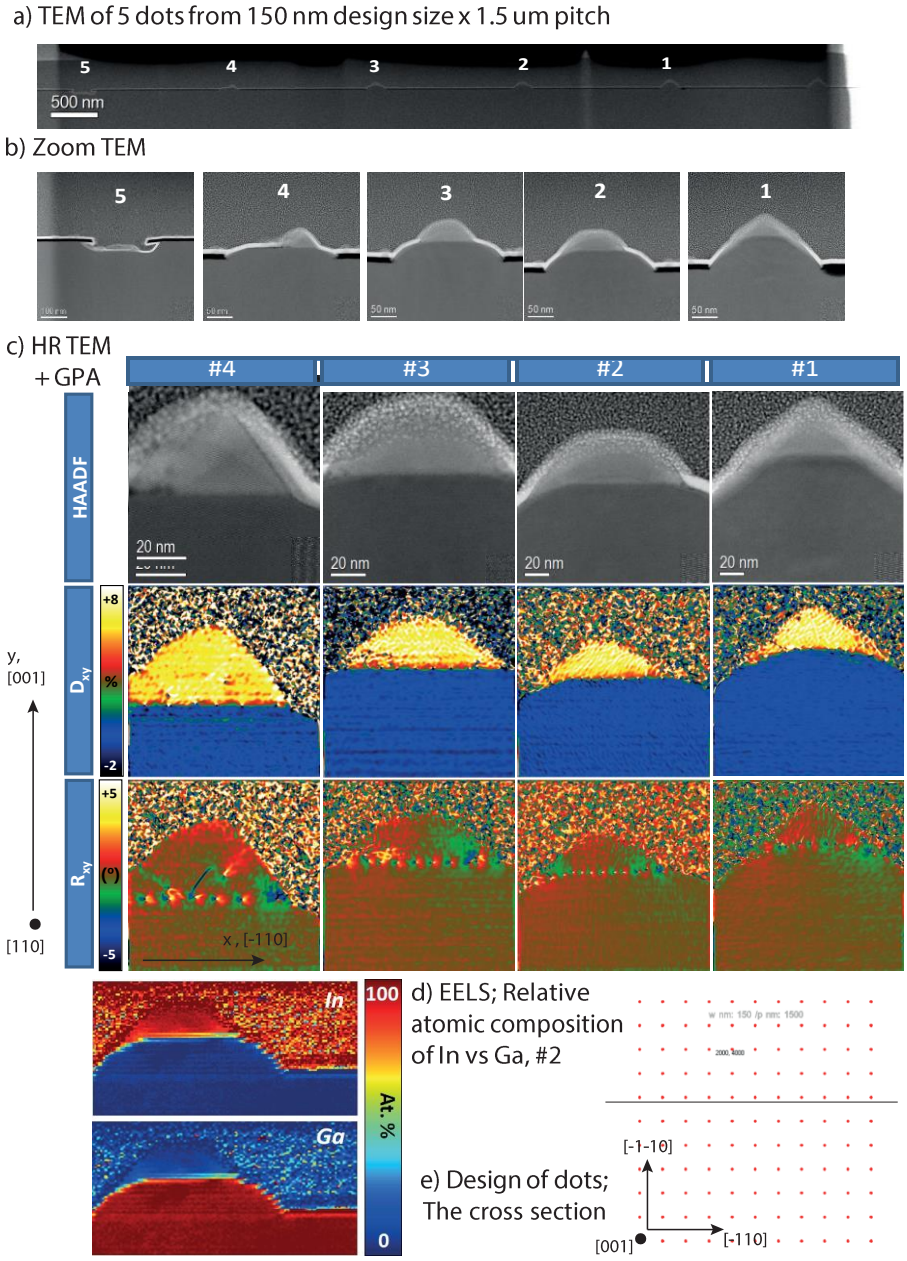

Figure 34: This figure shows data from TEM analysis, on dots with 150 nm design trenches and 1.5 μm pitch. The detector used for the TEM images is a High Angular Annular Dark Field (HAADF) detector. a) shows a TEM image of 5 dots in the array. b) is a zoom-in. c) is Geometric Phase Analysis (GPA) of 4 of the dots, showing the dilatation (D_{xy}) and rotation (R_{xy}) in the lattice as a color plot. d) shows the Electron Energy Loss Spectroscopy (EELS) for the In and Ga composition. e) shows the design of one array and indicates where the cut section is taken.

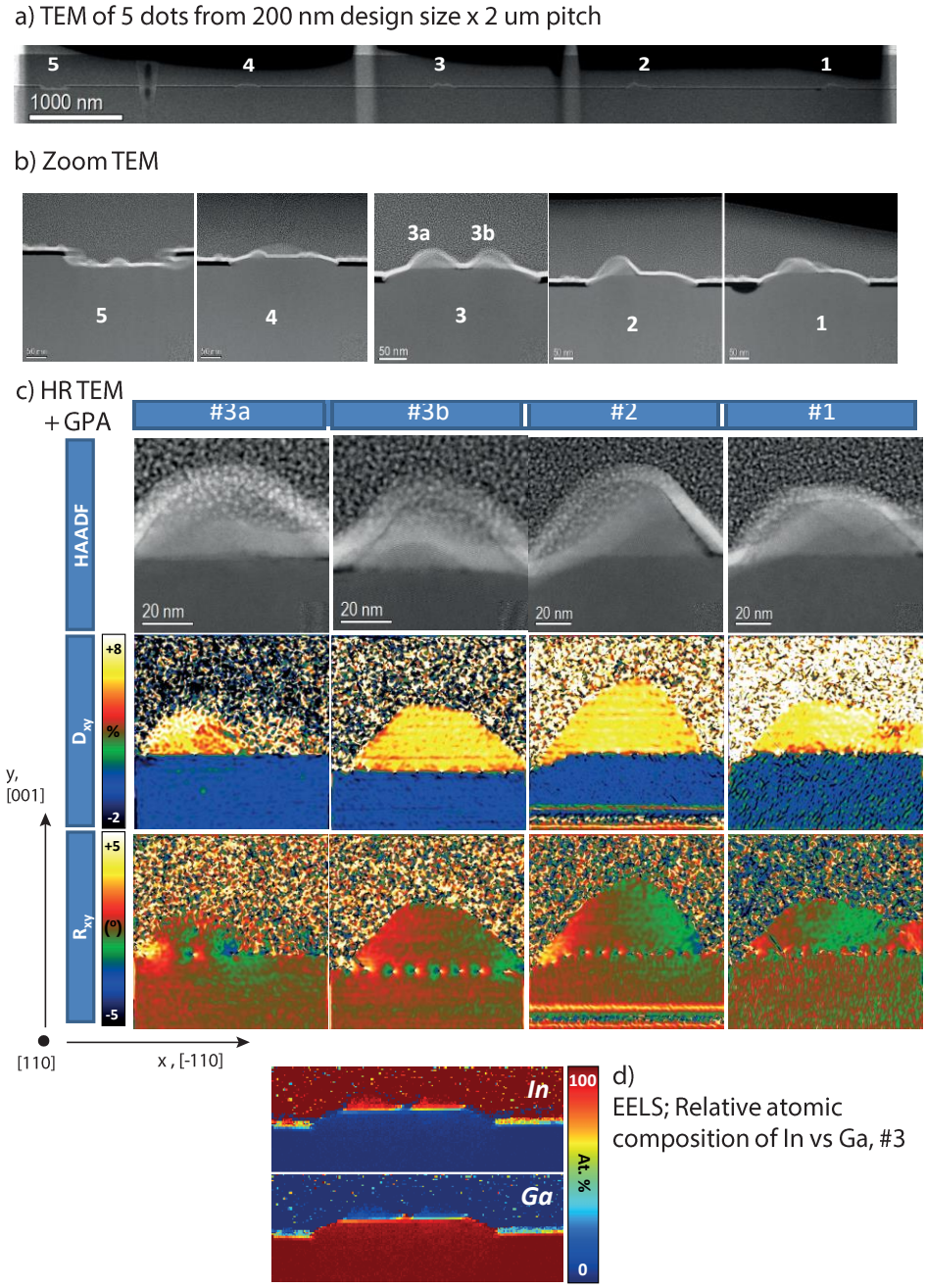

Figure 35: This figure shows data from TEM analysis, on dots with 200 nm design trenches and 2 μm pitch. The detector used for the TEM images is a High Angular Annular Dark Field (HAADF) detector. a) shows a TEM image of 5 dots in the array. b) is a zoom-in. c) is Geometric Phase Analysis (GPA) of 4 of the dots, showing the dilatation (D_{xy}) and rotation (R_{xy}) in the lattice as a color plot. d) shows the Electron Energy Loss Spectroscopy (EELS) for the In and Ga composition.

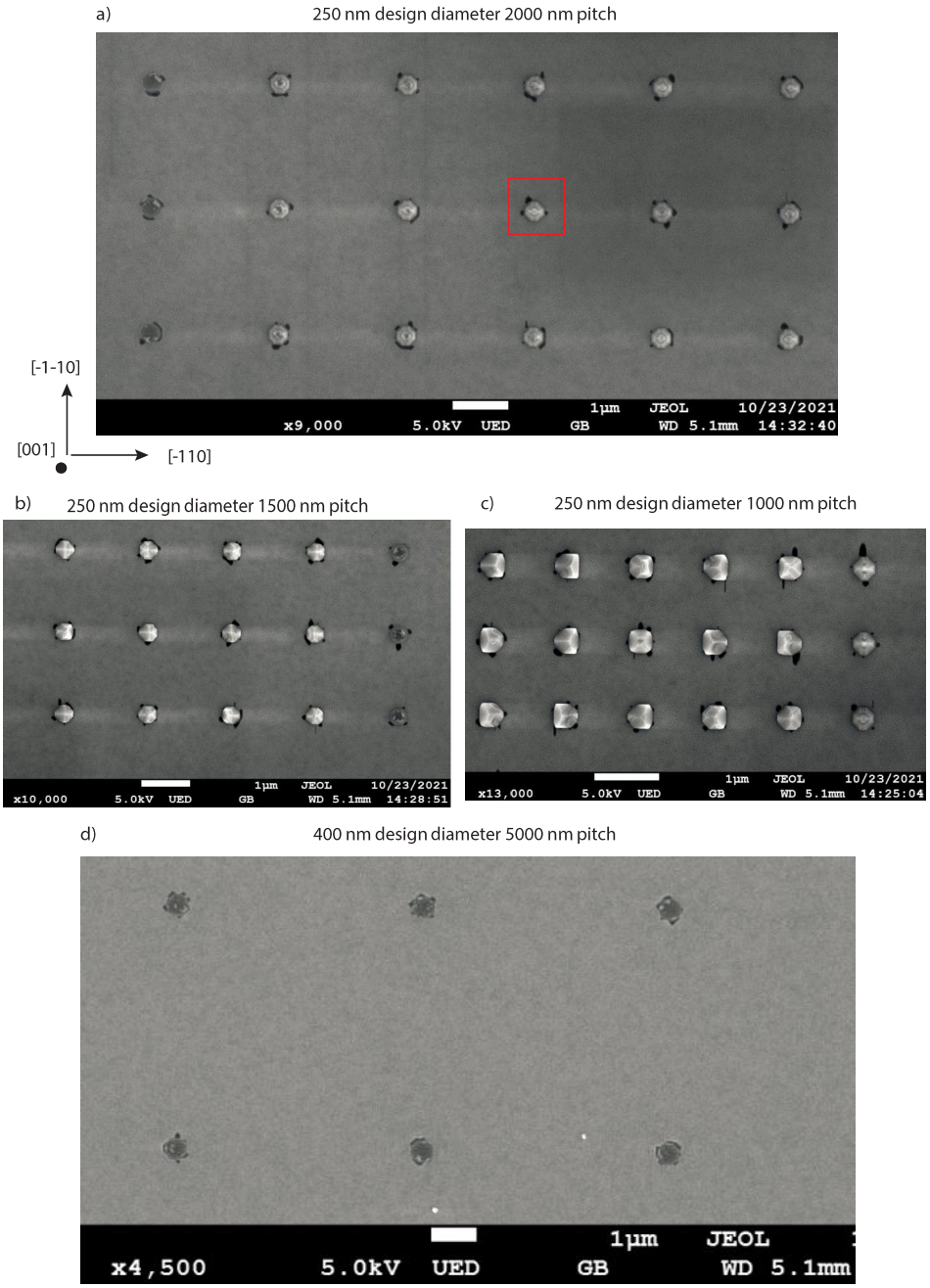

Figure 36: SEM images of GaAs buffer dots with InAs QDs (Smaple QD1132). a), b) and c) is SEM images at the edge in the middle of the array of dots 250 nm design diameter with 2000 nm, 1500 nm and 1000 nm pitch respectively. c) is a SEM image at the middle of the array of dots 400 nm design diameter with 5000 nm pitch.

Figure 36 show SEM images of sample QD1132 with InAs growth on top of the GaAs buffer dots a) is an image taken at the middle of the left edge of the array for 250 nm design diameter and 2000 nm pitch. It is seen that the InAs is grown mainly on the top-facet of GaAs buffer dots but the InAs is in general not uniformly grown which is a consequence of the GaAs/InAs lattice mismatch. It is seen that in some case the InAs starts nucleation at the edge of the GaAs top-facet and even form a ring which also would show op as two separated dots in the TEM even though they were not. One more uniformly shaped InAs QD with a width of 124 nm is seen in a) second row fourth column. Looking at Figure 36 b) the pitch is decreased to 1500 nm and the InAs starts to grow on the side facets as flakes due to no available GaAs top-facet. This is also seen in c) where the pitch is decreased to 1000 nm but nicely faceted InAs QDs are formed at the top-facet of the GaAs buffer dots at the edge. Figure 36 a), b) and d) show that even though the GaAs buffer dot is not formed InAs will grow in the trenches. This is a result of the sinking effect, which is the opposite of the sourcing effect, where the flux of adatoms coming from the mask is greater than the adatoms leaving the growth openings. This is also seen in the TEM (Figure 34 b) dot 5) where no GaAs buffer is grown but InAs is represented in the trench.

4.4 Photo luminescence

When observing the QDs in the ThorLab camera we had to make sure that we were looking at the luminescence from the QDs. Firstly the dots were only seen when the excitation laser was right on top of the QDs the QDs were not seen in the camera when we moved the QDs away from the beam-spot. Then we had to make sure that the appearance of the dots in the camera was not coursed by reflection or diffraction of the surface structure of the dots, this was tested by adding an optical density filter (OD3) filter at the input to attenuate the excitation laser and decrease its power.

Looking at Figure 37 data from the spectrometer is shown. Figure 37 a) shows the spectra when the laser beam is right above the QDs and unfortunately also array from the QDs, without the OD3 filter. The spectrometer detects the wavelength of the laser and GaAs and some background light. The insert shows the appearance of the QD when the excitation laser is on top and the disappearance of the QD when moved away. When inserting the OD3 filter (Figure 37 b)) the laser is the only wavelength observed in the spectrometer and looking at the camera the QD were gone (insert in Figure 37 b)). This indicates that the appearance of the QD is the luminescence from the QD and not reflection or diffraction from the laser on the surface of the structure. If the QDs were seen using the OD3 filter it would have been a sign of reflection or diffraction of the dots because the OD3 filter is expected to only dim the reflection or diffraction from the excitation laser and not fully remove it.

Unfortunately, Figure 37 a) also shows the spectra when the beam spot is moved away from the QDs, as mentioned, No change in the spectra is seen which indicates that the luminescence from the QDs is not detected in the spectrometer. An indication of peaks at wavelengths 1180 nm was observed but these as well stayed unchanged when moving away from the dots. That the QD luminescence is not detected by the spectrometer is most likely caused by its limitations, the Si-CCD in the spectrometer only have a very low efficiency or none above 1000 nm (see Appendix 7.4) where we expect or luminescence from or QDs. In the insert of Figure 37 a) and Figure 38 it is seen that the QDs luminescence is observed in the ThorLab camera as mentioned, the CCD is also here of a low intensity above 1000 nm (see appendix 7.4) but the difference form the camera and the spectrometer is, that the camera is a direct light imagining tool and collects all the luminescence without any filters, where the spectrometer also includes a grating which consists of slits of different widths to divide the incoming wavelengths. This grating is therefore also wavelength dependent and may be more efficient for specific wavelengths. In addition, more optical components are used to couple the emission into

the spectrometer which leads to more loss (see section 3). This could certainly be the reason why we observe the QDs in the camera and not the spectrometer.

Figure 38 show SEM and camera images with the luminescence and the white light source and only the luminescence without the white light source for different sizes of DQs and pitches. It is observed that the luminescence of the dots seen in the camera disappeared for high pitch and smaller buffer dot size. The intensity can unfortunately not be compared because the power of the laser is unknown and unstable which causes a fluctuation in intensity while taking the images.

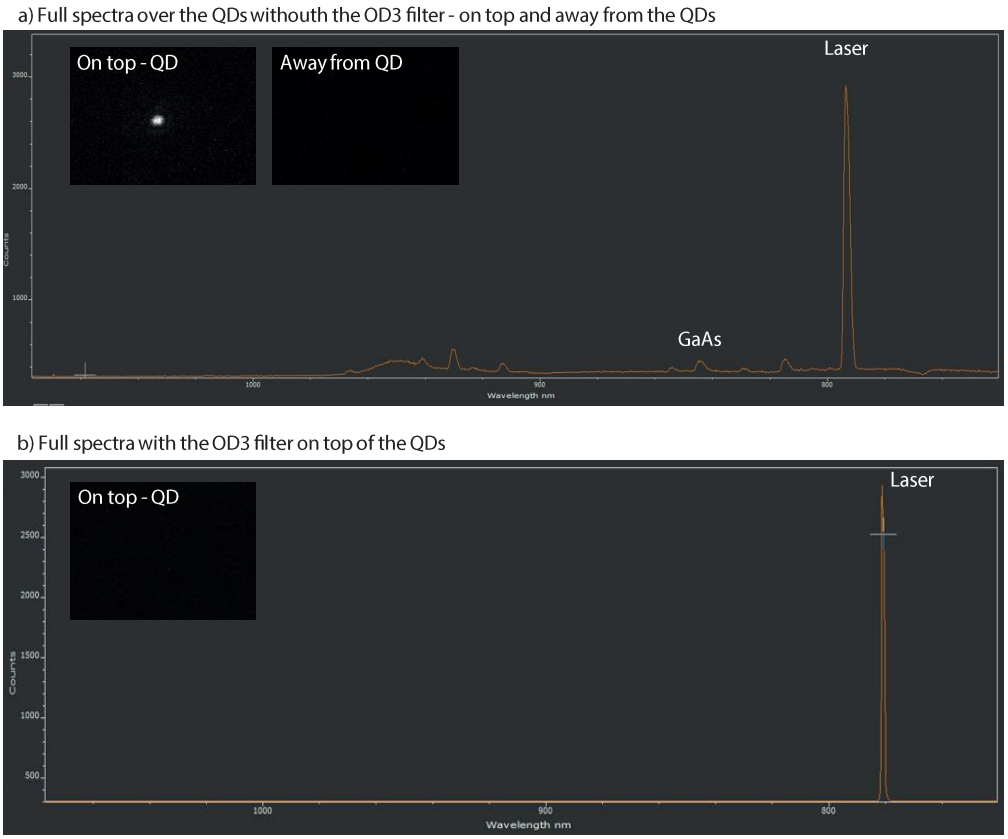

Figure 37: Spectrometer data showing the wavelength on the x-axis and the intensity on the y-axis. a) Is the full spectra from 740 nm to 1200 nm when the beam spot is above the QD array and also when it is away from the array. The insert shows a camera image on top of the QD array and away from the QD array. The wavelength of the laser and estimated wavelength of the GaAs is indicated in the plot, the other peaks are not defined. The spectra are without the optical density filter (OD3). b) Show the spectra with the OD3 with the beam spot on the QD array, where no wavelengths, except the laser, are detected. The insert indicates no luminescence from the QDs in the camera.

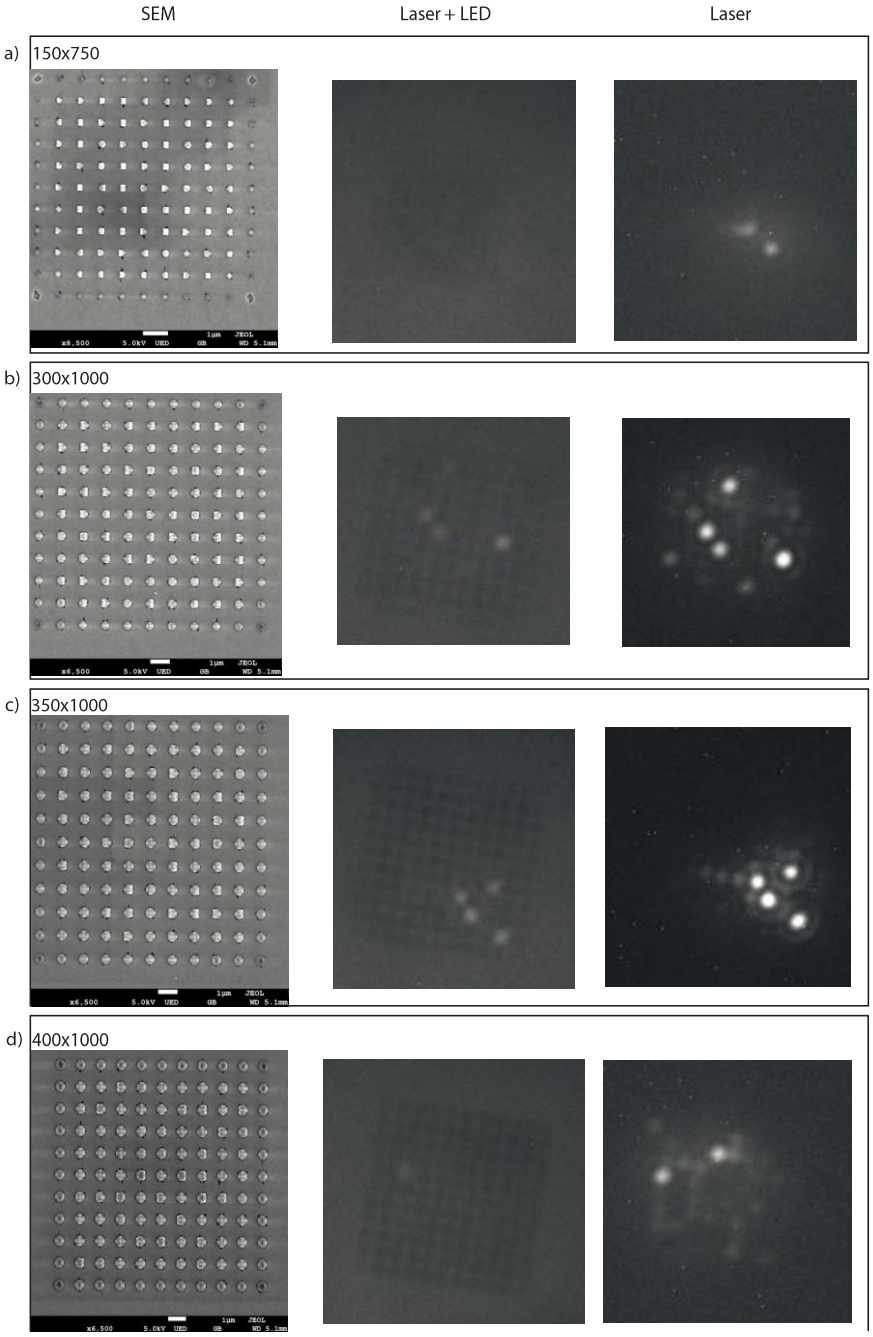

Figure 38: Shows SEM (QD1132), image from ThorLab camera with white light source and luminescence from the QDs (QD1142) when the laser is on and an image of the luminescence without the white light. a) Is for GaAs buffer dot structures of 150 nm size (design) and 750 nm pitch. b) Is for GaAs buffer dot structures of 300 nm size (design) and 1000 nm pitch. c) Is for GaAs buffer dot structures of 350 nm size (design) and 1000 nm pitch. d) Is for GaAs buffer dot structures of 400 nm size (design) and 1000 nm pitch.

5 Discussion

The SK dots, which is the aim to grow selectively for this project, is of a height below 7 nm and with below 40 nm, they are highly strained and with a wavelength around 930 nm. In this study the TEM images of the GaAs/InAs interface showed a highly relaxed InAs dot on the GaAs buffer layer which means that the InAs is not strained as the SK dots. The InAs QDs formed on the top-facet of the GaAs buffer dots are also measured to have a minimum diameter of roughly 70 nm and height of roughly 30 nm for this study (see section 4.3). Knowing that the size of the QD and the strain is defining the confinement of the quantum well in the QD and shortening the wavelength it is expected that the QDs for this study has a much longer wavelength than the SK dots and are getting closer to being bulk InAs (λ = 3000 nm).

Reasons why the wavelength is shorter and the luminescence is seen for big buffer dots and small pitch and not smaller dots and bigger pith could be many. But what is seen at the SEM images(section 4.4 Figure 38) is that QDs that emit is the ones with InAs grown as flakes on the sides (dots with smaller pitch) of the GaAs buffer dots and not the ones which only forms on the top-facet (bigger pitch). On the other hand, no luminescence is seen fro for example 150 nm design diameter and 750 nm pitch even though flakes are seen at the side facets (see Figure 39 d)).

Maybe strain could be introduced in the InAs growth on the side facets which could cause the wavelength of these dots to be shorter and thereby detected by the camera, but TEM needs to be done to confirm this.

Assuming that the InAs QDs, which are formed on the top-facets, emit with a longer wavelength when the InAs QD flakes are the reason why the emission in the camera is not seen, makes it a question of the limitations of the camera which is not efficient for wavelengths above 1100 nm. The limitations of the equipment in general (camera and spectrometer) should be solved by using an InAs-CCD to detect these wavelengths. It could also be a question of the power of the laser and the loss of the emission along the optical path which makes it harder to see the emission from the smaller InAs QD flakes.

The future steps for the growth of SAG InAs QDs would be to adjust the design to have smaller increments in the pitch and size, and increase the amount of QDs in an array to get more statistics. The array could also be considered to be of staggering lines of dots so the distance between all neighbors remains the same in all directions. Then the growth parameters also need to be adjusted both for the GaAs buffer dots and for the InAs

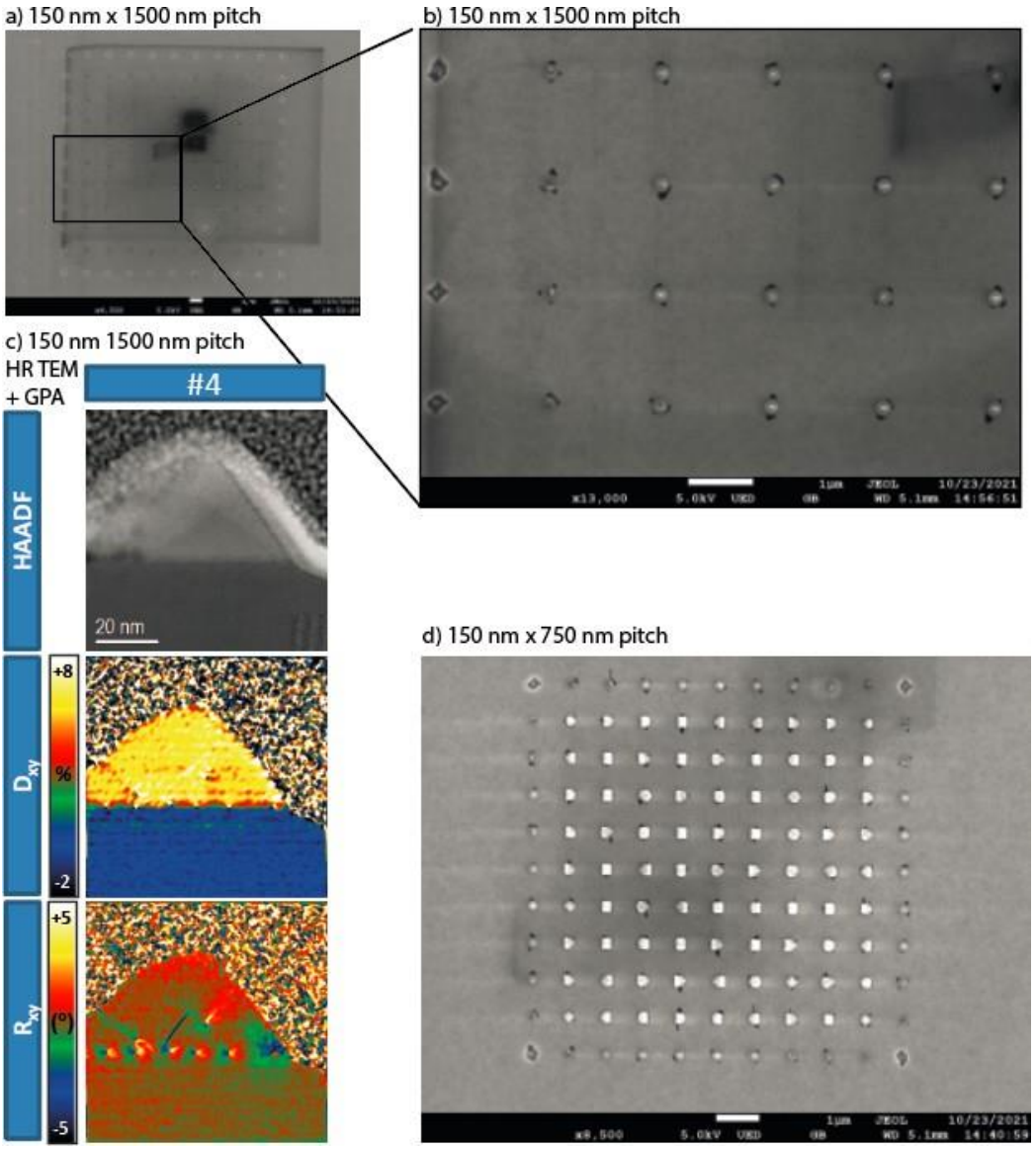

Figure 39: SEM and TEM from 150 nm design diameter. a) is SEM image of 1500 nm pitch where b) is a SEM zoom in of 1500 nm pitch. c) show the HR TEM and GPA for 1500 nm pitch which is discussed in section 4.3. d) is a SEM of 750 nm pitch.

QDs. Either more material for the GaAs buffer dots at larger sizes to grow smaller top-facets, or less material to target smaller sizes so they will form top-facets. The amount of material for InAs seems to be too much even though the parameter settings predict a film of 2.5 nm for regular planar growth. A lot of growths seem to be necessary for testing the growth parameters to target the formation of single SK dots on GaAs top facets. Furthermore the lithography and etching step has to be optimized by investigating the proximity effect and reducing the size distribution doing both lithography, development and etching to get a more uniform array of dots. The etching step could be changed to an anisotropic etching technique by using dry etch or another etchant to make this step more reliable. It is seen that the shape of the opening gets less clear when the size of the opening decreases, therefore a larger opening could result in more uniform dots in the same array and maybe would be the ones to prefer optimizing. It could also be considered to investigate other shapes of the opening which are more strict like a square opening, to maybe get the facet formation of the GaAs buffer more uniform form for more structures.

At some point in the optimization of the SAG-grown QDs the SiOx mask needs to be removed before implementing the QDs in photonic circuits as wave-guides. Therefore it could also have a great value to consider other techniques for creating the mask for the growth sights that are more easily removed.

6 Conclusion

In this study, the fabrication of the mask for SAG GaAs/InAs QDs was performed using EBL and HF wet etching technique. The fabrication steps were found to have a major influence on the mask opening shape and distribution of size within one array was found. The EBL and development step is found to increase the size of the openings by 21 %. The shape seems to be fairly controllable down to 200 nm design diameter for this specific study with the EBL settings and development time chosen. The distribution in size in on array was found to vary from 1.3 % to 1.5 % from the mean value. These parameters should be optimized to bring the size distribution of the openings down to be able to control the facet formation of the GaAs buffer dot structure and thereby the uniformity of the dots and the size of the top-facet within an array for smaller structures than 200 nm.

The shapes within an array for GaAs buffer dots have been categorized into 4 different shapes belonging to 4 different growth stages. Stage 1 of a 4-fold symmetry with the {110} and {111} facet family, stage 2 with 4-fold symmetry of facet family {110}, stage 3 a 1-fold symmetry with facet family {110} and {111} and stage 4, 4-fold symmetry, with facet family {111}. A count of these shapes appearance in an array of 200 nm design diameter for pitches from 350 nm to 1100 nm has been done. From these results, it can be concluded that increasing the pitch shapes in earlier growth stages are forming. The evolution of shapes can be seen clearly at the edge of the array can be seen going from pitch 1100 nm where no facets but the top-facet are forming to decreasing pitches where shapes at later growth stages are seen. At pitch 500 nm growth stage 3 starts to show and at 350 nm growth stage 4 is appearing at the edge. Where growth stage 1 is decreasing with decreasing pitch. This trend is an indication of source growth mode. The evolution is not that clear when looking at the inner dots and it is observed that growth stage 3 is the favorable one for the size 200 nm design diameter chosen for this study. To see this trend more clear the same study can be done for bigger structures such as 250 nm or 300 nm design diameter. It has been observed that the polarity of shapes in growth stage 3 favors A-polarity rather than B-polarity and that [111]A appear more than [-1-11]A, the reason for this selectivity has not been found.

The Sourcing effect has also been observed studying the height and diameter of the GaAs buffer dot structures along the edge and through the middle of the array, where the dots is significantly smaller and has Incorporated less material into the crystal at the edge with fewer neighbors and more mask than the dots in the middle of the array. The nominal growth rate has been found to be of maximum 0.013 for 200 nm design

diameter and 600 nm pitch and of maximum 0.019 for 400 nm design diameter and 600 nm pitch. Calculating the nominal growth rate to be less than 1 means that the growth is in sourcing mode and more material is leaving the openings the incorporating. The nominal growth rate is also found to be increasing with increasing diameter.

The top-facet area was one of the targets for this project to minimize. For this study only arrays with 400 nm design diameter were found all to have top-facets, therefore these were chosen to investigate the evolution of top-facets dependent on position in array and pitch. The top-facet is found to be bigger at positions at the edges than dots in the middle of the array and decreasing with increasing volume of the dot which follows the physics of sourcing growth mode. The top-facet is measured to be 130 nm in diameter for the smallest top-facet for 400 nm design diameter and 600 nm pitch, but could be found to be smaller for smaller design diameters and bigger pitches. The minimization of the top-facets should be done in the future by changing the growth parameters to favor smaller design diameters. Expectantly the width of the top-facet was found to decrease with increasing pitch which could most likely be a result of the EBL proximity effect but need to be studied further.

On top of the GaAs buffer dot InAs QDs were grown, to investigate the GaAs/InAs interface and the InAs QD TEM studies were done for 200 nm design diameter with 2000 nm pitch and 150 nm design diameter with 1500 nm pitch. The InAs dots were found to have a size of roughly 70 nm in diameter and be 30 nm in height. Which is huge compared to the target SK dots of 10 nm - 40 nm in diameter and 5 nm - 7 nm in height. The InAs was found to be highly relaxed on top of the GaAs buffer dots with a measured distance between dislocation of 10 nm for dots of 150 nm design diameter and 8.6 nm for 200 nm design diameter. For a fully relaxed InAs crystal the distance is 8.35 nm.

Another goal for this project was to measure the wavelength of the InAs QDs with a spectrometer. This did not succeed due to equipment limitations for longer wavelengths of above 1100 nm. However, photo luminescence was observed in the ThorLab camera for some of the dots in the arrays with big design diameter and small pitch.

References

[1] J. A. Jones, M. Mosca, and R. H. Hansen. Implementation of a quantum search algorithm on a quantum computer. *Nature*, 1998. ISSN 00280836. doi: 10.1038/30687.

[2] David P. DiVincenzo. Real and realistic quantum computers. *Nature*, 1998. ISSN 00280836. doi: 10.1038/30094.

[3] M. T. Deng, S. Vaitiekenas, E. B. Hansen, J. Danon, M. Leijnse, K. Flensberg, J. Nygård, P. Krogstrup, and C. M. Marcus. Majorana bound state in a coupled quantum-dot hybrid-nanowire system. *Science*, 2016. ISSN 10959203. doi: 10.1126/science.aaf3961.

[4] Stephan Plugge, Asbjørn Rasmussen, Reinhold Egger, and Karsten Flensberg. Majorana box qubits. *New Journal of Physics*, 2017. ISSN 13672630. doi: 10.1088/1367-2630/aa54e1.

[5] Peter Lodahl. Quantum-dot based photonic quantum networks. *Quantum Science and Technology*, 2018. ISSN 20589565. doi: 10.1088/2058-9565/aa91bb.

[6] Nicholas Andrew. Wasley. *Nano-photonics in III-V Semiconductors for Integrated Quantum Optical Circuits*. Springer Theses, Recognizing Outstanding Ph.D. Research. Springer International Publishing, Cham, 1st ed. 2014. edition, 2014. ISBN 3-319-01514-1. doi: 10.1007/978-3-319-01514-9.

[7] Gary W. Wicks. III-V semiconductor materials. In *The Handbook of Photonics, Second Edition*. 2006. ISBN 9781420004694. doi: 10.1201/9781420004694.ch2.

[8] H H Yao, T C Lu, G S Huang, C Y Chen, W D Liang, H C Kuo, and S C Wang. InGaN self-assembled quantum dots grown by metal–organic chemical vapour deposition with growth interruption. *Nanotechnology*, 17(6):1713–1716, 2006. ISSN 0957-4484. doi: 10.1088/0957-4484/17/6/028.

[9] John R. Arthur. Molecular beam epitaxy. *Surface Science*, 2002. ISSN 00396028. doi: 10.1016/S0039-6028(01)01525-4.

[10] I. N. Stranski and L. Krastanow. Zur Theorie der orientierten Ausscheidung von Ionenkristallen aufeinander. *Monatshefte für Chemie*, 1937. ISSN 14344475. doi: 10.1007/BF01798103.

[11] Jihoon H. Lee, Zhiming M. Wang, and Gregory J. Salamo. The control on size

and density of InAs QDs by droplet epitaxy (april 2009). *IEEE Transactions on Nanotechnology*, 2009. ISSN 1536125X. doi: 10.1109/TNANO.2009.2021654.

[12] Suwit Kiravittaya, Armando Rastelli, and Oliver G. Schmidt. Advanced quantum dot configurations. *Reports on Progress in Physics*, 2009. ISSN 00344885. doi: 10.1088/0034-4885/72/4/046502.

[13] M. Mehta, D. Reuter, A. Melnikov, A. D. Wieck, and A. Remhof. Focused ion beam implantation induced site-selective growth of InAs quantum dots. *Applied Physics Letters*, 2007. ISSN 00036951. doi: 10.1063/1.2786836.

[14] M. Mehta, D. Reuter, A. Melnikov, A. D. Wieck, and A. Remhof. Site-selective growth of self-assembled InAs quantum dots on focused ion beam patterned GaAs. *Physica E: Low-Dimensional Systems and Nanostructures*, 2008. ISSN 13869477. doi: 10.1016/j.physe.2007.09.130.

[15] Peter Lodahl, Sahand Mahmoodian, and Soren Stobbe. Interfacing single photons and single quantum dots with photonic nanostructures. *Reviews of Modern Physics*, 2015. ISSN 15390756. doi: 10.1103/RevModPhys.87.347.

[16] F. Albert, S. Stobbe, C. Schneider, T. Heindel, S. Reitzenstein, S. Höfling, P. Lodahl, L. Worschech, and A. Forchel. Quantum efficiency and oscillator strength of site-controlled InAs quantum dots. *Applied Physics Letters*, 2010. ISSN 00036951. doi: 10.1063/1.3393988.

[17] Jeppe Johansen, Søren Stobbe, Ivan S. Nikolaev, Toke Lund-Hansen, Philip T. Kristensen, Jørn M. Hvam, Willem L. Vos, and Peter Lodahl. Size dependence of the wavefunction of self-assembled InAs quantum dots from time-resolved optical measurements. *Physical Review B - Condensed Matter and Materials Physics*, 2008. ISSN 10980121. doi: 10.1103/PhysRevB.77.073303.

[18] F. Mezrag, N. Bouarissa, and M. Boucenna. The size-dependent electronic and optical properties of InAs quantum dots. *Optik*, 127(3), 2016. ISSN 00304026. doi: 10.1016/j.ijleo.2015.10.208.

[19] Ioffe Institute. Band structure information. URL http://www.ioffe.ru/SVA/NSM/Semicond/GaAs/bandstr.html#Basichttp://www.ioffe.ru/SVA/NSM/Semicond/InAs/bandstr.html#Basic.

[20] Craig Pryor. Eight-band calculations of strained InAs/GaAs quantum dots compared with one-, four-, and six-band approximations. *Physical Review B - Con-*

densed Matter and Materials Physics, 57(12), 1998. ISSN 1550235X. doi: 10.1103/PhysRevB.57.7190.

[21] H. Eisele, A. Lenz, R. Heitz, R. Timm, M. Dähne, Y. Temko, T. Suzuki, and K. Jacobi. Change of InAs/GaAs quantum dot shape and composition during capping. *Journal of Applied Physics*, 2008. ISSN 00218979. doi: 10.1063/1.3042216.

[22] Ju Wu and Peng Jin. Self-assembly of InAs quantum dots on GaAs(001) by molecular beam epitaxy. *Frontiers of Physics*, 2015. ISSN 20950470. doi: 10.1007/s11467-014-0422-4.

[23] K. Zhang, J. Falta, Th Schmidt, Ch Heyn, G. Materlik, and W. Hansen. Distribution and shape of self-assembled InAs quantum dots grown on GaAs (001). In *Pure and Applied Chemistry*, volume 72, 2000. doi: 10.1351/pac200072010199.

[24] H. S. Lee, J. Y. Lee, T. W. Kim, and M. D. Kim. Strain effects in and crystal structures of self-assembled InAs/GaAs quantum dots. *Applied Physics Letters*, 2003. ISSN 00036951. doi: 10.1063/1.1612894.

[25] M. C. Xu, Y. Temko, T. Suzuki, and K. Jacobi. Shape transition of InAs quantum dots on GaAs(001). *Journal of Applied Physics*, 98(8), 2005. ISSN 00218979. doi: 10.1063/1.2076431.

[26] Strain and misfits. URL https://slideplayer.com/slide/8012174/.

[27] Peter Krogstrup, Henrik I. Jørgensen, Erik Johnson, Morten Hannibal Madsen, Claus B. Sørensen, Anna Fontcuberta I. Morral, Martin Aagesen, Jesper Nygård, and Frank Glas. Advances in the theory of III–V nanowire growth dynamics. *Journal of Physics D: Applied Physics*, 46(31):313001, 8 2013. ISSN 0022-3727. doi: 10.1088/0022-3727/46/31/313001. URL https://iopscience.iop.org/article/10.1088/0022-3727/46/31/313001.

[28] Pavel Aseev, Alexandra Fursina, Frenk Boekhout, Filip Krizek, Joachim E. Sestoft, Francesco Borsoi, Sebastian Heedt, Guanzhong Wang, Luca Binci, Sara Martí-Sánchez, Timm Swoboda, René Koops, Emanuele Uccelli, Jordi Arbiol, Peter Krogstrup, Leo P. Kouwenhoven, and Philippe Caroff. Selectivity Map for Molecular Beam Epitaxy of Advanced III-V Quantum Nanowire Networks. *Nano Letters*, 19 (1):218–227, 2019. ISSN 15306992. doi: 10.1021/acs.nanolett.8b03733.

[29] Martín Espiñeira Cachaza, Anna Wulff Christensen, Daria Beznasyuk, Tobias Saerkjaer, Morten Hannibal Madsen, Rawa Tanta, Gunjan Nagda, Sergej Schuwalow, and

Peter Krogstrup. Selective Area Growth Rates of III-V Nanowires. *PhysRevMaterials*, 2021.

[30] Ping Show Wong, Baolai Liang, Ryan Molecke, Jun Tatebayashi, and Diana L. Huffaker. Controlled formation and dynamic wulff simulation of equilibrium crystal shapes of GaAs pyramidal structures on nanopatterned substrates. *Crystal Growth and Design*, 2010. ISSN 15287483. doi: 10.1021/cg900785f.

[31] D. T. J. Hurle. Crystal growth for beginners . 2nd edition. Edited by Ivan V Markov. World Scientific Press, pp. 564. USD 68, GBP 46. ISBN 981-238-245-3. . *Journal of Applied Crystallography*, 37(2), 2004. ISSN 0021-8898. doi: 10.1107/s0021889803028358.

[32] D.R. Brambley. Electron-Beam Technology in Microelectronic Fabrication. *IEE Proceedings I Solid State and Electron Devices*, 129(2), 1982. ISSN 01437100. doi: 10.1049/ip-i-1.1982.0007.

[33] ELS-7000. URL https://www.london-nano.com/sites/default/files/ els-g100_brochure_0.pdf.

[34] S. Verhaverbeke, I. Teerlinck, C. Vinckier, G. Stevens, R. Cartuyvels, and M. M. Heyns. The Etching Mechanisms of SiO2 in Hydrofluoric Acid. *Journal of The Electrochemical Society*, 141(10), 1994. ISSN 0013-4651. doi: 10.1149/1.2059243.

[35] Jeol Ltd. SEM Scanning Electron Microscope A To Z Basic Knowledge For Using The SEM. *Jeol Ltd*, 2009. ISSN 13596454.

[36] Udo W. Pohl. *Epitaxy of Semiconductors: Introduction to Physical Principles*. 2013.

[37] Filip Krizek, Joachim E. Sestoft, Pavel Aseev, Sara Marti-Sanchez, Saulius Vaitiekenas, Lucas Casparis, Sabbir A. Khan, Yu Liu, Tomaš Stankevič, Alexander M. Whiticar, Alexandra Fursina, Frenk Boekhout, Rene Koops, Emanuele Uccelli, Leo P. Kouwenhoven, Charles M. Marcus, Jordi Arbiol, and Peter Krogstrup. Field effect enhancement in buffered quantum nanowire networks. *Physical Review Materials*, 2(9), 2018. ISSN 24759953. doi: 10.1103/PhysRevMaterials.2.093401.

[38] C. Cornet, S. Charbonnier, I. Lucci, L. Chen, A. Létoublon, A. Alvarez, K. Tavernier, T. Rohel, R. Bernard, J. B. Rodriguez, L. Cerutti, E. Tournié, Y. Léger, M. Bahri, G. Patriarche, L. Largeau, A. Ponchet, P. Turban, and N. Bertru. Zinc-blende group III-V/group IV epitaxy: Importance of the miscut. *Physical Review Materials*, 4(5), 2020. ISSN 24759953. doi: 10.1103/PhysRevMaterials.4.053401.

[39] Andor iKon-M-934. URL https://andor.oxinst.com/products/ikon-xl-and-ikon-large-ccd-series/ikon-m-934?gclid=Cj0KCQjww4OMBhCUARIsAILndv4YxEtOj-0sLFzSxtlE4lalD5VqRuMBD1Xkkm_bEYoeZqlo9D_Ih8gaAsPPEALw_wcB.

[40] ThorLab CS165CU. URL https://www.thorlabs.com/thorproduct.cfm?partnumber=CS165CU.

7 Appendices

7.1 Growths and sample overview

Growth sample	Wafer sample	Fab method	growth parameters	notes
QD1072	?	Daria, Elionix 125kV, dry etch	GaAs(Sb); 600°C, 15 min, 0.1 Ml/s	
QD1099	QDS123	Daria, Elionix 125kV, Charline and Laurits wet etch	GaAs(Sb); 600°C, 15 min, 0.1 Ml/s	
QD1104	QDS123	Daria, Elionix 125kV , Charline and Laurits wet etch	GaAs(Sb); 585°C, 30 min, 0.1 Ml/s	Growth on mask
QD1121	QD240521.3	Charline and Laurits Elionix 100kV	GaAs(Sb); 585°C, 120 min, 0.05 Ml/s (see Appendix 7.9)	was in AFM before growth, the one with improvised etching time
QD1132	QD100621.3	Charline and Laurits Elionix 100kV	GaAs(Sb); 585°C, 120 min, 0.05 Ml/s (see Appendix 7.9)	+ InAs growth
QD1142	QD100621.4	Charline and Laurits Elionix 100kV	GaAs(Sb); 585°C, 120 min, 0.05 Ml/s (see Appendix 7.9)	+ InAs growth and capping layer

7.2 The fabrication procedure step by step

Cleanness and proper fabrication of mask for growth is crucial for the growth of QDs. Doing this project 3 different PMMA coatings have been tested, different dose settings for EBL, different development and strip of techniques, two different etching tests, dry and wet etch, the design have been adjusted a lot of times and and last but not least different settings for growth parameters have been tried out to find the optimal growth for specific QDs.

Design were made in CleWin, the repetition of design were made in WeCas and proximity effect were corrected using BEAMER
The fabrication process (Charline Kirchert and Laurits Høgel):
Spin-coating:

- Clean the tweezer and GaAs wafer in separate containers using ultra-sonic bath (power 30, frequency 37) 1 min each
    1. Acetone
    2. IPA
    3. MQ
- Clean wafer-box with running acetone/IPA/MQ.
- Spin coat with resist CSAR-62-13 (2x1000 uL) 4000 rpm 45s
- Bake 185 degrees C for 1 min

EBL settings using unofficial dose calculator/Shiv:

- Tool: 100kV
- Write field size: 150 um
- Dots: 60000
- Pitch: 1
- Aperture: 40 um
- Beam current: 100e-12 A
- Area dose: 600 $\mu C/cm^2$

Development:

- 26 s O-xylene
- 5 s MIBK
- 1 min IPA
- 3 min IPA
- Plasma ash 2 min

Verify you got your pattern in the optical microscope Wet etch:

- 0.5 % HF (calculate rate of solution)
- Etch for the time that responds to 15 nm
- MQ dip
- MQ 3 min
- Have an additional container for the tweezer

Strip of resist:

- q.3 dioxolane 3 min
- 1.3 dioxolane at least 1 hour
- Sonicate (Power 30, frequency 37) 1 min
    1. 1.3 dioxolane
    2. IPA
    3. MQ
- Plasma ash 4 min

Cleave wafer into 4 quarters (use hydrogen dryer while cleaving)

- Sonicate (P 30, F 37) 2 min:
    1. Acetone
    2. IPA
    3. MQ
- Ash 2 min

AFM 1 quarter to verify cleanness:

- AFM of patterns, guide marks, SiOx in the corner (middle of full wafer) and the edge. We assume that all 4 wafers looks the same.

Wafer is now ready for MBE (Daria Beznasiuk and Gunjan Nagda)

Etch tests (Charline and Laurits): Etch tests have been done to calculate the exact rate of the HF solution. An ellipsometer have been used to measure the thickness of the SiOx film. For a proper etch test the SiOx should be thick enough, at least 100 nm, for the ellipsometer to be most accurate.

Dose test (Charline, Laurits and Harry): When doing dose tests the area dose was changed for repetitive patterns on the wafer, this was changed in the WeCas file. After development the chip was deposit with 5 nm Ti and 20 nm Au with help from Charalampos (Harry) Lampadaris . The chip was undergoing lift off using 1.3 dioxolane 1 hour, sonicated (P 30 F 37) for 3 min in 1.3 dioxolane, finishing with MQ dip.

7.3 Angle measurements of facets

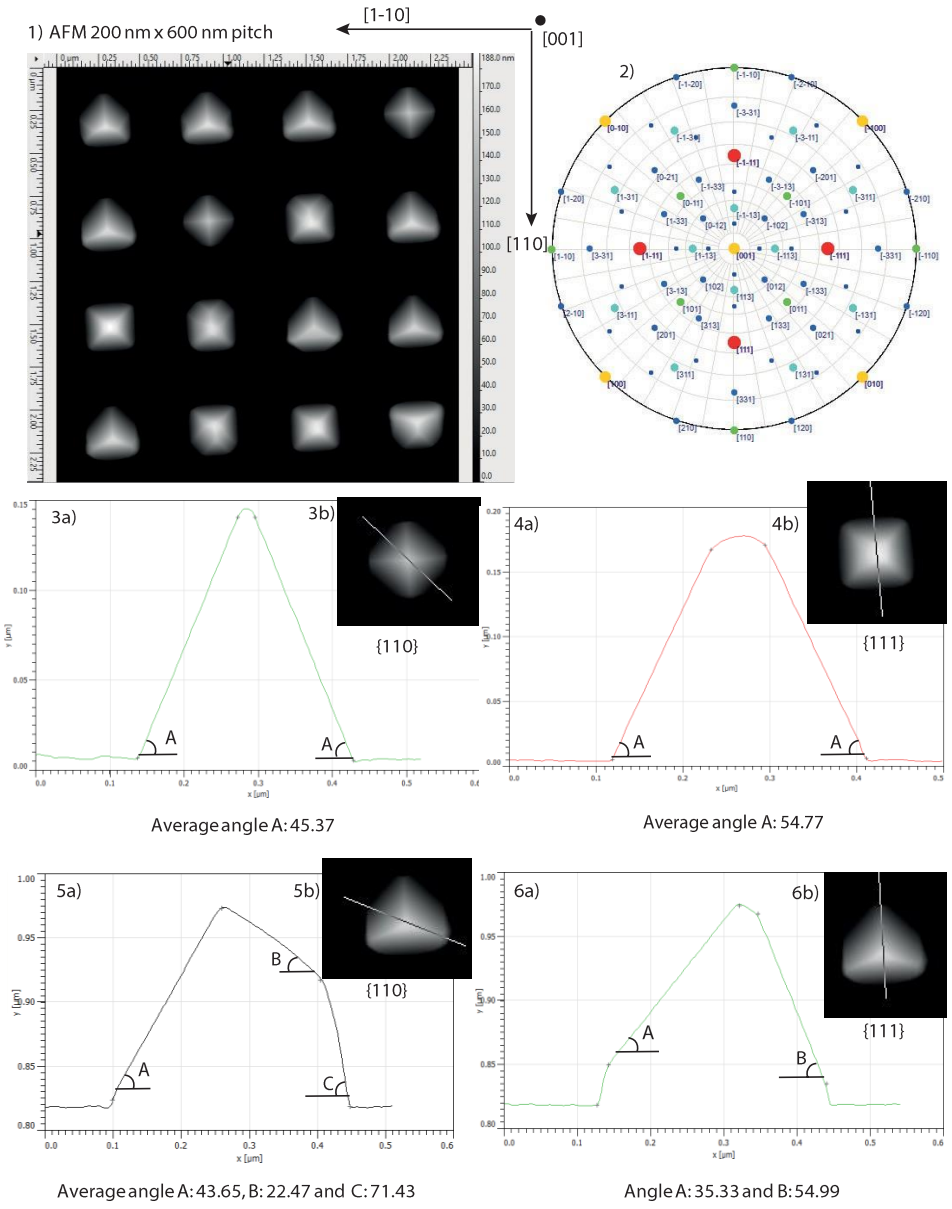

Figure 40: A schematic of how the facets were defined from the angles between the facet and the substrate. 1) The AFM image of 200 nm design dots with 600 nm pitch with indicated orientations. 2) SP orientated the same direction as the AFM. 3) to 6) show the indication of where the angles were measured for each shape.

7.4 CCDs

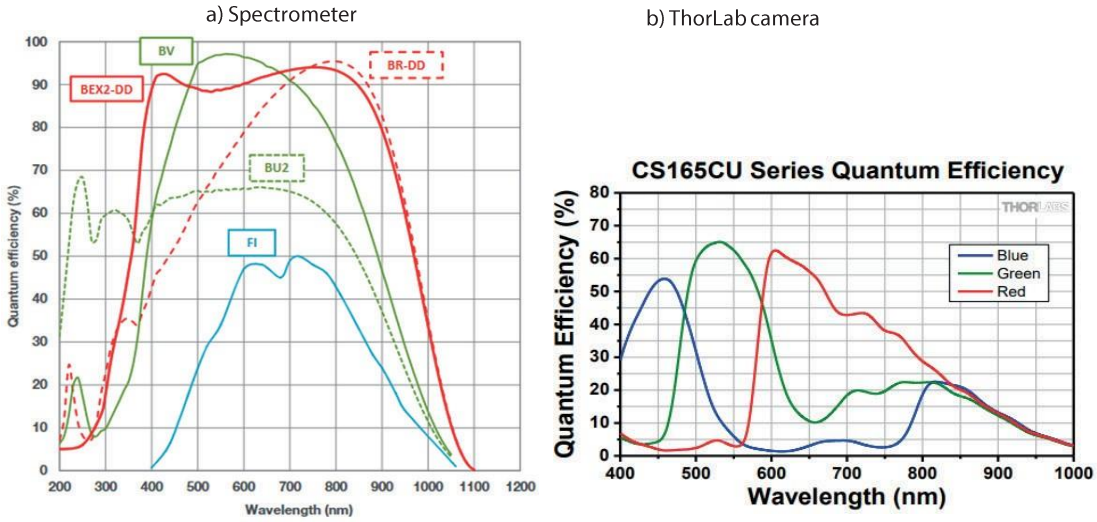

Figure 41: Quantum efficiency at wavelength in the near-infrared spectra for a) Spectrometer (BR-DD)[39] and b) ThorLab camera [40]

7.5 Area measurements of Au proximity effect

Mask the region without the Au dots

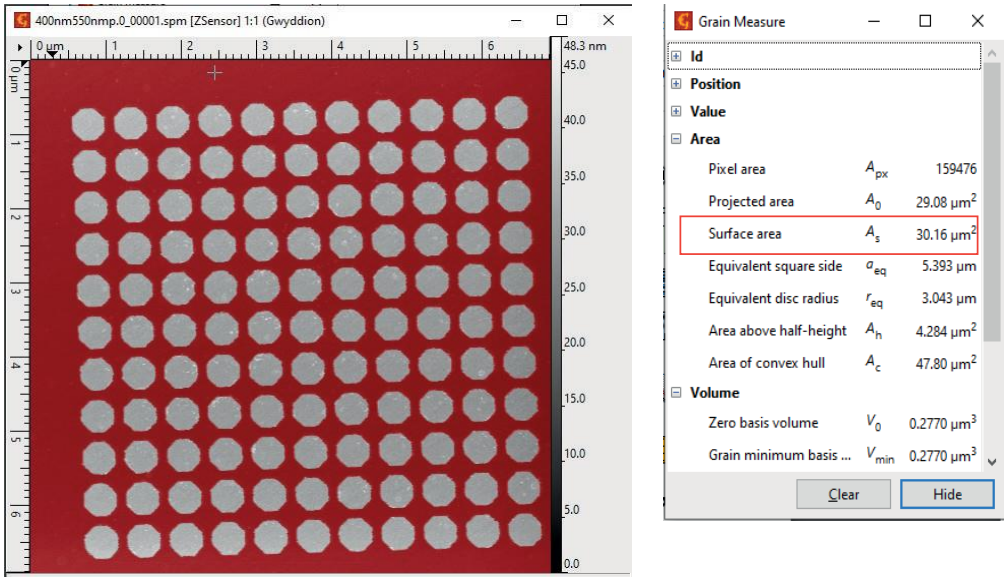

Mask the whole region

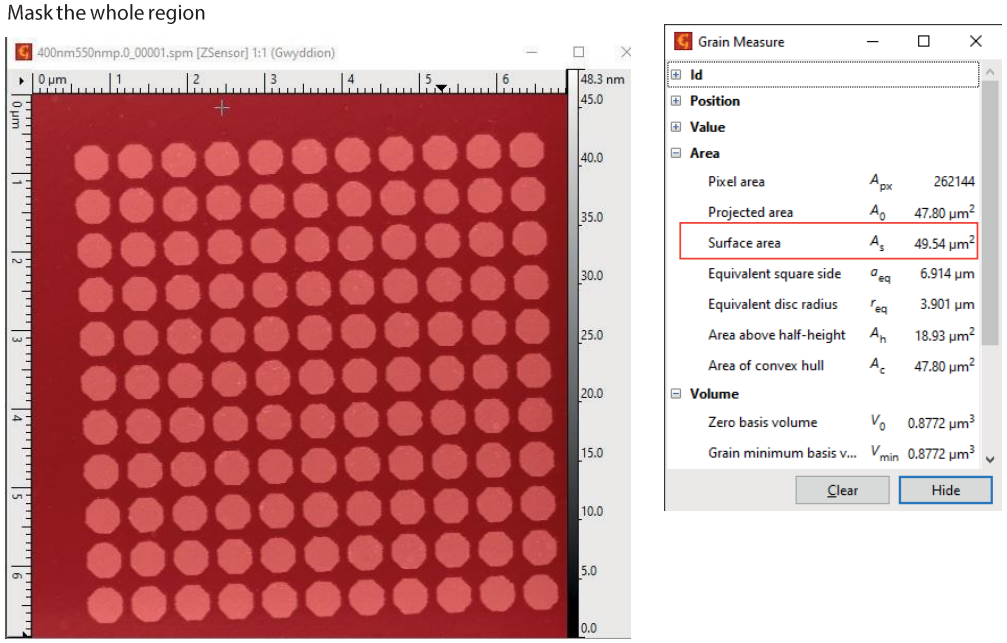

Figure 42: How the measurement for estimating the proximity effect for EBL were done using AFM images of both Au dots and GaAs buffer dots in section 4.1.

7.6 Au dots for dose test

a) 174 nm design width

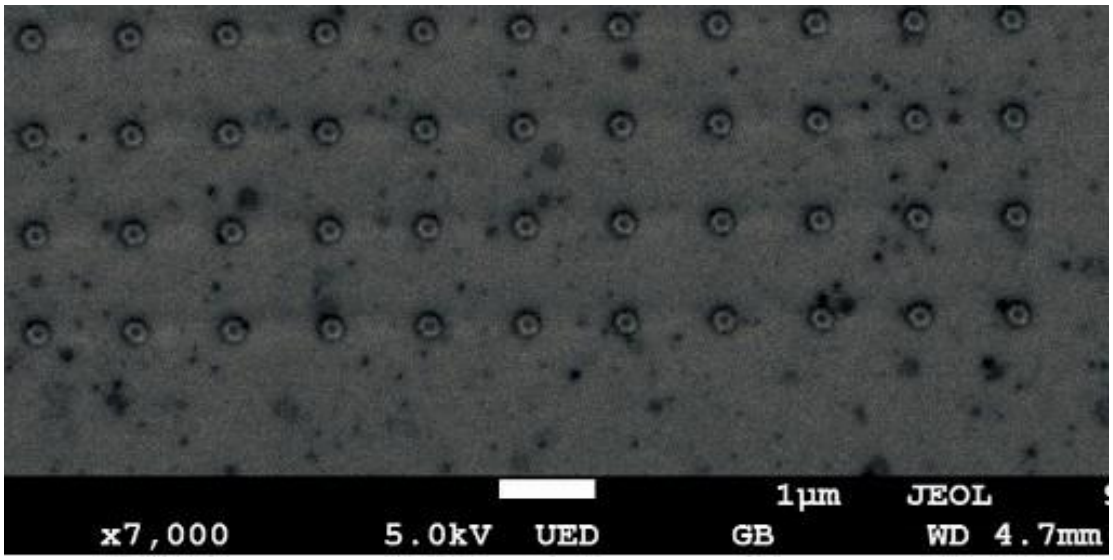

b) 230 nm design width

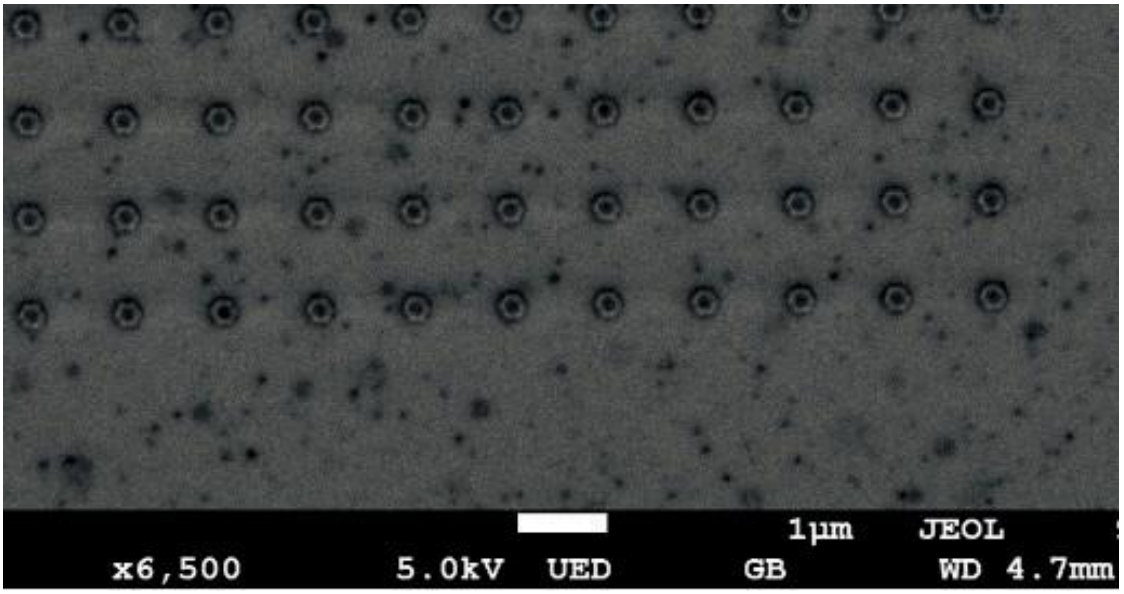

Figure 43: SEM images of a) 174 nm design width and b) 230 nm design width for Au dots deposition after development.

7.7 Area measurements of top facets

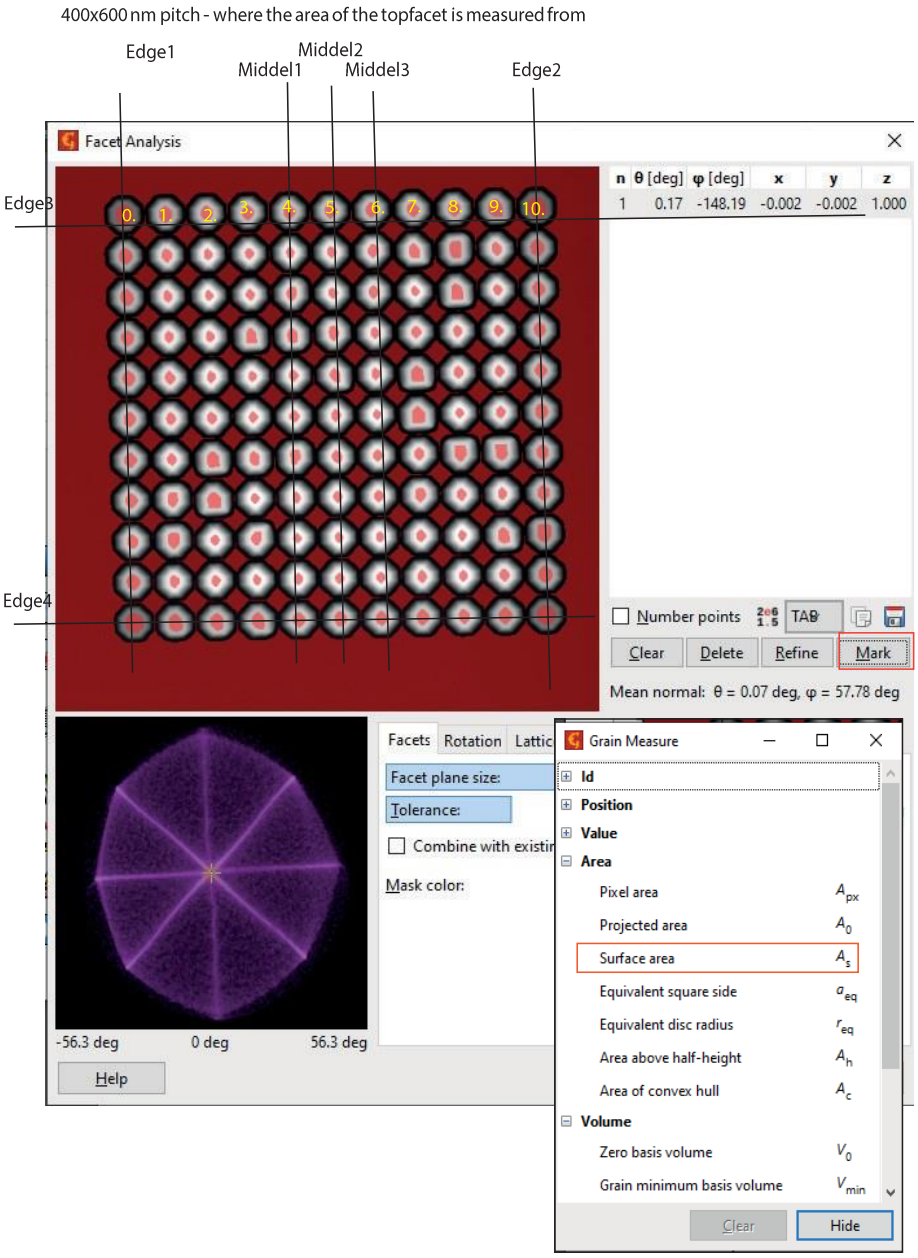

Figure 44: A schematic of how the measurements of the top-facet area of the dots at the edges and through the middle were done. The surface area (the red mask region on the dots) of each dot were measured along the 4 edges and averaged and along the 3 middle line and averaged. The definition of the position of the dots along the edges and the middle is the same for the height and diameter of the base of GaAs buffer dots.

7.8 Width measurements of base of GaAs dots

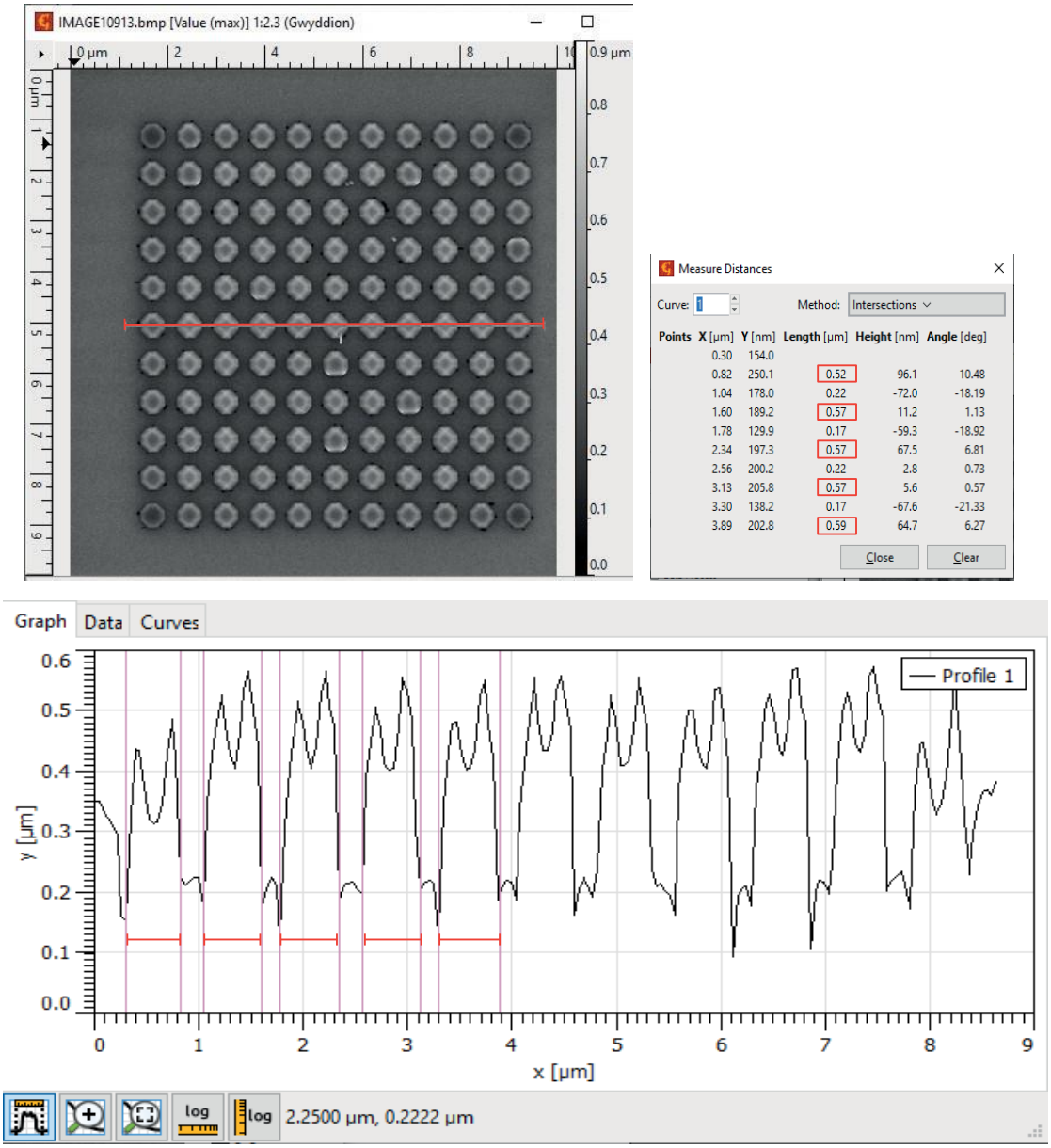

Figure 45: Schematic of how the width of the GaAs buffer structure base were measured using SEM images loaded in Gwyddion. The measurement were done for 11 QDs along the middle of the array where the red lines in the plot show the width between the lowest intensity peaks measured along the line. The top-facets of the GaAs buffer structure were done the same way only now it is the distance between the max intensities. For the top-facets the edges were left out so only 9 dots were measured.

7.9 Growth parameters

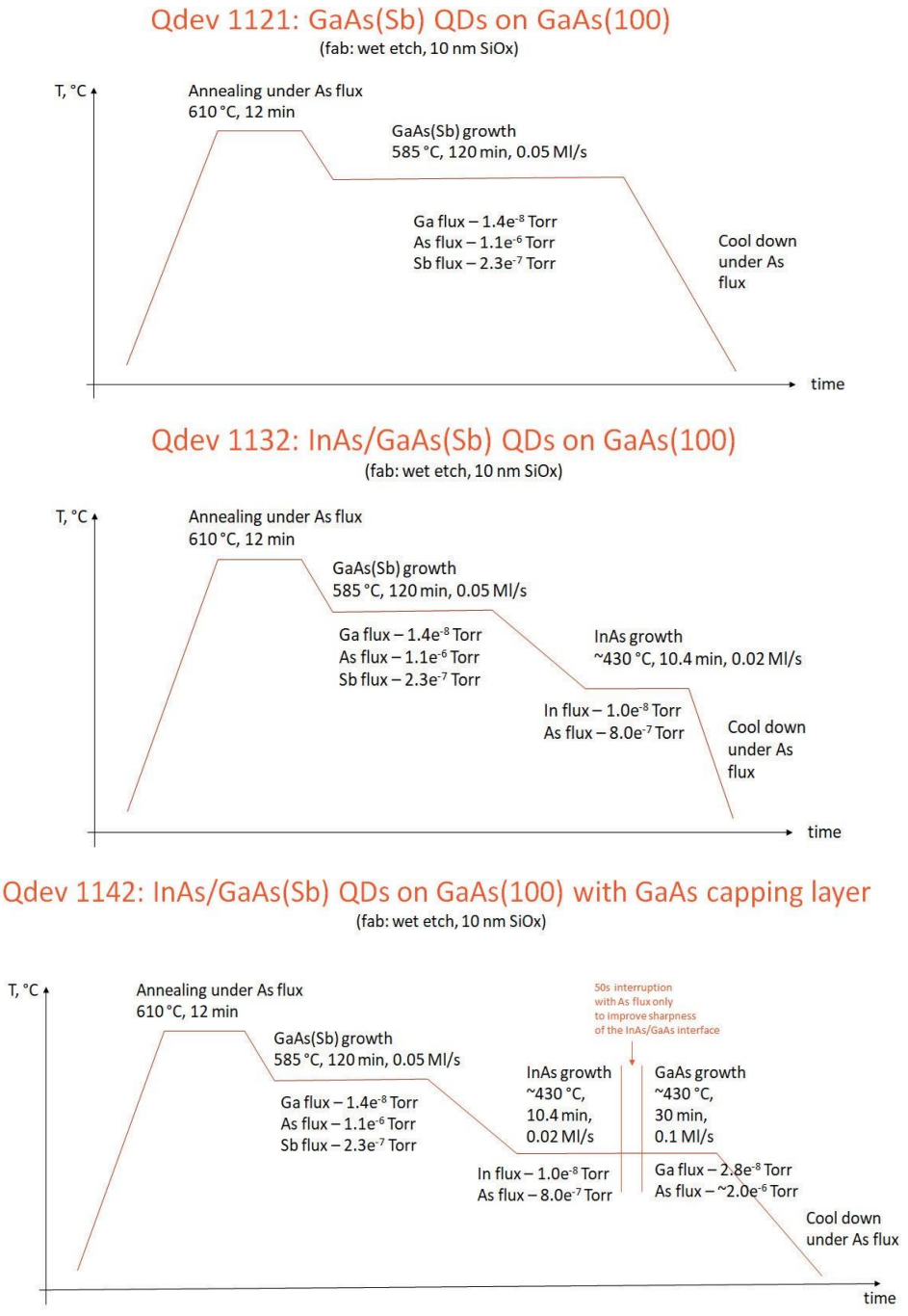

Figure 46: A schematic mabe by Daria of the growth parameters for sample QD1121, QD1132 and QD1142